Interference-Based Spectroscopy with XUV Radiation

vorgelegt von
Diplom-Physiker
Piet Hessing

Von der Fakultät II - Mathematik und Naturwissenschaften
der Technischen Universität Berlin
zur Erlangung des akademischen Grades

Doktor der Naturwissenschaften
- Dr. rer. nat. -

genehmigte Dissertation

Promotionsausschuss:

Vorsitzender: Prof. Dr. Stephan Reitzenstein
1. Gutachter: Prof. Dr. Stefan Eisebitt
2. Gutachter: Prof. Dr. Jan Lüning

Tag der wissenschaftlichen Aussprache: 03.03.2021

Berlin, 2021

Abstract

In this thesis, a novel interferometric method for the spectroscopic and time-resolved investigation of the complex optical and magento-optical refractive index in the spectral range of extreme ultraviolet radiation and soft x-rays is presented. Compared to similar methods, our method is self-normalizing and allows the determination of the real and imaginary part of the complex refractive index in only one single measurement.

The wavefront splitter of our interferometer consists of a simple monolithic combination of a double slit acting as a reference and an additional aperture containing the sample system under investigation as a free-standing film. The interferogram measured in the far field is evaluated by a single Fourier transformation. Via polarization-dependent measurements, the dichroic contributions to the complex refractive index due to the magnetization of the material can be extracted. We present proof-of-principle measurements using this concept and discuss performance and limiting factors.

Results are presented for CoGd-alloy, FeGd-alloy, and Co/Pt-multilayers, investigating for Co and Fe both the spectral regions of the respective M- and L-edges and for Gd the spectral region corresponding to the N-edge. These experiments were carried out at a synchrotron radiation source. We compare our results to experimental results in the literature and to electronic structure calculations. For the case of $Gd_{25}Co_{75}$ alloy, to our knowledge, we are the first to present experimental data on the magneto-optical refractive index at the Gd N-edge.

Beyond static measurements, we present a proof-of-concept experiment for a time-resolved investigation in a pump-probe scheme. Using a high-harmonic generation source for interferometric probing, the evolution of the magneto-optical refractive index of Fe in $Gd_{28}Fe_{72}$ is studied after optical excitation leading to ultrafast demagnetization. We conclude by discussing the current limitations of our time-resolved experiment and discuss improvements for future applications.

Zusammenfassung

In dieser Arbeit wird eine neuartige interferometrische Methode zur spektroskopischen und zeitaufgelösten Untersuchung des komplexen optischen und magentooptischen Brechungsindex im Spektralbereich extremer ultravioletter Strahlung und weicher Röntgenstrahlung vorgestellt. Im Vergleich zu ähnlichen Methoden ist unsere Methode selbst-normalisierend und erlaubt die Bestimmung des Real- und Imaginärteils des komplexen Brechungsindex in nur einer einzigen Messung.

Der Strahlteiler unseres Interferometers besteht aus einer einfachen monolithischen Kombination von einem Doppelspalt, der als Referenz dient, und einer zusätzlichen Apertur, welche das zu untersuchende Probensystem als freistehenden Film enthält. Das im Fernfeld gemessene Interferogramm wird mittels einer einzelnen Fouriertransformation ausgewertet. Durch polarisationsabhängige Messungen können die dichroitischen Beiträge zum komplexen Brechungsindex aufgrund der Magnetisierung des Materials extrahiert werden. Wir stellen *proof-of-principle*-Messungen unter Verwendung dieses Konzepts vor und diskutieren Leistungsfähigkeit und limitierende Faktoren.

Die Ergebnisse werden für CoGd-Legierungen, FeGd-Legierungen und Co/Pt-Multilagen vorgestellt, wobei für Co und Fe sowohl die Spektralbereiche der jeweiligen M- und L-Kanten als auch für Gd der Spektralbereich entsprechend der N-Kante untersucht werden. Diese Experimente wurden an einer Synchrotronstrahlungsquelle durchgeführt. Wir vergleichen unsere Ergebnisse mit experimentellen Ergebnissen aus der Literatur und mit elektronischen Strukturberechnungen. Für den Fall der $Gd_{25}Co_{75}$-Legierung sind wir unseres Wissens nach die ersten, die experimentelle Daten über den magnetooptischen Brechungsindex an der Gd N-Kante präsentieren.

Über statische Messungen hinaus stellen wir ein *proof-of-concept*-Experiment für eine zeitaufgelöste Untersuchung mittels einer *pump-probe*-Methode vor. Unter Verwendung einer Quelle zur Erzeugung hoher Harmonischer wird die zeitliche Entwicklung des magnetooptischen Brechungsindex von Fe in $Gd_{28}Fe_{72}$ nach optischer Anregung untersucht, die zu einer ultraschnellen Entmagnetisierung führt. Abschließend erörtern wir die derzeitigen Grenzen unseres zeitaufgelösten Experiments und diskutieren Verbesserungen für zukünftige Anwendungen.

Contents

List of Figures

List of Tables

CHAPTER 1

Introduction

The complex index of refraction fundamentally describes the optical properties of an optical medium. At extreme-ultraviolet (XUV) and soft x-ray photon energies, accurate understanding of the refractive index is crucial for the design of optical coatings, multilayer mirrors, and bandpass filters used for, e.g., lithography [1]. The aforementioned energy intervals also include the absorption edges of magnetic elements. For the study and development of new magnetic material, precise knowledge of the refractive index and its magnetic dichroism around absorption edges and its transient behaviour after optical excitation plays a significant role [2–4].

Previous work on the determination of the refractive index used the absorption of radiation through thin foils or gases over a broad energy spectrum [5] to measure the imaginary part β of the refractive index only. The real part δ of the refractive index was subsequently calculated by the Kramers-Kronig relation [6–8]. This indirect determination imprints any error in the measurement of β to δ, e.g., errors that can occur at the absorption edge when the value of δ changes rapidly. Moreover, In order to apply the Kramers-Kronig inversion successfully, it is also necessary that the data can be extrapolated beyond the measured range to achieve a wider domain of integration. If this condition cannot be met, further errors in the determination of the real part δ of the refractive index will occur [7].

Previous measurements of δ comprise x-ray reflectance measurements [9] and use of a Fresnel bimirror interferomety [10]. While these techniques also do not provide a complete understanding of the complex refractive index, the reflectance measurements are additionally sensitive to surface roughness, contaminations, and absorption.

Techniques that allow the direct measurement of the *complex* refractive index involve interferometry with Fresnel zone plates [11–13] or in-line holography approaches [1], Bragg scattering from specifically manufactured multilayer samples [14–16], and Mie scattering from polystyrene nanospheres [17]. While the first technique requires additional measurements to normalize the data to the incident intensity on the sample or suffers from the low transmittance of the optical setup, the latter techniques require *a priori* knowledge of the refractive index, or use iterative non-linear least square fitting that is susceptible to errors.

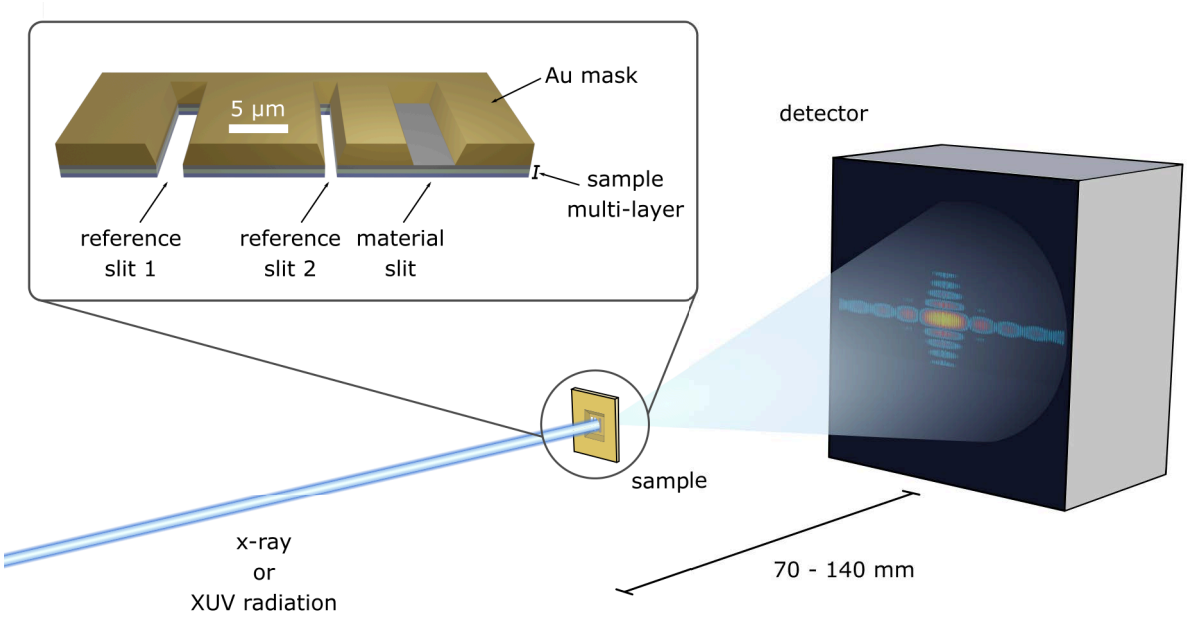

Figure 1.1: Overview of our interferometric triple-slit method. Coherent x-ray or XUV radiation is incident on the sample. The wavefront splitting apertures consists of three slits that have been prepared in a gold mask (see inset for cutaway drawing). One of the slits contains the sample layer to be examined, while the other two slits are devoid of material and are used as references in the data analysis. The far-field diffraction pattern is recorded by a detector. The selected distance between the sample and the detector depends on the photon energy and the sample geometry. The lengths given in this figure describe the typical orders of magnitude that we have used in the work presented in this thesis.

In this thesis, we present a novel interferometric technique (Fig. 1.1) for the spectroscopic study of optical and magneto-optical refractive indices, that is self-normalizing, allowing for easy time-resolved experiments, and determines β and δ from a single exposure[1] with non-iterative analysis. The only *a priori* knowledge needed, involves only experimental parameters such as photon energy and layer-thickness of the investigated element. Based on Thomas Young's double slit experiment, we will call the technique presented here the *triple-slit method*. In comparison to most other interferometric experiments to determine the refractive index, the wavefront splitting apertures of our technique are easily manufactured. Regarding magnetic materials in particular, the approach can be used for samples with out-of-plane and in-plane magnetization.

This thesis is composed of six main chapters. After the general introduction in Ch. 1, Ch. 2 discusses the interferometric principles of our method. Here, the mathematical framework is introduced and compared to similar interferometric methods. We present the

[1]For the determination of the magneto-optical part of the refractive index, or the extraction of the element-specific refraction from a multi-component multilayer two exposures are needed.

experimental details of the sample systems, the instrumentation, and the implementation of our experiment at a XUV source and a soft x-ray source in Ch. 3. In Ch. 4, we show our spectroscopic results from $[Co(4)Pt(7)]_{\times 20}$, $Gd_{25}Co_{75}$, and $Gd_{25}Gd_{75}$ at the M-edge and L-edge of the transition metals as well as at the Gd N-edge and compare them with values from literature and theory. Chapter 4 is followed by a discussion of the influence of experimental noise on the analysis of the refractive index (Ch. 5). This chapter is used as preparation for the challenges in Ch. 6, where we demonstrate the time-resolved capabilities of our method for a $Gd_{28}Fe_{72}$-alloy at the Fe M-edge and discuss future developments and improvements of our triple-slit method.

CHAPTER 2

Physical Principles

2.1 Concepts of Interferometric Measurements

Before we deal with the composition of the measured intensity distribution of the triple-slit diffraction and its data analysis in Ch. 2.2, we first want to establish some basic concepts of our method by examining two closely related experiments: the double slit experiment and Fourier transform holography (FTH). Through the double-slit experiment we will demonstrate how phase differences of light beams are mapped into the measured intensity distribution. By reviewing FTH, we will explore how this mapping can be used to reconstruct the amplitude and phase of light transmitted through the sample.

2.1.1 Double Slit Experiment

The double slit experiment is one of the central experiments in modern physics and demonstrates the quantum nature of small particles like photons, electrons, neutrons, or even molecules. The wave-particle duality, single particle interference and superposition of states, Heisenberg's uncertainty principle, as well as the collapse of the wave function are just a few basic insights into the nature of the quantum world this simple experiment offers. It is, therefore, not surprising that Richard Feynman used the following emphatic words in his 1963 lecture to describe the observations of the double slit experiment [18]: "We choose to examine a phenomenon which is impossible, absolutely impossible, to explain in any classical way, and which has in it the heart of quantum mechanics. In reality, it contains the only mystery."

Quantum mechanics was still waiting for its dawn, when at the beginning of the 19^{th} century, Thomas Young famously discovered that the diffraction of light split into two small beams cannot be explained by the simple addition of both single beam diffraction patterns, as it would be expected by the prevailing Newtonian view on light. Young described his findings in a new undulation theory of light [19, 20] by comparing his results to the behaviour of waves.

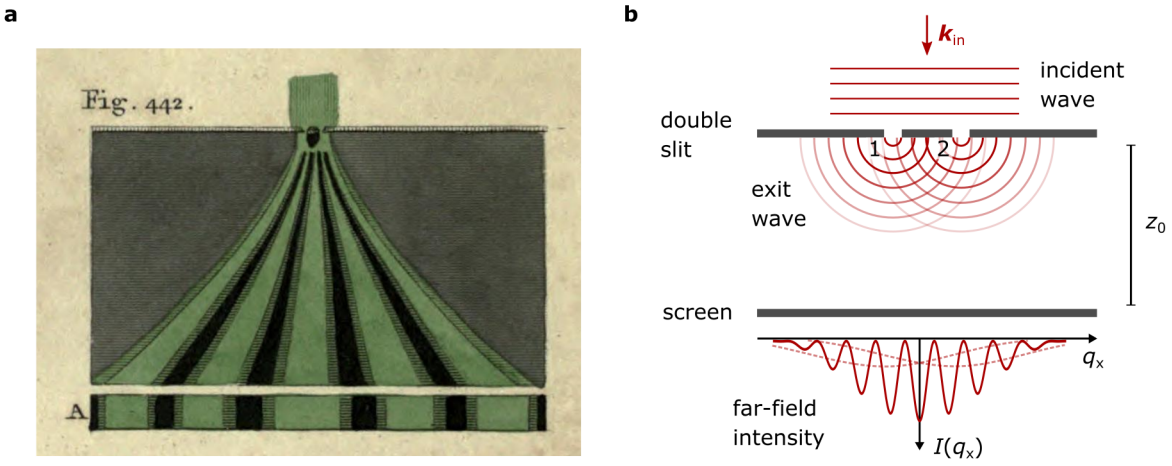

Figure 2.1: Sketch of the double slit experiment. **a** The figure was taken from T. Young's publication of his double aperture experiment from 1807 [20]. The corresponding caption reads: "The manner in which two portions of coloured light, admitted through two small apertures, produce light and dark stripes or fringes by their interference, proceeding in the form of hyperbolas; the middle ones are however usually a little dilated, as at A.". **b** Monochromatic plane waves with the wave vector $\boldsymbol{k}_{\mathrm{in}}$ fall onto a wall with two small slits 1 and 2. The exit wave propagates to a screen over a distance z_0. The far-field intensity distribution $I_{12}(q_{\mathrm{x}})$ equals the absolute square of the coherent sum from both single slit intensities. The intensities from both individual slits, $I_1(q_{\mathrm{x}})$ and $I_2(q_{\mathrm{x}})$ are given by the dashed lines.

Figure 2.1a shows an original sketch of T. Young's double aperture experiment from 1807 [20]. "One-coloured light" shines onto a wall with a small opening. This opening is split in half by a slim object like the side of a paper. In some distance light and dark fringes can be observed due to the interference between both beams sections. The modern representation of the double slit setup in Fig. 2.1b depicts both slits as sources of spherical waves. If the right slit would be closed so that the left slit would be the only one transmitting a spherical wave ψ_1, the far-field intensity would be equal to the corresponding dashed line depicted in the lower part of Fig. 2.1b. With both slits open, the amplitude of both waves adds up to $(\psi_1 + \psi_2)$. For the intensity I_{12} at the screen in the distance z_0 after the slits, we get:

$$I_{12} = |\psi_1(z_0) + \psi_2(z_0)|^2 \tag{2.1}$$

$$= I_1 + I_2 + 2\sqrt{I_1 I_2}\cos(\phi_1 - \phi_2), \tag{2.2}$$

with $(\phi_1 - \phi_2)$ being the phase difference between both wave fields at z_0.

The first two terms in Eq. 2.2 simply represent the incoherent sum of the individual slit diffraction patterns. The last term is called the interference term. Depending on the place of observation, the interference term modulates the incoherent summation of the single-slit's diffraction according to the phase difference. Consequently, the far-field diffraction I_{12} maps the phase differences $(\phi_1 - \phi_2)$ between the individual slits as intensity

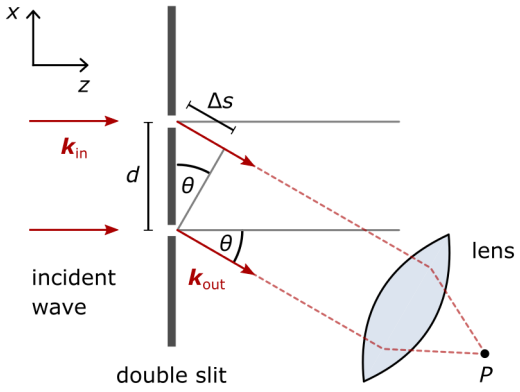

Figure 2.2: Geometric properties of the double slit diffraction. The wave field amplitude at a point P located in the far field depends on the angle θ and, therefore, on the distance Δs. Maxima of the intensity $I(\theta)$ can be observed if Δs is a multiple of the wavelength $\lambda = 2\pi/|\boldsymbol{k}|$, with $\boldsymbol{k}$ being the wave vector.

modulations. As we will see at the end of this section, this principle is used in Fourier transform holography (FTH) to overcome the problem that phase information is inevitably lost in intensity measurements[1] [22].

The analytical expression for the double-slit far-field diffraction can be derived from Fourier optics, but even with some basic geometrical considerations some key findings can be obtained. Figure 2.2 shows an observer in the far field looking at the double slit diffraction under an angle θ. The light beam from the slit, which is further away from the observer, travels an additional distance of Δs. This translates into a phase difference of

$$\Delta\phi = \frac{2\pi}{\lambda}\Delta s \tag{2.3}$$

$$= \frac{2\pi}{\lambda} d \sin\theta. \tag{2.4}$$

From Eq. 2.3 one can easily see that for a distance $\Delta s = n\lambda$ the phase difference is an even multiple of π so that constructive interference will occur under the corresponding angle θ. The spacing of the intensity maxima, called $\Delta q_{\max}$, at a distance z_0 is given by

$$\Delta q_{\max} = \frac{z_0 \lambda}{d}. \tag{2.5}$$

An important result of Fourier optics is that the relationship between the exit wave $\psi(x, z = 0)$ and the wave in the far field $\psi(x, z_0)$ is modelled by a Fourier Transformation $\mathcal{F}$:

$$\Psi(q_x) = (\mathcal{F}\psi(x, 0))(q_x). \tag{2.6}$$

Here, q_x stands for the reciprocal coordinate and, as we retain in the following, we use capital letters for the Fourier transformation of a function.

[1] This problem is also referred to as the phase problem in imaging [21].

In the following we will give the analytical solution of Eq. 2.6. We assume that the exit wave $\psi(x,0)$ was generated by N rectangular apertures[2] with an opening size of a and a spacing of d:

$$\psi(x,0) = \text{rect}\left(\frac{x}{a}\right) * \sum_{n=1}^{N} \delta(x - nd), \tag{2.7}$$

where we convoluted the rectangular function $\text{rect}(x/a)$ with a comb of Dirac distributions $\delta(x - nd)$ to get the periodic continuation of the rectangular function. With Eq. 2.7 and Eq. 2.6, the far intensity distribution is then given by [23]:

$$I(q'_x) = \left|\Psi(q_x)\big|_{q_x = q'_x/(\lambda z_0)}\right|^2 \tag{2.8}$$

$$= \left(\frac{a}{\lambda z_0}\right)^2 \text{sinc}^2\left(\frac{a}{\lambda z_0} q'_x\right) \sin^2\left(N\frac{d}{\lambda z_0} q'_x\right) \sin^{-2}\left(\frac{d}{\lambda z_0} q'_x\right). \tag{2.9}$$

In Eq. 2.8, we used the coordinate transformation $q_x = q'_x/(\lambda z_0)$ to get q_x independent from the wavelength λ and the distance z_0 between the apertures and the observation plane. The first two factors in Eq. 2.9 describe the far-field diffraction of a single aperture, while the last two sine functions give the expression for the interference between the N apertures. From Eq. 2.9 one can see that the diffraction pattern $I(q'_x)$ scales in size with the distance z_0. The aperture size a/λ in units of the wavelength scales the height of the diffraction orders, while the distance d/λ in units of the wavelength scales inversely their position in relation to the zero order diffraction.

2.1.2 Connection to Holography

In the previous section, it was explained how the far-field interference of the double slit maps the phase difference between both slits as intensity modulations (Eq. 2.2). This property is exploited in a similar way for lensless imaging through a technique called Fourier transform holography (FTH) [22, 24] to circumvent the phase problem[3]. Both our triple-slit method and FTH use a similar approach to analyse the interferograms. In this paragraph we will describe the similarities between the FTH and the triple-slit method presented in this thesis.

In order to understand the basics of FTH, we imagine that one slit of the double slit becomes small in relation to the other. Therefore, the position of the photons transmitted through the smaller slit is very well known. According to the Heisenberg uncertainty principle, the variable complementary to the photons position, its momentum $\boldsymbol{q}$, must become less known. If the smaller slit restricts the photons to one point in space, the photons momentum in the reciprocal space of the detector plane becomes maximal unknown and has, therefore, the same non-zero phase and amplitude on every point on the detector plane. Because these photons have the same phase everywhere, the phase of

[2]For the sake of generalization we give the solution to Eq. 2.6 for N rectangular apertures which includes the triple slit case explained in section 2.2.1.

[3]The phase problem is an inverse problem that states the inevitable loss of phase information during intensity measurements, making it impossible to have a unique direct relationship between the far-field intensity $I(q_x)$ and the object which caused $I(q_x)$.

the photons from the larger slit can be exactly mapped as intensity modulations in $I(q_x)$ by the interference term $2\sqrt{I_1 I_2}\cos(\phi_1 - \phi_2)$.

Mathematically this can be expressed as follows[4]. The smaller slit $s_1(x)$, called the reference, is equal to a delta distribution:

$$s_1(x) = \delta(x), \tag{2.10}$$

while the other slit contains the object to be imaged and can have an arbitrary transmission function:

$$s_2(x) = t(x). \tag{2.11}$$

In general, the transmission function is complex and describes the amplitude decrease and phase shift of the incident wave after transmission through the material. If the incident wave has constant phase of zero and an amplitude equal to one (plane wave), the exit wave becomes:

$$\psi(x) = \delta(x) + t(x). \tag{2.12}$$

With Eq. 2.6 and Eq. 2.8 the far-field intensity is given by:

$$\begin{aligned} I(q_x) &= |(\mathcal{F}\psi)(q_x)|^2 && (2.13)\\ &= |(\mathcal{F}\delta)(q_x)|^2 + |(\mathcal{F}t)(q_x)|^2 + 2\,\mathrm{Re}\{(\mathcal{F}\delta)(q_x)(\mathcal{F}t)^*(q_x)\} && (2.14)\end{aligned}$$

To recover the transmission function $t(x)$ of the object, which is illuminated by a plane wave, we apply an inverse Fourier transformation to Eq. 2.14. With the convolution theorem[5], we arrive at the Patterson map:

$$\begin{aligned} p(x) &= (\mathcal{F}^{-1}I)(x) && (2.15)\\ &= (\delta(\xi) * \delta(-\xi))(x) + (t(\xi) * t^*(-\xi))(x) \\ &\quad +(\delta(\xi) * t^*(-\xi))(x) + (t(\xi) * \delta(-\xi))(x), && (2.16)\end{aligned}$$

where the symbol $*$ indicates the convolution operator.

To write the Patterson map as an expression of correlations instead of convolution, we use the following relationship between the convolution operator $*$ and the cross-correlation operator[6] $\star$:

$$(f \star g)(t) = (f^*(-\tau) * g(\tau))(t). \tag{2.17}$$

This allows the Patterson map $p(x)$ from Eq. 2.16 to be expressed as follows:

$$p(x) = (\delta \star \delta)(x) + (t \star t)(x) + (t \star \delta)(x) + (\delta \star t)(x). \tag{2.18}$$

The first two terms describe the auto-correlation of the individual exit waves of both slits. The last two terms, called cross-correlations, contain the image information. Depending

[4]We restrict our mathematical analysis to one dimension for simplicity reasons. The extension to two dimensions is straight forward.

[5]The convolution theorem states that the convolution of two functions a and b is given by the following expression: $f * g = \mathcal{F}^{-1}((\mathcal{F}f)(\mathcal{F}g))$.

[6]The cross-correlation is defined as $(f \star g)(t) \coloneqq \int f^*(\tau)g(\tau + t)d\tau$.

on where the delta distribution $\delta(x)$ is located, it is either the neutral element of the cross-correlation or becomes a parity operator for the complex conjugate. The images of the object will, therefore, appear at the positions

$$(\delta \star t)(x) = t(x) \tag{2.19}$$

and

$$(t \star \delta)(x) = t^*(-x) \tag{2.20}$$

in $p(x)$. The point-mirrored and complex conjugated image from Eq. 2.20 is called twin image.

Figure 2.3 demonstrates the reconstruction process of the Patterson map $p(x)$ from a far-field intensity measurement $I(q_x)$ of an exit wave $\psi(x)$. As object we have chosen a rectangular transmission function with an arbitrary phase. The distance of the reference to the center of the object is x_0, while the object has a spatial half width of a. In the Patterson map shown in Fig. 2.3c, we see that the autocorrelation is twice as large as the object. Therefore, the spacing x_0 between the object and reference must be larger than $3a$ to avoid overlapping between the cross-correlations and the auto-correlation.

As we have shown in Eq. 2.1.2 and Fig. 2.3, FTH can not only map spatial information of the object, but is in principle also able to recover amplitude and phase of the complex exit wave. In reality, the far-field intensity pattern requires high-dynamic-range detection, which is not supported by most soft x-ray detectors. Experimentally, it is, therefore, common to block the brighter central part of $I(q_x)$, which relates to a measurement of a high-pass filtered version of $I(q_x)$. This makes it impossible to quantitatively determine absorption and dispersion information from the reconstruction.

Another challenge for quantitative imaging is the need for a normalization routine. While in our derivation of FTH we assumed a plane wave with unity amplitude as an incident wave, in reality the intensity transmitted through the apertures varies with the source properties during the exposure time of the detector. For this challenge alone, one would need a source, stable in time, whose photon flux is well characterised over a wide spectral range to normalise the signal to the incident intensity. Without this normalisation, it would not be clear, for example, when investigating a dynamic process, whether a change in the signal is due to a change in the response of the sample, or was caused by a fluctuation of the source.

A further obstacle is that the reference aperture is spatially extended and, therefore, the assumption of a point source is not justified. As a result, the reference's part of the interference term is no longer homogeneous. Additionally, photon-energy-dependent wave-guiding effects can occur at the reference aperture, which further influence the exit wave of the reference.

The method we want to present in this thesis is strongly related to FTH, as it also uses an inverse Fourier transformation on the diffraction pattern to access the cross-correlations but sacrifices the property of spatial imaging to overcome the problems of quantitative mapping of absorption and dispersion. In section 2.2, we will see what modifications need to be made to FTH, or more generally, to the double slit experiment to achieve this goal.

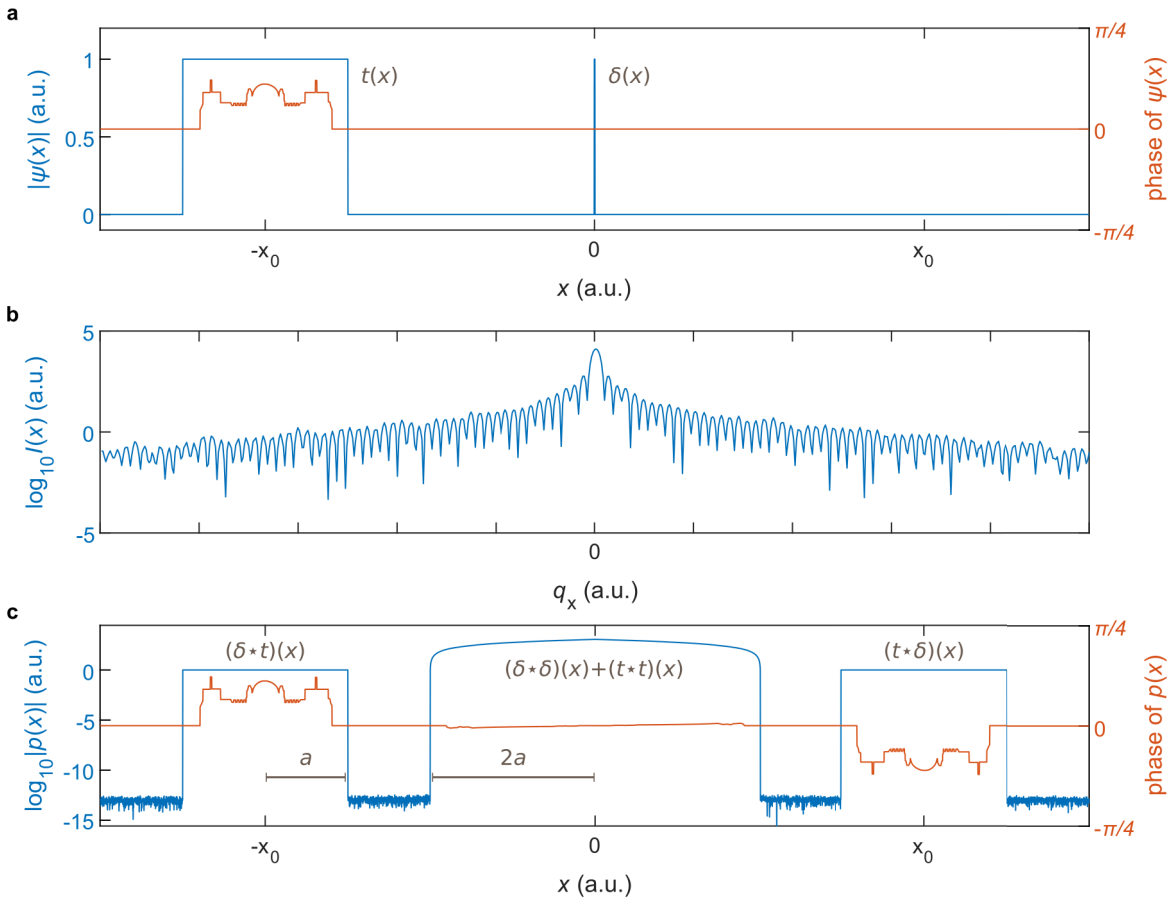

Figure 2.3: Demonstration of the FTH principle in one dimension. **a** The amplitude of the exit wave $\psi(x)$ is given by the blue curve, which is composed of the delta-like reference $\delta(x)$ at the origin and a rectangular transmission function $t(x)$ for the object aperture centred at $-x_0$ with an half size of a. The phase of the exit wave, coloured in orange, has an arbitrary shape inside the object aperture. **b** The far-field intensity $I(x)$ for $\psi(x)$ is shown in logarithmic scaling. **c** Patterson map $p(x)$ of the far-field intensity from **b**. The amplitude of $p(x)$ is shown in logarithmic scale to show the auto- and cross-correlation simultaneously. The cross-correlation terms $(\delta \star t)(x)$ and $(t \star \delta)(x)$ appear at the position $-x_0$ and x_0 respectively. The auto-correlation has a half size of $2a$. The noise in the amplitude is due to the logarithmic scaling and digital artefacts. With the comparison to **a**, it is apparent that the distance from reference to object x_0 must be greater than $3a$ to avoid overlapping of auto-correlation and cross-correlation.

2.2 Triple Slit Experiment

We have seen in the last section and in Fig 2.3 that the reconstruction algorithm of FTH is able to quantitatively reproduce the relative phase shift between a reference and an object aperture. However, the reconstructed amplitude does not only depend on the absorption by the object, but also on the incident intensity. This problem can be expressed mathematically as follows. Let the two arbitrary functions

$$s_1(x) = a_1(x)\mathrm{e}^{i\phi_1(x)} \tag{2.21}$$

and

$$s_2(x) = a_2(x)\mathrm{e}^{i\phi_2(x)} \tag{2.22}$$

represent the local exit waves of two corresponding slit. Their cross-correlation then becomes:

$$(s_1 \star s_2)(\xi) = \int s_1^*(x)s_2(x+\xi)dx. \tag{2.23}$$

We will call the position, where the cross-correlation integral has a maximum, ξ_m. If the two exit waves are constant over the area of the slits, Eq. 2.23 then becomes:

$$(s_1 \star s_2)(\xi_\mathrm{m}) = a_1 a_2 w\mathrm{e}^{i(\phi_2-\phi_1)}, \tag{2.24}$$

with w being the width of the slits. The phase difference $\phi_2 - \phi_1$ is zero if both slits are devoid of any material or contain the same material layer. If only one slit contains a material layer, the phase difference $\phi_2 - \phi_1$ is equal to the relative phase shift that the incident wave receives due to the interaction with the material. We will call the slit, containing the material layer, *material slit*, and the slit without material layer *vacuum slit*.

The amplitude of the cross-correlation $|(s_1 \star s_2)(\xi_\mathrm{m})| = a_1 a_2 w$ scales with the width w of the slits and the product of the amplitudes $a_1 a_2$. From the product $a_1 a_2$, it is ambiguous which part can be attributed to the absorption in the material layer and which to the incident intensity. To solve the problem of the ambiguous amplitude reconstruction, we need a normalization to the incident intensity. The idea of the triple-slit concept is that a third vacuum slit is introduced to the vacuum/material double slit (Fig. 1.1). The two vacuum slits act as references, whose cross-correlation monitor the incident intensity. We will refer to both vacuum slits as *reference slits* when we want to emphasize their function in the data analysis. The triple-slit configuration allows the measurement of the exit wave properties and normalization simultaneously.

In the following section, we will discuss the formation of the triple slit exit wave, the far field diffraction pattern, and the reconstruction of the absorption and dispersion of the layer in the material slit.

2.2.1 Triple Slit Exit Wave

The important requirement of the interferometric method presented in this thesis is the elastic scattering between photons and electrons in the sample. As the wavelength of the

photons utilized during our experiments is much larger than the spacing of the atoms in the samples, it is reasonable to use a continuous description of the scattering process. The effect of the material on the passing radiation is described by the complex refractive index $n(\omega)$. In the XUV and soft x-ray regime, it is common to write the refractive index of a given material as deviation from vacuum as the difference is small [25]:

$$n(\omega) = 1 - \delta(\omega) + i\beta(\omega) \tag{2.25}$$

The real part $\delta(\omega)$ of the refractive index $n(\omega)$ describes the dispersive phase change of a wave $\psi(\boldsymbol{r})$, while the imaginary part $\beta(\omega)$ describes the absorptive amplitude change. This is demonstrated in the following equation, where we assume a monochromatic plane wave $\boldsymbol{k} \cdot \boldsymbol{r} = k_z z$ for simplicity reasons, starting to propagate through a medium with refractive index n at $z = 0$:

$$\begin{aligned} \psi(z,t) &= \psi_0 \exp(i(nkz - \omega t)) && (2.26)\\ &= \psi_0 \exp(i((1 - \delta + i\beta)kz - \omega t)) && (2.27)\\ &= \psi_0 \exp(-\beta kz) \exp(-i\delta kz) \exp(ikz) \exp(-i\omega t), && (2.28) \end{aligned}$$

with k being the vacuum wave number and ω being the angular frequency of the light wave. The first exponential in Eq. 2.28 describes the absorption through a decay in amplitude, the second exponential describes a phase shift of the wave, the third exponential equals the exponential of the vacuum propagation, and the last one is the global phase for the time propagation. The goal of this thesis is to establish an interferometric method to simultaneously measure the amplitude decay and the phase shift of a wave after interaction with a medium and reconstruct the underlying optical constants. To see how our triple slit method is able to achieve this goal, we will first look at the formation of the exit wave.

All three slits are illuminated by the incident wave $\psi_{\text{in}}(\boldsymbol{r})$. Two of the three slits in the triple slit setup are used as reference slits and are devoid of any material. The exit wave after the reference double slit is given by:

$$s_{\text{ref}}(\boldsymbol{r}) = \sum_{n=1}^{2} \psi_{\text{in}}(\boldsymbol{r}) t_{\text{ref},n}(\boldsymbol{r}) \tag{2.29}$$

with the binary reference transmission function

$$t_{\text{ref},n}(\boldsymbol{r}) = \begin{cases} 1, & \text{for } \boldsymbol{r} \in \text{ref. slit}(n) \\ 0, & \text{else,} \end{cases} \tag{2.30}$$

where the index n labels the individual apertures of the reference double slit. Hereby, we neglected any waveguiding and near-field propagation, as we assume the slits thickness to be thin and the slits size to be significantly larger than the wavelength.

One of the three slits contains a thin film of the investigated medium. The time independent exit wave behind the material slit with layer thickness d reads:

$$s_{\text{mat}}(\boldsymbol{r}) = \psi_{\text{in}}(\boldsymbol{r}) t_{\text{mat}}(\boldsymbol{r}) \exp(-\beta kd) \exp(-i\delta kd). \tag{2.31}$$

As before, the binary function $t_{\text{mat}}(\boldsymbol{r})$ is equal to unity when $\boldsymbol{r}$ is element of the material slit area and zero elsewhere.

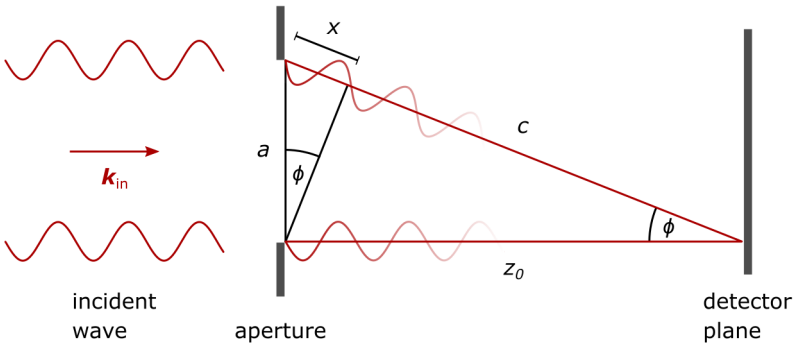

Figure 2.4: Illustration of the Fresnel number. The length a equals the characteristic size of the aperture and z_0 stands for the distance between the aperture and the detector. If the wavelength λ equals the length x, the Fresnel number becomes $F = a/z_0 \cdot a/x = \tan(\phi)/\sin(\phi) \approx 1$ for small angles ϕ. If the length x becomes small against the wavelength λ, both sides of the triangle—z_0 and c—can be treated as parallel regarding wave mechanics. If this holds true for every point on the detector, the detector is said to be in the far-field.

Summarized, the exit wave behind the triple slits is given by:

$$\begin{aligned} \psi(\boldsymbol{r}) &= s_{\text{mat}}(\boldsymbol{r}) + s_{\text{ref}}(\boldsymbol{r}) && (2.32) \\ &= \psi_{\text{in}}(\boldsymbol{r}) \left(t_{\text{mat}}(\boldsymbol{r}) \exp(-\beta k d) \exp(-i\delta k d) + \sum_{n=1}^{2} t_{\text{ref},n}(\boldsymbol{r}) \right) && (2.33) \end{aligned}$$

In the following sections, we will assign numbers to the slits to keep the formulas concise. We will call the material slit

$$s_1(\boldsymbol{r}) \coloneqq s_{\text{mat}}(\boldsymbol{r}) \tag{2.34}$$

and the reference slits

$$\begin{aligned} s_2(\boldsymbol{r}) &\coloneqq \psi_{\text{in}}(\boldsymbol{r}) t_{\text{ref},1}(\boldsymbol{r}) && (2.35) \\ s_3(\boldsymbol{r}) &\coloneqq \psi_{\text{in}}(\boldsymbol{r}) t_{\text{ref},2}(\boldsymbol{r}). && (2.36) \end{aligned}$$

2.2.2 Far-Field Diffraction

The measured interferogram results from free space propagation of the triple slit exit wave to the detector plane. The detector is said to be in the far-field regime, if the Fresnel number F is much smaller than one for every point on the detector:

$$F = \frac{a^2}{\lambda z_0} \ll 1, \tag{2.37}$$

with the characteristic size of the exit wave a, the distance between sample and detector plane z_0 and the photon wavelength λ. This is another way of saying that in the far-field the scattered beams can be treated as parallel in regards to the wave mechanics (Fig. 2.4).

If this approximation is fulfilled, the propagated wave field at the detector plane is given by the Fraunhofer diffraction integral:

$$\Psi(\boldsymbol{q}) = \int_{\boldsymbol{r}} \psi(\boldsymbol{r}) \exp(-\mathrm{i}(\boldsymbol{q}\cdot\boldsymbol{r}))\,\mathrm{d}\boldsymbol{r} \tag{2.38}$$

$$= (\mathcal{F}\psi)(\boldsymbol{q}), \tag{2.39}$$

with the vectors $\boldsymbol{q} = (q_x, q_y)$ in the sample plane, $\boldsymbol{r} = (r_x, r_y)$ in the detector plane (both orthogonal to the beam axis), and the Fourier operator $\mathcal{F}$, which acts as free space propagator for the wave field from the sample plane to the detector plane.

The measurable quantity of $\Psi(\boldsymbol{q})$ in an experiment is the photon flux density $I_{\mathrm{ph}}(\boldsymbol{q})$, which is equal to the time average of magnitude of the poynting vector $\boldsymbol{S}$:

$$I_{\mathrm{ph}} = \frac{\langle|\boldsymbol{S}(\boldsymbol{q},t)|\rangle_t}{\hbar\omega}, \tag{2.40}$$

with $\hbar$ being the reduced Planck constant, ω the angular frequency of the photons, and $\langle.\rangle_t$ the time averaging operator.

The photon flux density $I_{\mathrm{ph}}(\boldsymbol{q})$ is proportional to the intensity $I(\boldsymbol{q})$ of the wave field. By convention, in the following we will solely use the intensity $I(\boldsymbol{q})$, when we are referring to the quantity recorded by the detector:

$$I(\boldsymbol{q}) = |\Psi(\boldsymbol{q})|^2. \tag{2.41}$$

$$= (\mathcal{F}\psi)^*(\boldsymbol{q})(\mathcal{F}\psi)(\boldsymbol{q}) \tag{2.42}$$

The expression for the far-field diffraction pattern $I(\boldsymbol{q})$ of the triple slits results from the following consideration. With Eq. 2.34 to 2.36 we write the triple slit exit wave $\psi(\boldsymbol{r})$ as the summation of the exit waves from the individual slits s_n:

$$\psi(\boldsymbol{r}) = \sum_{n=1}^{3} s_n(\boldsymbol{r}) \tag{2.43}$$

With eq. 2.42 the far-field intensity reads:

$$I(\boldsymbol{q}) = \sum_{n,m=1}^{3} S_n^*(\boldsymbol{q}) S_m(\boldsymbol{q}), \tag{2.44}$$

with

$$S_n(\boldsymbol{q}) = (\mathcal{F}s_n)(\boldsymbol{q}) \tag{2.45}$$

being an abbreviation for the Fourier transformation of the individual slits.

As we saw for the double slit experiment in chapter 2.1.1, the terms with $m = n$ equals the incoherent sum of the individual slit diffraction patterns. The mixed terms $m \neq n$ give the interference between the slits and modulate the incoherent summation of the single slits diffraction according to the phase difference between the slits. See Fig. 2.5 (middle) for an example of a triple slit diffraction pattern.

2.2.3 Analysis of Absorption and Dispersion

In this section, we will derive how the optical constants are determined from the measured interferogram. In the following, we assume fully coherent monochromatic light. To reconstruct the relative properties of the exit wave $\psi(\boldsymbol{r})$, we use an inverse Fourier transform $\mathcal{F}^{-1}$ onto the intensity $I(\boldsymbol{q})$, which yields the spatial autocorrelation:

$$\begin{aligned} a(\boldsymbol{r}) &= (\mathcal{F}^{-1}I)(\boldsymbol{r}) && (2.46)\\ &= \mathcal{F}^{-1}((\mathcal{F}\psi)^*(\mathcal{F}\psi))(\boldsymbol{r}) && (2.47)\\ &= (\psi^*(-\boldsymbol{\rho}) * \psi(\boldsymbol{\rho}))(\boldsymbol{r}), && (2.48) \end{aligned}$$

with $*$ denoting the convolution operator. For the last step in this equation, the convolution theorem was used.

With the exit wave from eq. 2.43, the spatial auto-correlation reads:

$$\begin{aligned} a(\boldsymbol{r}) &= \left(\sum_{m=1}^{3} s_m^*(-\boldsymbol{\rho}) * \sum_{n=1}^{3} s_n(\boldsymbol{\rho})\right)(\boldsymbol{r}) && (2.49)\\ &= \sum_{n,m=1}^{3} c_{n,m}(\boldsymbol{r}) && (2.50) \end{aligned}$$

The terms with $m = n$ belong to the auto-correlation of the individual slits, while for $m \neq n$ the cross-correlations $c_{n,m}(\boldsymbol{r})$ between the slits are summarized. Figure 2.5 summarizes the nomenclature for the triple slit reconstruction process.

For the reconstruction of the refractive index, the most important correlations are the cross-correlation between the material slit with one reference slit and the cross-correlation between both reference slits. With Eq. 2.33, the cross-correlation between the material and the first reference slit is:

$$\begin{aligned} c_{1,2}(\boldsymbol{r}) &= (s_1^*(-\boldsymbol{\rho}) * s_2(\boldsymbol{\rho}))(\boldsymbol{r}) && (2.51)\\ &= \left(\left[\psi_{\mathrm{in}}(-\boldsymbol{\rho})t_{\mathrm{mat}}(-\boldsymbol{\rho})e^{(-\beta kd)}e^{(-i\delta kd)}\right]^* * \left[\psi_{\mathrm{in}}(\boldsymbol{\rho})t_{\mathrm{ref},1}(\boldsymbol{\rho})\right]\right)(\boldsymbol{r}) && (2.52)\\ &= e^{-\beta kd}e^{i\delta kd}\int \psi_{\mathrm{in}}^*(\boldsymbol{\rho})t_{\mathrm{mat}}(\boldsymbol{\rho})\psi_{\mathrm{in}}(\boldsymbol{\rho}+\boldsymbol{r})t_{\mathrm{ref},1}(\boldsymbol{\rho}+\boldsymbol{r})\,\mathrm{d}\boldsymbol{\rho} && (2.53) \end{aligned}$$

The expression in Eq. 2.53 can be simplified if the illumination $\psi_{\mathrm{in}}(\boldsymbol{r})$ is approximated by a plane wave ψ_{c}:

$$\begin{aligned} c_{1,2}(\boldsymbol{r}) &= e^{-\beta kd}e^{i\delta kd}|\psi_{\mathrm{c}}|^2\int t_{\mathrm{mat}}(\boldsymbol{\rho})t_{\mathrm{ref},1}(\boldsymbol{\rho}+\boldsymbol{r})\,\mathrm{d}\boldsymbol{\rho} && (2.54)\\ &= e^{-\beta kd}e^{i\delta kd}|\psi_{\mathrm{c}}|^2 A^{1,2}(\boldsymbol{r}). && (2.55) \end{aligned}$$

If we evaluate the cross-correlation $c_{1,2}(\boldsymbol{r})$ at the position $\boldsymbol{r} = \boldsymbol{r}_{\max}$ where the transmission functions $t_n(\boldsymbol{r})$ fully overlap, we get $A^{1,2}(\boldsymbol{r}_{\max}) = A^{1,2}_{\max}$, and, therefore:

$$c_{1,2}(\boldsymbol{r}_{\max}) = e^{-\beta kd}e^{i\delta kd}|\psi_{\mathrm{c}}|^2 A^{1,2}_{\max}, \tag{2.56}$$

with $A^{1,2}_{\max}$ being the area of the smaller slit:

$$A^{1,2}_{\max} = \min\{\mathrm{area}(t_{\mathrm{mat}}), \mathrm{area}(t_{\mathrm{ref},1})\}. \tag{2.57}$$

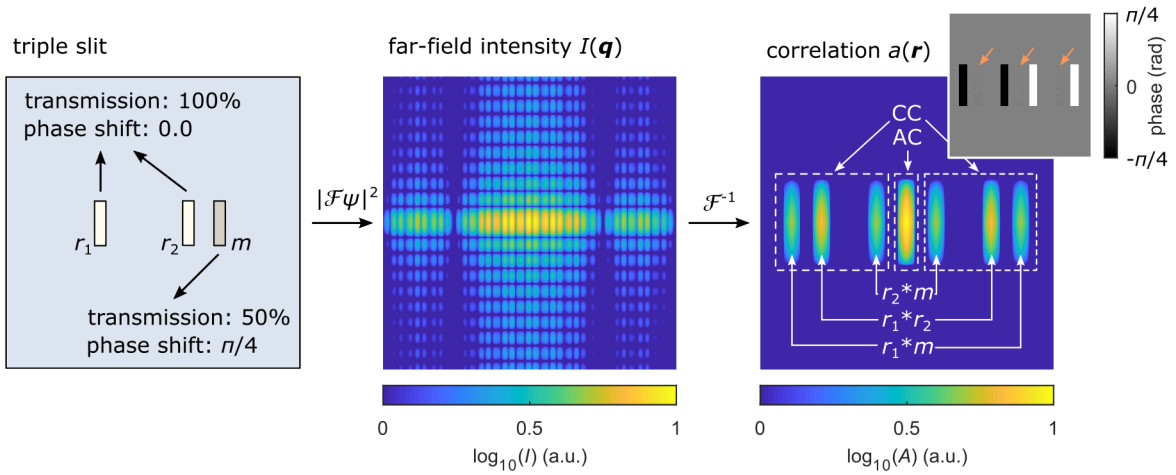

Figure 2.5: Nomenclature of the triple slit experiment. Both reference slits r_1 and r_2 transmit the incident light 100 % and do not alter the phase. In this simulation, the material slit m was set to absorb 50 % of the incident light and shift the phase by $\pi/4$ rad. The absolute value squared of the Fourier transform of the exit wave ψ gives the far-field diffraction $I(\boldsymbol{q})$. With an inverse Fourier transformation, one obtains the autocorrelation map $a(\boldsymbol{r})$. The dominant contributions to $a(\boldsymbol{r})$ are the auto-correlation (AC) and the cross-correlations (CC). The origin of the individual cross-correlations is marked by the correlation of the individual slits (e.g. $r_2 * m$ denotes the cross-correlation between the second reference slit r_2 and the material slit m). The inset in the upper right corner shows the phase of $a(\boldsymbol{r})$. Instead of seven correlations contributions, as for the amplitude, only four cross-correlations are non-zero. The missing correlations—marked by orange arrows—have zero phase and belong to the AC and the two correlations of $r_1 * r_2$.

Equation 2.57 accounts for the case in which both slits have different widths. A benefit of having slits with different widths is that the maximum value of the integral in Eq. 2.55 is not only given at the point $\boldsymbol{r} = \boldsymbol{r}_{\max}$, but at an interval with the size of the width difference of both slits. In this case, it can be averaged over the interval to obtain better statistics in the analysis of the optical indices. Therefore, different sized slits are the default aperture geometry used in our experiments. In the following, we will call the interval of $\max(A^{1,2}(\boldsymbol{r}))$ *cross-correlation plateau*.

The derivation of the twin image $c_{2,1}(\boldsymbol{r})$ of the cross-correlation $c_{1,2}(\boldsymbol{r})$ is identical to the derivation above. In the reconstruction $a(\boldsymbol{r})$, the cross-correlation and its twin image are separated by twice the distance between both slits s_1 and s_2. When designing the triple slit geometry, it is important to use a spacing between the slits, which is larger than half the size of the autocorrelation, to avoid overlapping of the correlations.

From Eq. 2.56, it is apparent that the optical constants are given by:

$$\beta = -\ln\left(\frac{|c_{1,2}(\boldsymbol{r}_{\max})|}{|\psi_{\mathrm{c}}|^2 A^{1,2}_{\max}}\right)\frac{1}{kd} \tag{2.58}$$

and

$$\delta = -i\ln\left(\frac{c_{1,2}(\boldsymbol{r}_{\max})}{|c_{1,2}(\boldsymbol{r}_{\max})|}\right)\frac{1}{kd} \tag{2.59}$$

Like many methods for the determination of the absorptive part of the refractive index, Eq. 2.58 contains the power $|\psi_{\mathrm{c}}|^2 A^{1,2}_{\max}$ of the incident radiation. With our method, we can utilize the cross-correlation between both reference slits $c_{2,3}(\boldsymbol{r}_{\max})$ to normalize $c_{1,2}(\boldsymbol{r}_{\max})$ as shown below.

With a similar derivation as for the material-reference cross-correlation, we arrive for the cross-correlation between both reference slits $c_{2,3}(\boldsymbol{r})$ at a similar equation as Eq. 2.55:

$$c_{2,3}(\boldsymbol{r}) = |\psi_{\mathrm{c}}|^2 \int t_{\mathrm{ref},1}(\boldsymbol{\rho}) t_{\mathrm{ref},2}(\boldsymbol{\rho}+\boldsymbol{r})\,\mathrm{d}\boldsymbol{\rho}. \tag{2.60}$$

For the position $\boldsymbol{r}_{\max}$, where the integral in Eq. 2.60 is maximal, we get the following equation:

$$c_{2,3}(\boldsymbol{r}_{\max}) = |\psi_{\mathrm{c}}|^2 A^{2,3}_{\max}. \tag{2.61}$$

We can use this reference cross-correlation value to normalize the cross-correlation between material slit and first reference slit $c_{1,2}(\boldsymbol{r}_{\max})$ from Eq. 2.56 in regards to the incident intensity:

$$c^{\mathrm{norm}}_{1,2}(\boldsymbol{r}_{\max}) = \frac{c_{1,2}(\boldsymbol{r}_{\max})}{c_{2,3}(\boldsymbol{r}_{\max})} \tag{2.62}$$

$$= e^{-\beta kd} e^{i\delta kd} \frac{A^{1,2}_{\max}}{A^{2,3}_{\max}}. \tag{2.63}$$

The geometric factor $A^{1,2}_{\max}/A^{2,3}_{\max}$ in Eq. 2.63 is equal to one if both vacuum slits have the same size or the smaller vacuum slit was used for the cross-correlation with the material slit. If the larger reference slit was used for the analysis of the cross-correlation, the

geometric factor $A^{1,2}_{\max}/A^{2,3}_{\max}$ can easily be corrected by the reciprocal ratio of the reference slit areas.

With the normalized material-reference cross-correlation, the optical constants can be reconstructed with:

$$\beta = -\ln\left(\frac{|c_{1,2}(\boldsymbol{r}_{\max})|}{|c_{2,3}(\boldsymbol{r}_{\max})|}\right)\frac{1}{kd} \tag{2.64}$$

and

$$\delta = -i\ln\left(\frac{c_{1,2}(\boldsymbol{r}_{\max})}{|c_{1,2}(\boldsymbol{r}_{\max})|}\right)\frac{1}{kd}. \tag{2.65}$$

Equations 2.64 and 2.65 only apply for samples with a single element present. During most experimental cases, the sample contains layers of various elements, even if only to support the layer to be examined. In these cases, Eqs. 2.64 and 2.65 describe an average over the full layer stack.

To calculate the refractive index in question, one needs to perform a control measurement $I'(\boldsymbol{q})$ of the sample without the layer of interest, in addition to the measurement $I(\boldsymbol{q})$ with all sample layers present. For the mathematical derivation, we use the prime symbol $'$ to denote quantities belonging to the control measurement. With multiple layers present, the exit wave from Eq. 2.26 becomes:

$$\psi(z,t) = \psi_0 \exp(i(k\sum_j n_j d_j - \omega t)), \tag{2.66}$$

with the index j running over all elements present in the sample layer. The derivation of the spatial auto-correlations $a(\boldsymbol{r})$ and $a'(\boldsymbol{r})$ follows the same argumentation we have seen before for a single layer. For clarity purposes, we will use the following definitions:

$$c_{\mathrm{m,r_1}} \coloneqq c_{1,2}(\boldsymbol{r}_{\max}) \tag{2.67}$$

and

$$c_{\mathrm{r_1,r_2}} \coloneqq c_{2,3}(\boldsymbol{r}_{\max}), \tag{2.68}$$

for the complex value of the cross-correlation plateau between the material slit and one reference slit and the cross-correlation plateau of both reference slits, respectively.

With $a(\boldsymbol{r})$ and $a'(\boldsymbol{r})$, one can show that the real and imaginary part of the refractive index of the investigated material layer, β_{mat} and δ_{mat}, becomes:

$$\beta_{\mathrm{mat}} = \left(\ln\left(\left|\frac{c'_{\mathrm{m,r_1}}}{c'_{\mathrm{r_1,r_2}}}\right|\right) - \ln\left(\left|\frac{c_{\mathrm{m,r_1}}}{c_{\mathrm{r_1,r_2}}}\right|\right)\right)\frac{1}{kd_{\mathrm{mat}}} \tag{2.69}$$

$$= \ln\left(\left|\frac{c'_{\mathrm{m,r_1}}}{c'_{\mathrm{r_1,r_2}}}\right|\left|\frac{c_{\mathrm{r_1,r_2}}}{c_{\mathrm{m,r_1}}}\right|\right)\frac{1}{kd_{\mathrm{mat}}} \tag{2.70}$$

and

$$\delta_{\mathrm{mat}} = i\left(\ln\left(\frac{c'_{\mathrm{m,r_1}}}{|c'_{\mathrm{m,r_1}}|}\right) - \ln\left(\frac{c_{\mathrm{m,r_1}}}{|c_{\mathrm{m,r_1}}|}\right)\right)\frac{1}{kd_{\mathrm{mat}}} \tag{2.71}$$

$$= i\ln\left(\frac{c'_{\mathrm{m,r_1}}\,|c_{\mathrm{m,r_1}}|}{c_{\mathrm{m,r_1}}\,|c'_{\mathrm{m,r_1}}|}\right)\frac{1}{kd_{\mathrm{mat}}}, \tag{2.72}$$

with d_{mat} indicating the layer thickness of the material of interest.

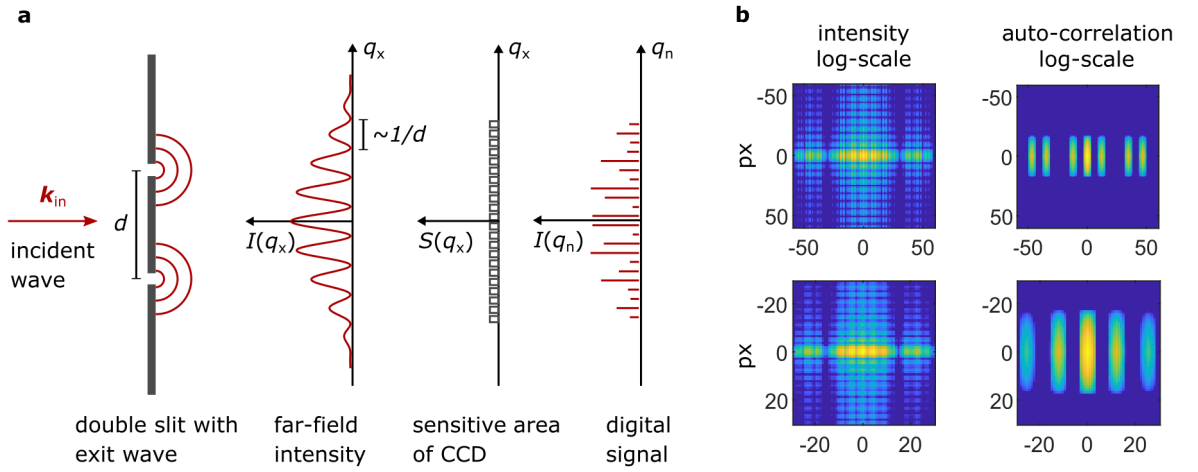

Figure 2.6: Consequences of sampling and undersampling a continuous diffraction pattern. **a** The two point sources from the double slit generate a far-field diffraction pattern $I(q_x)$. The dominant frequency is reciprocally dependent on the distance d between both point sources. To detect this frequency in the digital signal $I(q_n)$, the sensitive area of the CCD detector $S(q_x)$ (series of rect-functions) needs to sample the diffraction pattern by at least twice the frequency [28]. **b** The left column shows the far-field diffraction pattern of a triple slit, the right column shows the corresponding reconstructed auto-correlation. The upper diffraction pattern is sufficiently sampled. All three cross-correlations are visible in the reconstruction. The lower diffraction pattern is sampled with half the frequency. The corresponding reconstruction shows only the cross-correlation of the two closest slits. The interferometric information of the slits that are further apart is lost.

2.3 Digital Interferometry

The previous section dealt with the formation of the triple slit exit wave, the recording, and the reconstruction of the wave properties. These considerations were all done with continuous functions and variables. In this section, we will discuss the effects of digital sampling and discretization on the measuring and reconstruction process.

A pixelated detector, like a CCD, records a center rectangle of finite size of the triple slit far-field diffraction pattern $I(\boldsymbol{q})$. If the far-field approximation is reasonably fulfilled, the curvature of the Ewald's sphere[7] is close to zero over the detector area, so that no gnomonic distortion of the diffraction pattern occurs [27]. The center rectangle of the continuous diffraction pattern is sampled with a pixel spacing of s, yielding the diffraction pattern $I(\boldsymbol{q}_n)$, with the discrete reciprocal vector $\boldsymbol{q}_n$ (Fig. 2.6a).

Principally, the size of the detected rectangle $\max(\boldsymbol{q}_n)$ and the sampling rate $r_s = 1/s$ of $I(\boldsymbol{q}_n)$ have both an influence on the reconstruction quality. We will first discuss the effects of the finite size of the detected diffraction pattern on the reconstruction, followed by a discussion on the sampling rate. For an analogous discussion of these effects in digital

[7]The center of the Ewald's sphere is located at the scattering center. Its surface results from the wave vectors of all possible elastically scattered photons. If the surface from the Ewald's sphere deviates significantly from the flat detector surface, the momentum transfer q is sampled non-linearly [26]

holography, see [29].

One influence of $\max(\boldsymbol{q}_n)$, or, in other words, the maximum detected scattering angle, can be seen by multiplying the continuous $I(\boldsymbol{q})$ with the rectangular angular acceptance function $R(\boldsymbol{q})$ of the detector[8]:

$$\begin{aligned} a|_R &= \mathcal{F}^{-1}(IR) && (2.73)\\ &= \mathcal{F}^{-1}(\mathcal{F}a\mathcal{F}r) && (2.74)\\ &= a * r, && (2.75) \end{aligned}$$

with the reconstruction $a|_R$ based on the finite size of the detected diffraction pattern and r being the Fourier transformation of the detectors angular acceptance function R. With Eq. 2.75, we see that the reconstructed correlation function $a|_R(\boldsymbol{r})$ equals the true correlation function $a(\boldsymbol{r})$ convoluted with the Fourier transform of the detector shape $r(\boldsymbol{r})$. One can identify $r(\boldsymbol{r})$ with the point spread function (PSF) of the imaging system [29].

Another effect associated with the size of the physical detector is the achievable real space resolution. The larger the sampled area, i.e., the more higher spatial frequencies are measured, the higher the resolution in real space. Therefore, $R(\boldsymbol{q})$ can be referred to the numerical aperture of an imaging system [29].

For the reconstruction of the triple slit data, only the average values of the slit areas are of interest (see discussion to Eq. 2.55). Therefore, the reconstructed real space resolution is for the most part not an important parameter, except in one extreme case. If the real space resolution is not sufficient, to sample the smallest size of the cross-correlations by at least two pixels, signal loss will occur. Around this limit, the PSF will alter the correlation plateaus and the true amplitude and phase maxima might not be resolvable. Additionally, the noise surrounding the correlation will affect the amplitude and phase of the reconstruction [9].

For the effect of the sampling rate r_s of $R(\boldsymbol{q}_n)$ on the correlation function $a(\boldsymbol{r}_n)$, we will use the derivation we had previously used in a reciprocal sense. Instead of connecting the spatial expansion of the recorded diffraction pattern $I(\boldsymbol{q})R(\boldsymbol{q})$ with the resolution of the reconstruction $a(\boldsymbol{r}_n)$, we will connect the resolution, or sampling, of $I(\boldsymbol{q}_n)R(\boldsymbol{q}_n)$ to the reconstructed field of view.

Ideally, the sampling rate in the reciprocal space $r_\mathrm{s} = 1/s$ must be able to sample the highest modulation occurring in the diffraction pattern by at least twice the rate, which is known as Nyquist–Shannon sampling theorem [28]. The highest spectral component corresponds to the point sources in the sample plane, which are farthest apart. If these modulations are not sufficiently sampled, the information about the distance between both point sources becomes inaccessible. In the reconstruction space this leads to a decreased field of view (FOV)(Fig. 2.6b).

For the triple slit experiment, a relaxed version of the oversampling constraint is valid (Fig. 2.6b). As we saw in section 2.2.3, Eq. 2.64 and Eq. 2.65, only two cross-correlations—the reference cross-correlation $c_{2,3}$ and the correlations $c_{1,2}$ between the material slit and one reference slit—are needed for the reconstruction of the refractive indices. The third cross-correlations carries redundant information about the material slit. When the two

[8]The discrete sampling is omitted for simplicity reasons in the following calculation.

[9]For a typical experimental geometry presented in this thesis (see Fig. 1.1), the reconstructed real space pixels must be smaller than 500 nm.

corresponding slits are the one furthest apart, their spectral components do not need to be oversampled. Nevertheless, for most experimental conditions it is beneficial to use this redundant information for better signal-to-noise ratio (SNR).

Besides the FOV, the sampling rate also influences the spatial contrast distribution within the reconstruction $a(\boldsymbol{r}_n)$. As with the decrease in longitudinal coherence, visibility decreases when the higher frequency intensity modulations are sampled less. Since higher frequencies belong to higher distances in the sample, the contrast is reduced for slits that are further apart. This influence is described by the modulation transfer function (MTF), which can be calculated by the Fourier transform of the PSF of the detector. The PSF can be approximated by the area of one individual pixel. For a similar discussion of the MTF in digital holography, see [29].

Since the contrast reduction by the MTF is known, it can be corrected if necessary. In most experimental cases, however, it will be possible to select sufficient sampling.

Another consequence of the measuring process is the introduction of noise sources to the intensity signal $I(\boldsymbol{q}_n)$. Associated with the CCD, there are three major types of noise: dark noise, readout noise, and photon noise. The number of thermally generated electrons within the CCD is subject to statistical variations and is called dark noise. During the experiment, it is common to cool the CCD to reduce the dark noise. The readout noise dominantly arises from the pre-amplifier converting the CCD-charges to a voltage signal. The photon noise results from the quantum nature of light. Here, the detection probability follows a Poisson distribution.

Under illumination conditions, where the scattered intensity is low, certain areas of the diffraction pattern can become readout noise limited. In those regions, the readout noise will dominate the signal. Typically, the camera exposure time can be increased to collect more photons per pixel. However, two areas are particularly vulnerable to become readout noise limited. First, in regions with higher momentum transfer the scattering probability decreases. As we saw before, this affects only the resolution of the reconstruction, which is not as important for the experiment as the level information of the correlations plateaus. The second and more important case covers the areas where destructive interference occurs. If the destructive interference minima are cut off by the readout noise level, the level of the plateaus in the reconstruction will decrease. Therefore, it is important to make sure that the SNR especially at the interference minima is sufficiently high, or that the photon noise affects the plateaus less than the effect to be measured. The impact of low SNR at the interference minima on the data analysis will be discussed in greater detail in Ch. 5.3.

2.4 Magneto-Optical Constants

Besides the reconstruction of optical indices described previously in section 2.2.3, one main focus of the work presented is the spectroscopic and dynamic measurement of magneto-optical indices. The complex magneto-optical index describes the element specific influence of their magnetization $\boldsymbol{m}$ on circularly polarized light with angular momentum $\boldsymbol{l}_{\mathrm{ph}}$ through phase shift and absorption [30]. To describe this influence, the refractive index $n(\omega)$ from Eq. 2.25 is modified by a polarization and magnetization dependent correction term:

$$n_{\mathrm{circ}}(\omega) = n(\omega) - s(\Delta\delta(\omega) - i\Delta\beta(\omega)). \tag{2.76}$$

The absorptive and dispersive deviations from the refractive index for unpolarized light $n(\omega)$ are indicated by the magneto-optical indices $\Delta\beta(\omega)$ and $\Delta\delta(\omega)$, respectively. The scaling factor

$$s = d_\mathrm{p} d_\mathrm{m} \hat{\boldsymbol{l}}_\mathrm{ph} \cdot \hat{\boldsymbol{m}} \tag{2.77}$$

describes the strength and sign of the whole correction term. Here, $\hat{\boldsymbol{l}}_\mathrm{ph}$ stands for the unit vector along the direction of the angular momentum of the photons, $\hat{\boldsymbol{m}}$ for the normalized magnetization direction, and the constants d_p and d_m for the degree of polarization of the photon beam and for the degree of magnetic saturation in the sample layer, respectively. The sign of the correction term in Eq. 2.76 is defined by the scalar product $\hat{\boldsymbol{l}}_\mathrm{ph} \cdot \hat{\boldsymbol{m}}$.

For the majority of the experiments presented in this thesis, the effect of the magneto-optical constants is maximized by using sample magnetization parallel or anti-parallel to the angular momentum of the photons $\boldsymbol{l}_\mathrm{ph}$, as well as circularly polarized light ($d_\mathrm{p} \approx 1$) and saturated magnetization with $d_\mathrm{m} = 1$.

For the reconstruction of the magneto-optical indices $\Delta\delta$ and $\Delta\beta$, we measured the diffraction pattern $I^+(\boldsymbol{q})$ and $I^-(\boldsymbol{q})$ for both magnetization directions and fixed polarization direction of the light. (Equivalently, it would be possible to use right and left circularly polarized light with constant magnetization direction.) With the difference of both corresponding reconstructions, we can remove the influence of the magnetization independent part of the refractive index in Eq. 2.76 and calculate the magnetization dependent part. The derivation is analogous to Eqs. 2.70 and 2.72, where we subtracted the influence of supporting material layers. As a result, we get for the magneto-optical constants:

$$\Delta\beta = -\ln\left(\left|\frac{c^+_{\mathrm{m,r_1}}}{c^+_{\mathrm{r_1,r_2}}}\right|\left|\frac{c^-_{\mathrm{r_1,r_2}}}{c^-_{\mathrm{m,r_1}}}\right|\right)\frac{1}{2kd} \tag{2.78}$$

and

$$\Delta\delta = -i\ln\left(\frac{c^+_{\mathrm{m,r_1}}\,|c^-_{\mathrm{m,r_1}}|}{c^-_{\mathrm{m,r_1}}\,|c^+_{\mathrm{m,r_1}}|}\right)\frac{1}{2kd}, \tag{2.79}$$

where the subscripts $+$ and $-$ are indicating if the corresponding cross-correlations are belonging to the measurement with parallel or anti-parallel magnetization with respect to photon angular momentum.

2.4.1 Origin of the dichroic signals $I^+(\boldsymbol{q})$ and $I^-(\boldsymbol{q})$

As we have seen in the last paragraph, the diffraction patterns $I^+(\boldsymbol{q})$ and $I^-(\boldsymbol{q})$ differ from each other in terms of how strong the magnetization $+\boldsymbol{m}$ and $-\boldsymbol{m}$ affects the radiation. This dicroidic signal is described by the magnetic circular dichroism (MCD). For a thorough description of the MCD in the soft x-ray region and the interaction of polarized photons with matter, we refer the reader to [30].

In general, the MCD can be attributed to a difference in transition probability between spin-orbit split core levels and the exchange split valence states for different signs of $\hat{\boldsymbol{l}}_\mathrm{ph} \cdot \hat{\boldsymbol{m}}$ (Fig. 2.7). In [30], the MCD is described by a two-step model. First, in the presence of spin-orbit coupling, the angular momentum of the photon can be partly transferred to the

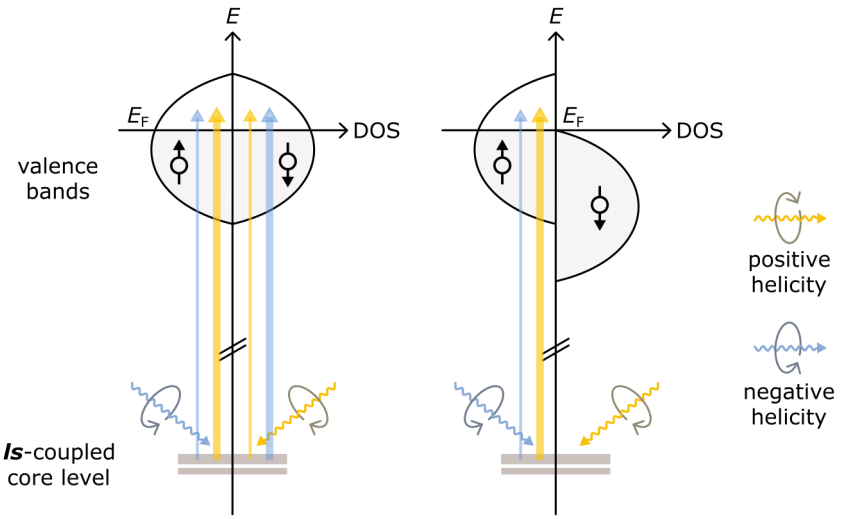

Figure 2.7: Illustration of the XMCD effect. Circularly polarized photons are absorbed in spin-orbit coupled core levels. The photoelectrons are spin-polarized and are excited to the free states above the Fermi-level. The amount of spin-polarization (indicated by the width of the transition arrow) is opposite for opposite photon helicity. The valence band on the left diagram shows no density of states (DOS) spin splitting and therefore no MCD contrast. The diagram on the right illustrates a valence band with Stoner splitting, chosen such that the "spin-down" channel is completely filled. Due to the Stoner-splitting the unoccupied DOS is higher for "spin-up" states. Therefore, the "spin-up" transition is much more likely to occur (adapted from [30]).

electron spin. Depending on the photon helicity, the photoelectrons are spin-polarized. A change in helicity results in opposite spin-polarization. In the second step, the asymmetry in the exchange split density of states (DOS) alters the transition probability in favour of the quantum number with the most unoccupied states.

The MCD effect occurs predominantly at absorption edges due to spin-orbit split core levels. This work investigates the M- and L-edges of Co and Fe, but dichroism can also be observed at the K-edge. For $3d$ transition metals, the energy of the M-edge resonance is located in the XUV range. Due to spin-orbit coupling, the $3p$ energy level of the $3p$–$3d$ transition splits up into a fine structure: $3p_{3/2}$ $(l+s)$ and $3p_{1/2}$ $(l-s)$. At the M-edge the transitions from the $3p$ fine structure overlap in absorption spectra, because of lifetime broadening.

At the L-edge, we are looking at the $2p$–$3d$ transition. The resonance energy for $3d$ transition metals is located in the soft x-ray regime. As for the M-edge, the $2p$ level has a fine structure due to spin-orbit coupling: $2p_{3/2}$ $(l+s)$ and $2p_{1/2}$ $(l-s)$. In contrast to the M-edge, here both levels are energetically sufficiently separated from each other to resolve them spectroscopically. Since the spin-orbit coupling has a different sign for both fine structure resonances, the spin polarization and therefore the sign of the XMCD effect will be opposite at those resonances.

2.5 Interferometric X-Ray Spectroscopy

The study of interferometric fringe patterns is employed to a wide range of applications, e.g. from atomic displacement measurements in surface structure analysis [31] to the 3D-mapping of earth's topography [32], or the observation of gravitational waves [33]. In general, interferometric instruments are categorized by their ability to create two light beams with different path lengths before they recombine at a recording device. Wavefront splitting interferometers divide the incident beam into two spatially separated parts [34]. Amplitude splitting interferometers use an optical element to reflect a fraction of the incident beams amplitude to create two beam paths [35]. Due to the refractive index in the XUV and x-ray range, effective beam amplitude splitters are not available for this energy range. Therefore, wavefront splitting interferometers are usually employed. The simplest implementation of wavefront splitting would be Youngs double-slit.

The Fresnel bimirror setup from [10] achieves wavefront splitting by reflecting parts of the beam under different angle. Coherent x-rays fall under grazing incidence onto two plane mirrors whose planes are tilted by a small angle. In the region where both reflected beams overlap, interference fringes do occur. When inserting a sample in one optical path, the interference pattern will shift. From the absolute shift of both measurements, δ can be deduced. This method depends on stable incident beam conditions and is prone to signal deterioration due to surface roughness and surface contamination.

The method presented in [13] inserts a 200 nm thick sample foil into one part of the incident beam, similar to the aforementioned Fresnel bimirror setup, but works in transmission. The interferometer is formed by two Fresnel zone plates behind the sample. The zone plates are arranged such that the first order diffraction of each zone plate interferes with the zero order of the other at the detector plane. By analysing the phase

shift and the intensity difference between the part with and without the foil, the complex refractive index can be calculated. Compared to this method, one advantage of our triple-slit method is that the sample layer is monolithically integrated into the interferometer, which ensures a less complex and more stable setup.

Another interferometric method utilizing zone plates is described in [11, 12]. Here, two optical elements, a binary grating and a zone plate, are combined. The coherent x-ray beam first passes the grating, which serves as beam splitter. The following zone plate focuses the two beams from the $(-1, +1)$ diffraction onto the sample mask. The sample mask consists of pairs of double-slits, in which one double-slit is free of any material and is used as reference and the other double-slit has one slit coated with a layer of the investigated material. The complex refractive index is calculated by comparing the far-field diffraction pattern of the reference double slit with the diffraction pattern of the double slit that contains the material coated slit. The interference shift is connected to the dispersive part of the refractive index, whereas the decrease in visibility depends on the absorptive part. This method is similar to ours, but on the one hand uses two more optical elements and, on the other hand, requires two successive measurements to determine the refractive index which makes it prone to alignment errors.

Instead of measuring the complex refractive index completely, some techniques rely on numerical models to iteratively approximate the complex refractive index partially or completely.

The point diffraction interferometry measurement described in [1] uses a setup similar to in-line holography to determine the dispersive part of the refractive index. A pinhole with a diameter between 50 µm to 100 µm is prepared in the center of free-standing foils with a diameter of 10 mm. The coherent XUV-light generated by a HHG source falls onto the foil. The center pinhole transmits a reference wave which interferes at the far-field detector plane with the wave transmitted through the foil. As the HHG-beam contains several harmonics, a grating behind the foil is used to spectroscopically resolve the diffraction patterns. From the interference minima, the dispersive part of the refractive index can be calculated. As there is no analytical procedure for the absorptive part, a numerical fitting approach was utilized. Based on the Huygens-Fresnel principle, the simulated diffraction patterns were iteratively fitted onto the measured diffraction pattern by a downhill simplex algorithm with β, the pinhole size, and the foil-detector distance as free parameters. An advantage of this method is that interferograms for different wavelengths can be recorded simultaneously.

Another iterative technique to approximate the complex refractive index at multiple wavelength is shown in [17]. Here, the diffraction from a single-layer of a self-assembled hexagonal array of polystyrene nano-spheres is simultaneously recorded for multiple harmonics of a HHG source. By non-linear least-square fitting the Mie-scattering intensities to the recorded data, the algorithm converges to β and δ. This technique is limited by the curvature of the phase front at the sample plane and the availability of nano-spheres matching the wavelength employed. In terms of data analysis, another advantage of our method is that we do not rely on iterative algorithms, but gain access to the complex refractive index after only one numerical operation (Fourier transformation).

CHAPTER 3

Experimental Details

In this chapter, we will describe in detail the physical properties of the sample systems we have investigated. In the following sections, we present the coherent light sources we used and discuss their properties in relation to the triple-slit experiment. We end this chapter with a description of the experimental setup.

3.1 Sample Systems

To demonstrate the spectroscopic and dynamic imaging properties of our triple-slit method, we used ferrimagnetic metallic alloys like GdCo or GdFe, and ferromagnetic multilayers like Co/Pt as sample systems. Motivated by an application perspective in data storage technology, these systems became scientifically relevant when it was discovered that short laser pulses can demagnetize the magnetic order in a sub-picosecond timescale [36]. Further experiments showed not only demagnetization but also permanent reversal of the magnetic order [37]. Despite major interest and ongoing research from experimental and theoretical scientists in these results [3, 4, 38–40], key questions about the underlying mechanisms of femtomagnetism have not yet been conclusively clarified, e.g., the angular momentum transfer in non-equilibrium states after optical excitation [41].

In most cases, the magnetic layers used are binary or multi-component systems, where it is important to separate the information about the individual elements spectroscopically. If one arranges the magnetic systems in the triple-slit configuration, one gets access to the element-specific and time-resolved complex electronic and magnetic responses of the system. Figure 3.1 shows such a typical triple-slit arrangement.

The triple-slits are prepared on commercially available silicon nitride (Si_3N_4) membranes which are supported by a silicon frame. In the first processing step, a gold layer is evaporated onto the Si_3N_4 membrane. This layer acts as opaque mask for the XUV and soft x-ray photons during the experiments. The height of the Au-layer is usually in the range of 1 µm. Afterwards, the material slit is processed into the gold film by focused ion beam (FIB). The sample and support layers are then applied to the Si_3N_4-layer by

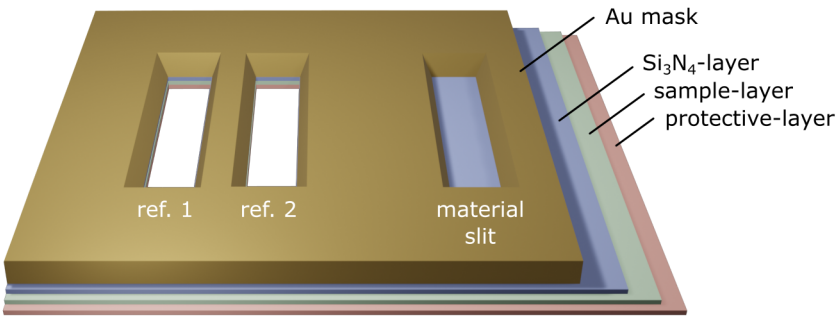

Figure 3.1: Basic triple-slit geometry. A thick gold layer masks the sample layers except where the three slits are present. Inside the reference slits, all other layers are removed, whereas they are still present inside the material slit. The layers beneath the gold mask contain a supporting Si_3N_4-layer, the sample layer and layers which act as protective structure against oxidation. In our experiments, the typical height of the slits is in the order of 10 µm. The width of the slits varied depending on the requirements of the individual experiments.

magnetron sputtering. The material slit is prepared before the magnetic sample layer is deposited to avoid possible changes to the properties of the magnetic sample layer by the Ga^+ ions used in the FIB process. In the last step, the two reference slits are milled via FIB. The height of the three slits ranges usually between 4 µm to 10 µm, the width between 0.5 µm to 3 µm. These parameters vary according to the requirements of the respective experiment and are described in detail in the respective chapters (Ch. 4 and Ch. 6).

As we have seen in Ch. 2.4, the maximum MCD contrast is obtained for parallel or anti-parallel orientation of magnetization and photon spin. Therefore, we aimed for an out-of-plane orientation of the samples magnetization combined with a perpendicular incidence of the beam. Perpendicular magnetic anisotropy for thin films can be tuned by the stoichiometry of the sample or the use of multilayer [42, 43]. In the following, we give an overview of the sample systems we have measured and which we present in this thesis.

3.1.1 $Gd_{25}Co_{75}$

With this sample, we are interested in the spectroscopic data of Co at the M-edge and of Gd at the N-edge to derive their correspondent magneto-optical constants. The sample layer had a total thickness of 30 nm. The atom percentages of the $Gd_{25}Co_{75}$ alloy sample layer are 25 % for Gd and 75 % Co. This relates to an integrated layer thickness of 15 nm for pure Co as well as 15 nm for pure for Gd. The 150 nm thick Si_3N_4 substrate was masked with a 1.1 µm thick $[Cr(5\,nm)/Au(50\,nm)]_{50}$ multilayer. The $Gd_{25}Co_{75}$ layer was seeded with 3 nm and capped with 2 nm Ta to prevent oxidation of the sample layer.

The three slits (vacuum, vacuum, $Gd_{25}Co_{75}$) were 4 µm in height (vertical) and 1 µm, 1 µm, 3 µm wide (horizontal), respectively. The distances between the slits were 9.6 µm (vacuum slit 1 to vacuum slit 2) and 4.5 µm (vacuum slit 2 to material slit), and chosen such that the cross-correlations in the reconstructions were not overlapping.

The magnetic hysteresis loops for this sample, measured by polar magneto-optic Kerr

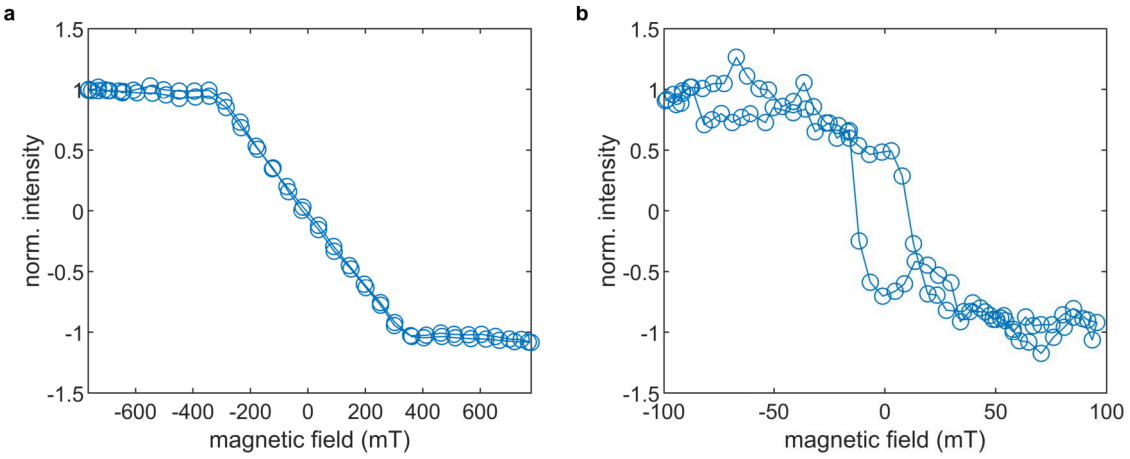

Figure 3.2: Magnetic hysteresis loops of the $Gd_{25}Co_{75}$ layer for out-of-plane (**a**) and in-plane (**b**) geometry measured by polar MOKE on a sister sample.

effect (MOKE) on a sister sample, are given in Fig. 3.2. Despite the intention during the sputtering process to get perpendicular magnetic anisotropy, the hysteresis of the $Gd_{25}Co_{75}$ reveals that the magnetic easy axis was in-plane (Fig. 3.2a) instead of out-of-plane (Fig. 3.2b). The out-of-plane magnetization of the sample saturates at 350 mT. The maximal external magnetic field strength that was possible during the triple-slit experiment was below this value. For the analysis of this data, an additional scaling factor for incomplete magnetization must, therefore, be taken into account (see Eq. 2.77).

3.1.2 $[Co(4)Pt(7)]_{\times 20}$

This sample was used to spectroscopically measure the magneto-optical constants of Co at the M- and L-edge. We used a $[Co(4)Pt(7)]_{\times 20}$ multilayer with a perpendicular magnetic anisotropy originating from the Co/Pt interfaces (Fig. 3.3). The Si_3N_4 membrane had a thickness of 200 nm and the gold mask consists of $[Cr(5\,nm)/Au(55\,nm)]_{20}$. The Co/Pt multilayer was seeded with Ta(2 nm) and capped with Pt(2 nm.

The triple-slit layout was different compared to the $Gd_{25}Co_{75}$ sample. Most importantly, we changed the two vacuum slits from having the same width to different width. This ensures that there are no sampling problems for the vacuum-vacuum cross-correlation during the spectroscopic measurements, as we will see in Ch. 4.2. The three slits (vacuum, vacuum, CoPt) were 2 µm in height (vertical) and 0.5 µm, 1.0 µm, 3.0 µm wide (horizontal), respectively. The distance between the slits was identical to the $Gd_{25}Co_{75}$ sample.

A similar multilayer was used in the time resolved small-angle scattering measurement, presented in section 6.1. We performed pump-probe measurements of the magnetic M-edge scattering from the magnetic domain network of a $[Co(8)/Pt(8)]_{\times 16}$ multilayer. The magnetic domains were aligned in a preferred direction with a demagnetization routine (demagnetizing the sample in an in-plane field caused by an alternating current) prior to the experiment to enhance the signal-to-noise ratio of the magnetic scattering on the detector.

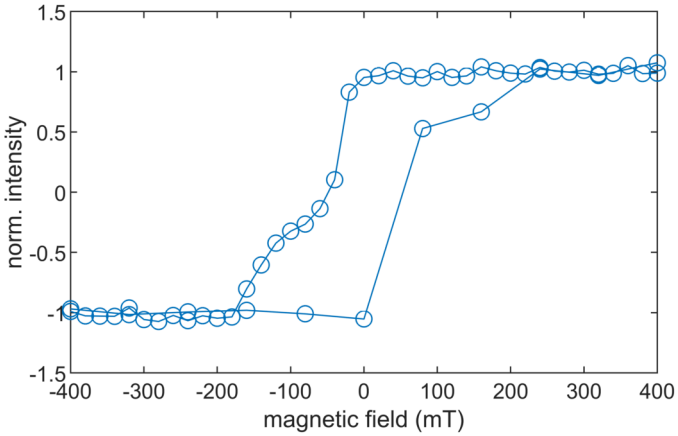

Figure 3.3: Magnetic out-of-plane hysteresis loop of the $[Co(4)Pt(7)]_{\times 20}$ multilayer measured by the triple-slit method.

3.1.3 Pure Co and Ta

With these samples, we aimed to reconstruct the optical constants of Co at the *L*-edge. The first sample system consists of a pure Co layer with 30 nm thickness with a 3 nm thick Ta layer above and below. The second sample had only one layer of Ta with a thickness of 3 nm. The data from the second sample was used as a reference measurement in order to separate the Ta signal from the Co signal in the first sample. Both samples had a 200 nm Si_3N_4 membrane and were masked with a $[Cr(5\,nm)/Au(55\,nm)]_{20}$ layer. The three slits (vacuum, vacuum, Co) were 2 µm in height (vertical) and 0.5 µm, 0.1 µm, 0.5 µm wide (horizontal), respectively. The distances between the slits were 2.1 µm (vacuum slit 1 to vacuum slit 2) and 1.0 µm (vacuum slit 2 to material slit).

3.1.4 $Gd_{25}Fe_{75}$ and $Gd_{28}Fe_{72}$

With the $Gd_{25}Fe_{75}$ sample, the Fe *M*- and *L*-edges as well as the Gd *N*-edge were investigated. The total layer thickness was 30 nm. The atom percentages of the $Gd_{25}Fe_{75}$ alloy sample layer are 25 % for Gd and 75 % Fe. This relates to a integrated layer thickness of 15.5 nm for pure Fe and 14.5 nm for pure Gd. The Si_3N_4 substrate and the gold mask had the same parameters as the $Gd_{25}Co_{75}$ sample. The hysteresis of this alloy is shown in Fig. 3.4 which indicates a perpendicular magnetic anisotropy. The geometry of the three slits were equal to the one of the $Gd_{25}Co_{75}$ alloy sample.

The experiment demonstrating the dynamic capabilities of our triple-slit setup used also a FeGd alloy as sample layer. The stoichiometry of this alloy was $Ta(3)/Gd_{28}Fe_{72}(40)/Ta(3)$, where the numbers in brackets represent the thickness in nanometer and the numbers behind the elemental symbols denote the atom percentage in the alloy. The sample layer was increased to 40 nm to increase the magnetic signal. To counter the limiting photon flux of the HHG source, the absorption in the Si_3N_4 was reduced by using a Si_3N_4 layer with only 10 nm layer thickness. The hysteresis of a sister sample is shown in Fig. 3.5. The magnetization of the sample saturates at a external magnetic field of 50 mT. The low saturation field has the advantage that the electromagnet inside the vacuum chamber can operate at a lower current. This significantly reduced the heat load in the immediate

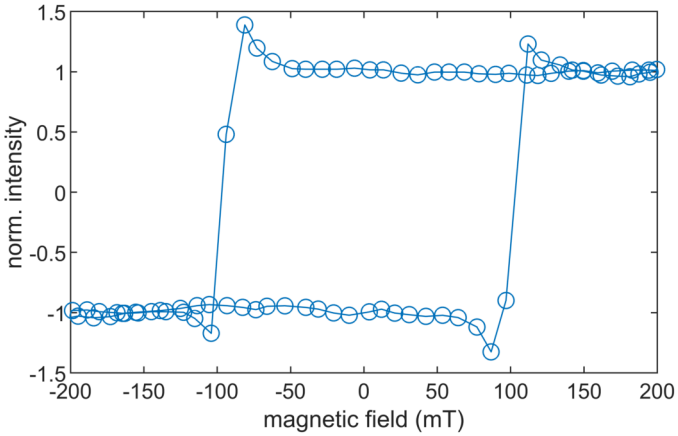

Figure 3.4: Magnetic out-of-plane hysteresis loop of the $Gd_{25}Fe_{75}$ multilayer measured by polar MOKE on a sister sample.

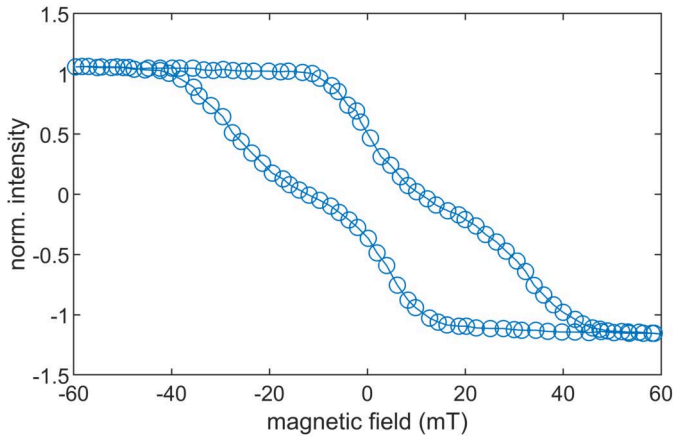

Figure 3.5: Magnetic out-of-plane hysteresis loop of the $Gd_{28}Fe_{72}$ multilayer used in the pump-probe experiment measured by polar MOKE on a sister sample.

vicinity of the sample.

3.2 X-Ray- and EUV-Sources

The data we present in this thesis were recorded at two different photon sources. In the case of the spectroscopic measurements, the experiments were performed at different beamlines of the BESSY II synchrotron source. The pump-probe measurements were carried out at a lab-based HHG source. In the following, we will first discuss the beamlines of the synchrotron sources.

X-Ray-Sources

The L-edge data was recorded at the UE52-SGM undulator beamline of BESSY II [44]. The beamline delivers linearly and circularly polarized light in a photon energy range from 100 eV to 1500 eV. For photon energies around the Co and Fe L-edge the energy

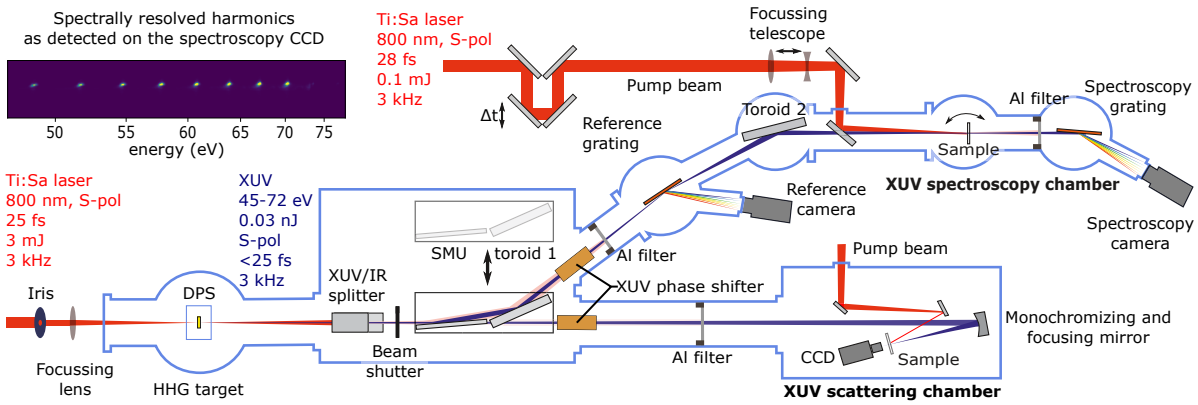

Figure 3.6: Schematic drawing of the HHG source. The blue line encircles the components in vacuum with pressures $< 1 \times 10^{-6}$ mbar. High-harmonics are generated in the HHG target by intense IR pulses which are consequently removed via the XUV/IR splitter and Al filters. The switching mirror unit (SMU) directs the XUV radiation to the spectroscopy endstation, or, if removed, lets the beam pass into the scattering endstation. The reference grating and camera are used for intensity normalization. A monochromizing and focusing mirror is used in the scattering chamber to define the incident wave on the sample. For the pump-probe experiment, the CCD is covered by an additional Al-filter. The inset in the upper left shows an image of the high harmonic spectrum. The figure was adapted from [46].

resolution was $E/\Delta E > 2000$. The reflective focussing optics of the beamline had a horizontal (vertical) divergence of 6 mrad (1 mrad) and achieved a minimal focus size in the order 50 µm. This results in a homogeneous beam profile on the area of the triple-slits in a distance of 100 mm from the focus. With a photon flux of 1×10^{11} ph s^{-1} in the aforementioned bandwidth, the experiment was not photon limited, even outside the focus position.

The M-edge data of the ferromagnetic samples and the N-edge data of Gd was taken at the UE112-PGM-1 undulator beamline of BESSY II [45]. The beamline offers variable polarization in a photon energy range of 8 eV to 690 eV. Around the M-edges of the investigated ferromagnetic samples, the energy bandwidth was 30 meV. For the Gd N-edge at 149 eV a energy bandwidth of 99 meV was obtained. The optimum beamline focus size was 80 µm both horizontally and vertically. At 63.5 eV the horizontal (vertical) divergence was 1.4 mrad (0.6 mrad). Like at the UE52-SGM beamlime, the experiment was not photon limited, as the photon flux was $>1 \times 10^{12}$ ph s^{-1} for the aforementioned bandwidth in the investigated energy interval.

XUV-Source

The time resolved IR-pump/XUV-probe measurements were carried out at a lab-based HHG-source located at the Max Born Institute [46].

An overview of the high harmonic generation setup is shown in Fig. 3.6. The driving IR beam of the XUV-HHG radiation was provided by a commercially available Ti:sapphire

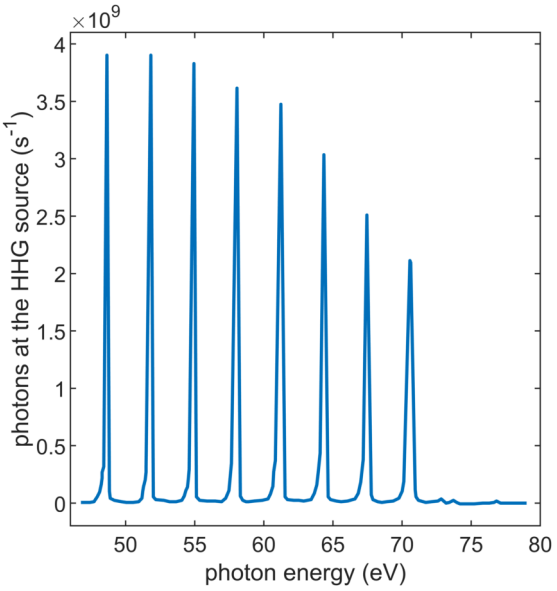

Figure 3.7: HHG spectrum of Ne gas calculated back to the source position (see [46] for details of the calculation). The spectrum has a cutoff at 72.6 eV due to the use of an Al-filter in the beam path. Figure from [46]

amplifier laser system (Coherent Legend Elite Due HE +USX). The pulses of 25 fs had a repetition rate of 3 kHz, a wavelength centred at 800 nm with a bandwidth of 80 nm, and a pulse energy of 2.9 mJ.

The non-linear process of the HHG depends on the temporal and spatial shape of the IR beam. In front of the 2 mm Ne gas target, both parameters were controlled by a motorized compressor for the beam pulse length, a motorized iris for filtering larger transverse vectors from the beam, and a focussing lens ($f = 1$ m).

After tuning the optimal phase matching conditions, we found the optimal gas pressure for maximal HHG to be 300 mbar. A differential pumping station around the HHG gas target allows for gas pressures up to 1 bar inside the gas cell and a pressure of around 10^{-5} mbar outside the gas cell. The areas in Fig. 3.6 encircled by the blue outline are under vacuum with a pressure of below 1×10^{-6} mbar.

The co-propagating IR light is attenuated by a XUV/IR splitter by 2–3 orders of magnitude [46]. The reduced IR light is subsequently blocked from entering the experimental chambers by 200 nm thick Al foils. The theoretical transmission of the XUV/IR splitter for XUV photons is 60 %. During our pump-probe experiments, we experienced a transmission decrease through the splitter unit, due to thermal damage to the mirror surfaces. We could increase the HHG flux by one order of magnitude by replacing the XUV/IR splitter by a small aperture (0.5 mm diameter) close to the entrance of the SMU chamber. As the IR beam had a higher divergence compared to the HHG beam this allowed to clip a portion of the IR beam without altering the HHG beam. After approximately 1 m propagation distance, the intensity of the remaining IR beam was sufficiently low to be blocked by a 200 nm Al filter without damaging the filter if the exposure time did not exceed times above 1 min. The exposure time was controlled by a fast shutter in front of the Al filter.

A motorized mirror switching unit (SMU, 4° grazing incidence) steers the XUV

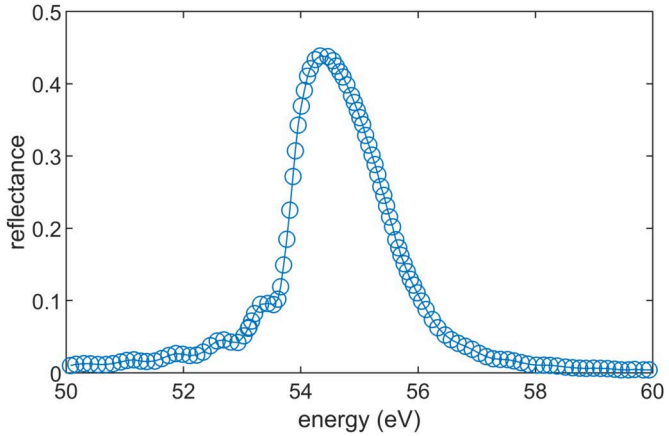

Figure 3.8: Reflectance of the multilayer mirror used in the pump-probe experiment of the $Gd_{28}Fe_{72}$ alloy (Measurement provided by the manufacturer).

beam either to the XUV spectroscopy chamber, or to the XUV scattering chamber. The spectroscopy beamline was used during our experiment only for beam diagnostics. Figure 3.7 shows a typical spectrum measured with the reference camera from the spectroscopy beamline. The total flux at the source is in the order of $3 \times 10^{11}\,\mathrm{ph\,s^{-1}}$ (calculated, see [46] for details). The pulses of odd harmonics have an energy spacing of 3.1 eV, with a photon energy bandwidth ΔE_{FWHM} of a single harmonic of approximately 200 meV[1]. As we used Al filter in our beamline for blocking the IR laser, the spectrum does not show harmonics beyond the Al L-edge around 72.5 eV. We utilized this known cut-off to calibrate the energy axis of the spectrum. For a more detailed description of this beamline, we refer the reader to [46].

A XUV phase shifter generated the circularly polarized XUV light. This yields an ellipticity of $p = 0.8$ at 45° rotation angle of the XUV phase shifter. The principle and the properties of the phase shifter are described in [46, 47]. The phase shifter is able to provide right and left circularly polarized light. In practice, this involves a rotation along the optical axis, which causes the beam to have small angular deviations from the optical axis. At the sample plane, this angular deviations can translate to a lateral beam shift in the order of 15 µm. Therefore, in the dynamic measurements, we have kept the polarization constant and changed the direction of the external magnetic field to change the sign of the XMCD contrast.

The distance from the HHG cell to the XUV scattering chamber equals 3.5 m. At this point, due to divergence (approximately 2 mrad at 60 eV), the XUV beam needs to be refocused. Additionally, our experiment requires monochromatic radiation instead of the spectrum of harmonics of Fig. 3.7. We used a spherical multilayer mirror ($f = 250$ mm) with a narrow band reflectivity under nearly normal incidence to select a single harmonic peak and refocus it onto the sample plane. The multilayer of the mirror used during the triple-slit experiment of the $Gd_{28}Fe_{72}$ alloy had a reflective maximum at 54.3 eV and a full width at half maximum (FWHM) bandwidth of (1.7 eV) (Fig. 3.8). The focus size was 10 µm (FWHM). To yield a reasonable homogeneity of the incident wave across the area

[1]Due to the reciprocal relationship $\Delta E_{\mathrm{FWHM}} \Delta \tau_{\mathrm{FWHM}} \geq 1.825\,\mathrm{eV \cdot fs}$ [25] between the energy bandwidth ΔE_{FWHM} and the pulse duration $\Delta \tau_{\mathrm{FWHM}}$, the theoretical lower limit of $\Delta \tau_{\mathrm{FWHM}}$ would be 9.1 fs.

Table 3.1: Estimation of the XUV transmission after all optical elements at the sample position. See [46] for details on the analysis of the transmission measurements. The transmission value for the Al filter transmission was taken from [48].

Element	XUV transmission in %
XUV/IR splitter	60
Phase shifter	20
Al filter (200 nm)	72
Spherical mirror	40
Total	4

of the triple-slits, while still maintaining sufficient photon fluence through the sample, the sample was placed 75 mm upstream from the focus position. At this position, the FWHM beam size was 80 µm. After all optical elements described above, the total photon flux of the harmonic centered around 54.3 eV incident at the sample position was approximately 1×10^8 ph s^{-1} (Tab. 3.1). Compared to the photon flux at the sample position, which was available at the UE112-PGM-1 undulator beamline of BESSY II, the photon flux of the HHG source is up to four orders of magnitude smaller. To achieve reasonable exposure times at the HHG source, it is, therefore, essential to use a smaller beam diameter on the sample. As we will see in Ch. 5.1 and Ch. 6.3, the smaller beam diameter in combination with the inhomogeneity of the beam profile with respect to the slit area increases the measurement errors caused by beam instabilities.

For the pump beam, a 5 % fraction was separated from the fundamental IR pulse. The pump-probe delay was introduced via a four mirror setup, where two mirrors were mounted on a linear translation stage. The pump intensity was controlled by a half-wave plate and two polarisers. The diameter of the pump beam on the sample was adjusted by two lenses and was typically around 350 µm (FWHM). Both pump and probe beams were actively stabilized by two motorized mirrors and a corresponding detector pair, located 3 m upstream of the XUV scattering chamber. The temporal overlap at the sample position was determined by detecting the sum-frequency generation of the fundamental IR that drives the HHG process and the IR pump beam from a barium borate (BBO) crystal as a function of pump-probe delay. This cross-correlation provides an upper limit for the temporal resolution of 50 fs.

3.2.1 Coherence

The ability to form interference patterns requires a well-defined phase and amplitude relationship throughout the illuminated area of interest. Depending on the light source, the well-defined phase and amplitude relationships of the radiated wave fields are limited in their spatial and temporal extension. This limitation is described by the degree of coherence. During the discussion about the reconstruction of the optical and magneto-optical constants in Ch. 2.2.1, we assumed that the part of the beam illuminating the area of the three slits is fully coherent. This assumption is an oversimplification, as the finite source size and its spectral bandwidth of every real physical illumination will limit

the region of coherence. In this section, we will discuss the impact of reduced degree of coherence on the analysis of triple-slit data and compare it to the coherence characteristics of HHG and synchrotron radiation.

In the most general way, the degree of coherence of an electric field at two different positions, r_1 and r_2, and times, t and $t+\tau$, is mathematically described by the mutual coherence function Γ:

$$\Gamma_{12}(\tau) = \langle E_1(t+\tau) E_2^*(t) \rangle. \tag{3.1}$$

Here, the scalar E_n stands for the electric field at the point r_n, τ denotes the time delay of the electric field between both points, and the square brackets symbolize a time averaging of the product of the two electric fields. With the local intensities $\langle |E_i|^2 \rangle$ at both points, the normalized complex degree of coherence is given by:

$$\gamma_{12}(\tau) = \frac{\Gamma_{12}(\tau)}{\sqrt{\langle |E_1|^2 \rangle} \sqrt{\langle |E_2|^2 \rangle}}. \tag{3.2}$$

For coherent radiation such as a plane wave with a well-defined frequency, the amplitude of the complex degree of coherence would be $|\gamma_{12}(\tau)| = 1$ at all combination of points and time delays, meaning that the wave field at point 2 after all time delays τ is fully determined by the wave field at point r_1. All real existing light sources approach this limit only in finite regions of coherence. In the following, we will discuss the influence of partial coherence on the ability to form interference patterns.

In Eq. 2.2, we assumed full coherence for the interference of a double slit diffraction pattern. Considering the normalized complex degree of coherence, we can rewrite the interference term as

$$2\sqrt{I_1 I_2} \cos(\phi_1 - \phi_2) = 2\sqrt{\langle |E_1|^2 \rangle} \sqrt{\langle |E_2|^2 \rangle} \operatorname{Re} \gamma_{12}(\tau), \tag{3.3}$$

where the real part of $\gamma_{12}(\tau)$ can be written as:

$$\operatorname{Re} \gamma_{12}(\tau) = |\gamma_{12}(\tau)| \cos(\arg \gamma_{12}(\tau)). \tag{3.4}$$

For $|\gamma_{12}(\tau)| < 1$, the contrast between the minima and maxima of the interference pattern will decrease compared to the contrast for full coherence while the modulation frequency of the diffraction pattern deviates from a pure cosine depending on the phase of $\gamma_{12}(\tau)$. It is common to separate the influence of partial coherence in a temporal and a spatial correlation of the electric field, as we will see in the following.

Temporal Coherence

As a measure of temporal coherence[2], one can define a temporal coherence length l_{coh}, in which the waves are expected to maintain their phase relation. Expressed in terms of the normalized complex degree of coherence (Eq. 3.2), this means that one is interested in the normalized complex degree of coherence $\gamma_{11}(\tau) \equiv \gamma(\tau)$ at the same point for different time delays.

[2]In the case of a well defined propagation direction, the temporal coherence is also called longitudinal coherence, to indicate the decomposition of coherence in a transverse and parallel part regarding the propagation direction.

One can connect $\gamma(\tau)$ via a Fourier pair to the normalized spectral density $s(\omega)$ of the wave field which is known as the Wiener-Khinchin theorem [49]:

$$\gamma(\tau) = \int_{-\infty}^{+\infty} s(\omega) \exp(-i\omega\tau)\, d\omega. \tag{3.5}$$

Depending on the shape of $s(\omega)$, be it a pure Gaussian or a random distribution inside a Gaussian envelope, the envelope of $\gamma(\tau)$ will change according to $\Delta\tau \propto 1/\Delta\omega$. This implies for the interference term in Eq. 3.3 that the characteristic time in which $\gamma(\tau)$ contributes significantly to the interference term is inversely proportional to the bandwidth of $s(\omega)$.

From this, we can derive the temporal coherence length l_{coh} if we consider the edge case in which only two frequencies contribute to the normalized spectral density $s(\omega)$ of the wave. With the assumption that a wave field with a given bandwidth of $\Delta\lambda$ will significantly dephase after 180° phase difference of $E_1(\lambda)$ and $E_2(\lambda + \Delta\lambda)$, the temporal coherence length l_{coh} can be given as a number N_{coh} of wavelengths:

$$l_{\mathrm{coh}} = N_{\mathrm{coh}}\lambda. \tag{3.6}$$

Over this distance, the spectrally shifted wave undergoes a half wavelength less, to satisfy the 180° dephasing criteria:

$$l_{\mathrm{coh}} = (N_{\mathrm{coh}} - \frac{1}{2})(\lambda + \Delta\lambda). \tag{3.7}$$

Solving for the expected number of coherent wave cycles gives:

$$N_{\mathrm{coh}} = \frac{\lambda}{2\Delta\lambda} + \frac{1}{2}. \tag{3.8}$$

Since usually $\Delta\lambda$ becomes very small against λ, the 1/2 term can be neglected compared to the first term. If N_{coh} is inserted into Eq. 3.6, the coherence length becomes:

$$l_{\mathrm{coh}} = \frac{\lambda^2}{2\Delta\lambda}, \tag{3.9}$$

as it is commonly defined in textbooks, e.g. [25].

For the experiments at the HHG source, the harmonic centred at 54.3 eV, which had a FWHM bandwidth of 0.2 eV, was used. Note that the bandpass of the multilayer mirror (Fig. 3.8) is about an order of magnitude larger than the harmonic bandwidth and thus does not affect the coherence length. For the harmonic at 54.3 eV, Eq. 3.9 results in a coherence length of 3.1 µm. The maximal slit separation was 13 µm with the CCD detector (2048 px × 2048 px, 13.5 µm edge size) placed 75 mm downstream of the slits. For this setup, the maximal possible path length difference from both slits to a position on the detector was 2.4 µm. Since during the HHG experiment the triple-slit diffraction pattern was only visible on a quarter of the detector area due to the signal-to-noise ratio, the coherence length of the HHG source provided sufficient interference contrast.

The radiation emitted from the soft x-ray undulator beamlines is spectrally filtered by a monochromator, which provides a spectral purity of $E/\Delta E > 2000$. The resulting coherence length was, therefore, not a limiting factor during our experiments, even at the

L-edges of Fe and Co, where the wavelengths are shorter compared to their M-edges, but the scattering angles are also smaller.

As we have seen in Ch. 2.1.2, our triple-slit method is closely related to Fourier transform holography (FTH). In FTH, it can be shown [50] that the decreasing coherence length deteriorates the resolution of the reconstructed object. For a nanoscale imaging technique, this deterioration means a strong limitation. In our method, however, a reduced coherence length is less limiting, as we are not interested in the resolution of spatial information, but only in the amplitudes and phases of the plateaus of the slit's cross-correlations (see discussion to Eq. 2.55 in Ch. 2.2.3).

Spatial Coherence

A measure for significant phase correlation of quasi-monochromatic radiation from an extended source of independent emitters orthogonal to the propagation direction is given by transverse coherence length l_{trans}. If only this transverse property of the wave correlation is considered, the normalized complex degree of coherence $\gamma_{12}(\tau)$ becomes for $\tau \to 0$:

$$\gamma_{12}(0) = \frac{\langle E_1(t) E_2^*(t) \rangle}{\sqrt{\langle |E_1|^2 \rangle} \sqrt{\langle |E_2|^2 \rangle}} \tag{3.10}$$

$$\equiv \mu_{12}. \tag{3.11}$$

Analogous to the applicability of the Wiener-Khinchin theorem for the temporal degree of coherence $\gamma(\tau)$ in Eq. 3.5, the degree of spatial coherence μ_{12} of quasi-monochromatic radiation from a distribution of uncorrelated emitters, observed in the far-field, is linked to the distribution of the source intensity via a Fourier transformation. This relationship is described by the van Cittert-Zernike theorem [25]. In the following, we will consider the normalized degree of coherence μ_{O1} between a point O at the origin of the (x, y, z) coordinate system and another arbitrary point $\boldsymbol{r}_1 = (x_1, y_1, z = 0)$ in the observation plane. The source plane, indicated by the coordinates (χ, η), is parallel to the observation plane and located in the far field in a distance $z = z_0$ to the observation plane. This results in the following representation of the van Cittert-Zernike theorem:

$$\mu_{\mathrm{O1}} = e^{(-i\Psi)} \int_{-\infty}^{+\infty} I_{\mathrm{norm}}(\chi, \eta) e^{ik(x_1\chi + y_1\eta)/z_0} \, d\chi \, d\eta, \tag{3.12}$$

with $I_{\mathrm{norm}}(\chi, \eta)$ standing for the normalized source intensity distribution, and $\Psi = k(x^2 + y^2)/2z$ giving the geometrical property of the phase oscillation, when altering the distance between the points 1 and the origin.

Analogous to the reciprocal connection between the bandwidth $\Delta\omega$ and the coherence time $\Delta\tau$ in Eq. 3.5, one can reciprocally connect the spatial extension w_0 of the source with the transverse coherence length l_{trans}:

$$l_{\mathrm{trans}} = \frac{\lambda z}{4\pi w_0}. \tag{3.13}$$

If the uncorrelated emitters have the intensity distribution of a Gaussian with standard deviation of w_0,

$$I = I_0 \exp\left(-\frac{r^2}{2w_0^2}\right), \tag{3.14}$$

the normalized degree of spatial coherence is given by evaluating Eq. 3.12 for this Gaussian distribution [25]:

$$\mu_{O1} = \exp(-i\Psi) \exp\left(-\frac{(kw_0 r_1)^2}{2z^2}\right). \tag{3.15}$$

Using the transverse coherence length $r_1 = l_{\text{trans}}$ in Eq. 3.15, the normalized degree of spatial coherence becomes:

$$|\mu_{12}| = \exp(-1/8) \approx 0.88. \tag{3.16}$$

This means that within one coherence length l_{trans}, the partial spatial coherence of a Gaussian intensity distribution does not reduce the amplitude of the interference term from Eq. 3.3 by more than 88 % as long as the far-field approximation is fulfilled.

For our triple-slit experiment, we need a high degree of spatial coherence over the area of the slits, which is in the order of 10 µm. The spatial coherence of the HHG radiation is largely due to the fully coherent driving IR laser field [25]. Although the gas atoms participating in the HHG process are randomly distributed, the gas atoms radiate with a fixed phase relationship to the driving IR field and thus to each other. This causes the harmonics to add up constructively in the forward direction, generating radiation proportional to the square of the number of atoms participating in the HHG process. Studies of spatial coherence have shown that HHG radiation has a high degree of spatial coherence across most of the XUV beam's diameter [51–53]. However, some factors of the HHG can reduce the spatial coherence. From Eq. 3.13, it follows that the wavelength and focus size of the driving laser directly influence the transverse coherence length. In addition, the gas type and gas pressure of the HHG influence the relative phase velocities of the IR and the high harmonics, which leads to dephasing and a subsequent reduction of coherence. A further disturbance of the IR phase front is caused by the non-uniform generation of free electrons in the interaction region of the driving IR and the gas volume [51, 52].

During our HHG experiment, we optimized the set of values for gas pressure and gas type, IR focus size, and IR laser intensity (see Ch. 3.2) to achieve a large dephasing length and high spatial coherence. The fact that the size of the triple-slit apertures is smaller than the XUV beam diameter at the sample position (sufficiently beyond the focus position), further increases the spatial coherence. This is also known as spatial filtering. From Eq. 3.13 and the the divergence half angle $\theta_{\text{trans}} = l_{\text{trans}}/z$, or more generally $\theta = r/z$, the following statement can be obtained:

$$w_0\theta \geq \frac{\lambda}{4\pi}. \tag{3.17}$$

Radiation to which the equals sign in Eq. 3.17 applies, is called diffraction limited. This limit can be approached, for example, by lasers with intra-cavity mode control operating in the TEM_{00} mode [54], or, more generally, by using a pinhole-aperture combination that restrict either the beam waist w_0 or the divergence half angle θ, or both simultaneously. With a slit size of maximal $10 \times 3,$ µm, a maximal slit distance of 10 µm and a beam diameter of 80 µm (FWHM) at a distance of 70 mm from the focus (10 µm FWHM), in addition to the optimization of the HHG parameters spatial coherence was not a limiting factor for our HHG experiment.

For undulator radiation, the degree of spatial coherence is optimized by spatial filtering inside the beamline. As described for the HHG experiment, the triple-slit aperture size compared to the beam diameter at the sample position at sufficient distance from the beamline focus represents another spatial filter. Due to the high photon flux of undulator radiation, the optimization of the sample position in relation to the beamline focus ensures that spatial coherence does not become a limitation for our interferometric measurements without the photon flux through the triple-slit apertures becoming insufficient.

As we have seen for the temporal coherence, its influence on the triple-slit analysis can be described by a comparison with FTH. In [50], it was shown that a reduction of spatial coherence reduces the contrast of the FTH reconstruction. For our triple-slit method, a reduction of the reconstruction contrast, i.e., the height of the triple-slit cross-correlations plateaus, is directly related to an absorption change in the sample layer.

In the next section, we will investigate in more detail the impact of partial coherence onto the analysis of the triple-slit experiment.

Partial Coherence and Triple-Slit Data Analysis

In this section, we will estimate the influence of three different factors on the degree of coherence and discuss the corresponding parameter intervals in which our interferometric experiment is not significantly affected by these error sources. These factors consist of a spatially extended source of independent emitters (mainly associated with undulator radiation), radiation with a photon energy bandwidth ΔE (associated with HHG radiation), and a relative drift between beam, sample, and detector on a time scale shorter than the exposure time of a diffraction pattern. For this purpose, we simulate a triple-slit experiment using a 30 nm $Gd_{25}Fe_{75}$ sample layer as described in Ch. 3.1.4 at a center photon energy of 54.3 eV and look at the partial coherence effects on the reconstructed amplitude and phase of the triple-slit exit wave. The main focus of the simulation is its comparability to the HHG experiment, since this radiation source has a lower photon energy resolution and less stable relation between beam, sample, and detector then the undulator source we used. The error estimation for the extended source volumes applies for both HHG radiation and synchrotron radiation if spatial filtering is not sufficient, i.e., the sample positions is too close to the focus.

Figure 3.9a displays an overview of both the simulated geometry[3] of the experiment and the different origins of decoherence. The extended volume of the source causes light from different directions to reach the slits. This lowers the spatial coherence. We simulated this decrease of spatial coherence by changing the incident wave front from a fully coherent TEM_{00} mode into an incoherent sum of four different orthonormal Laguerre-Gaussian modes, (00), (01), (10), and (11), and scaling their respective occupancy[4]. In order to keep the simulation dependent on only one parameter, we decided to define the occupancy of the modes according to a fixed ratio among each other and to scale only their total fraction of the total intensity by the scaling parameter s. In concrete terms this means that the modes were occupied as follows: $s{\cdot}10\,\%$ of the intensity were in the (10) mode,

[3]For clarity, only two slits with the corresponding diffraction pattern are shown in Fig. 3.9a. For the simulation, three slits were used with dimensions as described in Ch. 3.1.4.

[4]See discussion to Eq. 3.17 and [54] for more information regarding Laguerre-Gaussian modes and degree of coherence.

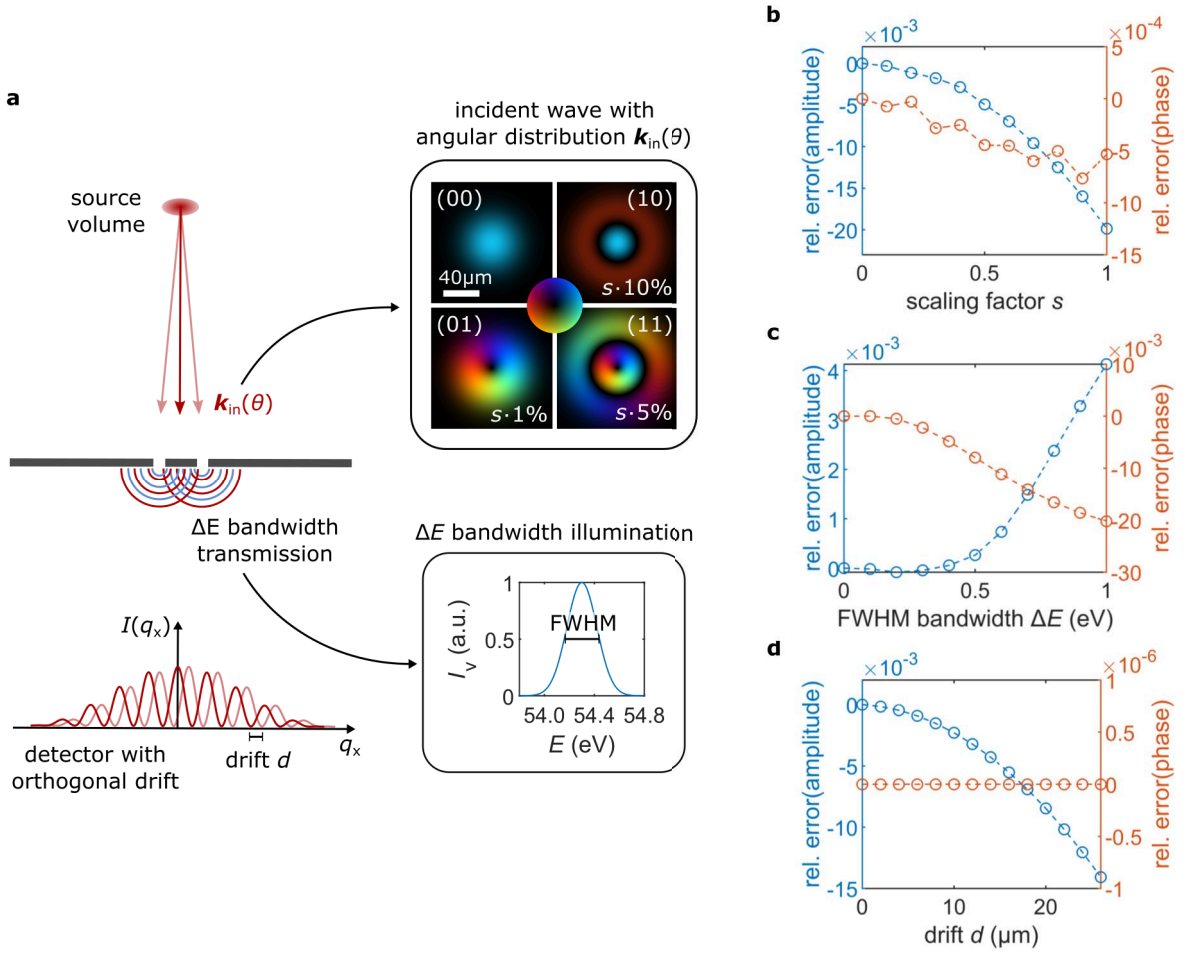

Figure 3.9: Simulated impact of partial coherence on the triple-slit reconstruction. Three different origins of incoherence were considered independently: An extended volume of emitters which leads to an angular distribution of $\boldsymbol{k}_{\mathrm{in}}(\theta)$, the magnitude of the the photon energy bandwidth ΔE, and a relative drift d between sample and detector (distance sample-detector $z_0 = 70\,\mathrm{mm}$). **a** Drawing of the simulation geometry. The three sources of partial coherence are indicated. The angular distribution of $\boldsymbol{k}_{\mathrm{in}}(\theta)$ in the incident beam is simulated by a incoherent sum of the first four normalized Laguerre-Gaussian modes (00), (10), (01), and (11). The four modes are shown with amplitude given as brightness value and phase as hue. The corresponding color wheel is positioned in the center of the four modes. The variable modes occupancy is given as percentage of the total intensity and scaled by the factor s. The occupancy of mode (00) is determined by the residual intensity fraction. The FWHM photon energy bandwidth ΔE had its center energy at 54.3 eV and ΔE scaled from 0 eV to 1 eV. **b-d** Relative error of the reconstructed amplitude and phase for different mode occupancies (**b**), variation of the bandwidth ΔE (**c**), and the relative drift between sample and CCD (**d**).

$s{\cdot}5\,\%$ in the (11) mode, and $s{\cdot}1\,\%$ in the (01) mode. The remaining intensity was used for the primary (00) mode. For the mode occupation ratio, we have oriented ourselves on values from the literature [55] concerning undulator radiation.

For the simulation, the scaling factor s was varied from 0 to 1 (Fig. 3.9b). The reconstructed phase is not strongly influenced by a reduction in spatial coherence. The relative error stays even for a scaling factor $s = 1$ under $1\,‰$. By reducing spatial coherence, the interference contrast is generally reduced, but the position of the interference minima and maxima remain largely unchanged. This explains why the reconstructed phase is less affected by a reduction in spatial coherence, since it depends more on the modulation frequency of the interference term. The reconstructed amplitude will deviate more than $1\,\%$ from the ground truth, when the scaling factor $s > 0.7$. This mode occupancy describes radiation from a undulator beamline with lower spatial coherence [55]. The reduction of spatial coherence through the possible occupancy of higher modes does also not pose a problem for the measurement with HHG radiation, since the coherent beam properties of the driving IR laser are largely transferred to the HHG beam (see discussion about spatial coherence in Ch. 3.2.1 and [25]). From this simulation, we can see that under normal conditions and with the degree of spatial filtering we have used during the experiments with HHG radiation and synchrotron radiation, spatial coherence is sufficient for the reconstruction of amplitude and phase of the exit wave.

The next simulated degeneration of full coherence is a decrease of temporal coherence through a photon energy bandwidth ΔE (FWHM) of the incident wave. The bandwidth ΔE was assumed to be Gaussian with a mean value around 54.3 eV. For the simulation, the bandwidth ΔE was varied from 0 eV to 1 eV. Figure 3.9c shows the relative error of amplitude and phase as a function of bandwidth. It can be seen that, in contrast to a reduction in spatial coherence, a reduction in temporal coherence has a stronger influence on the phase. A bandwidth of $\Delta E > 0.5\,\mathrm{eV}$ ($E/\Delta E < 108.6$) results in a relative phase error of $> 1\,\%$. The relative error of the amplitude, on the other hand, is much more stable against larger bandwidths ΔE. The radiation of the HHG source had the largest bandwidth $\Delta E = 0.2\,\mathrm{eV}$ of the experiments presented here. As we can see from Fig. 3.9c the relative error for a bandwidth $\Delta E \leq 0.2\,\mathrm{eV}$ is negligible.

The last of the three simulated reasons for decoherence is a relative drift between sample and detector (distance sample-detector $z_0 = 70\,\mathrm{mm}$). If this drift occurs on shorter time scales than the exposure time of a single diffraction image, the visibility of the interference pattern will decrease in the direction of the drift. This effect is similar to that of reduced spatial coherence in this direction [56]. With a reduced degree of spatial coherence, the detector is illuminated at the same time from different directions. In case of a point source, this illumination from different directions could occur over the duration of the detector exposure time due to the relative drift of sample and detector. Even if the sample and detector are stable over time, drift may occur as the incident beam moves across the sample [57]. If the wavefront of the incident beam is curved, the beam movement in relation to the slits causes them to be illuminated with $\boldsymbol{k}$-vectors from different angles. This has the effect that the diffraction pattern moves on the detector and reduces the interference visibility[5]. Figure 3.9d shows the relative error of the reconstructed amplitude and phase as a function of the relative drift between sample

[5]Both the effects of stationary curvature of the incident wave front and lateral drift are discussed in the Ch. 5.1.

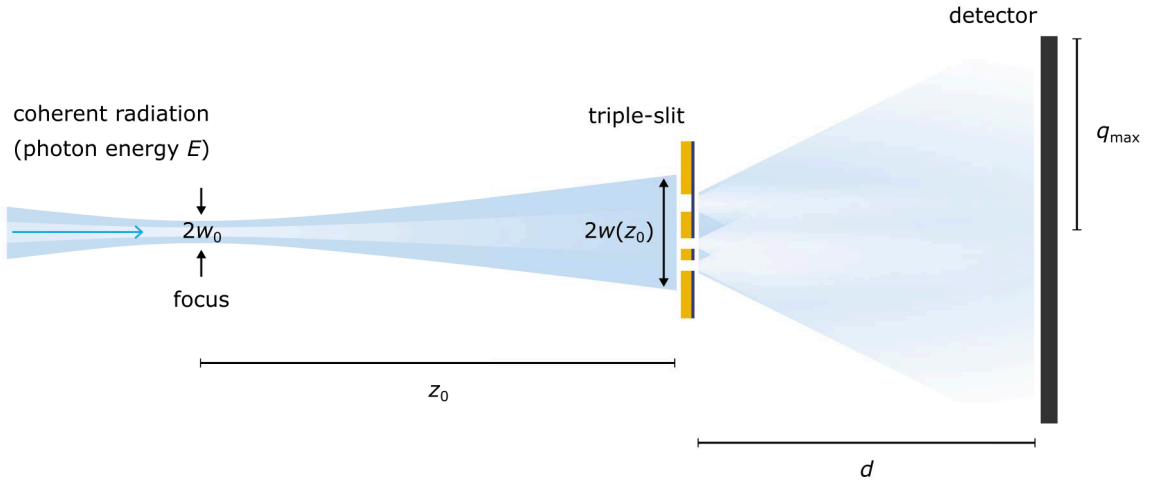

Figure 3.10: Sketch of the basic scattering geometry employed at the HHG source and the synchrotron beamlines UE112-PGM1 and UE52-SGM of BESSYII. This figure assigns the parameters of the scattering experiment, which are given in Tab. 3.2 for the three different radiation sources, to the scattering geometry: At the focus position the FWHM beam diameter with photon energy E is given by $2w_0$. The sample is located in a distance z_0 to the focus. The FWHM beam diameter on the sample is given by $2w(z_0)$. The distance between sample and detector is denoted by d. The maximum scattering angle recorded by the detector is given by q_{max}.

and detector for a sample-detector distance $z_0 = 70\,\mathrm{mm}$. As expected, the curves are qualitatively very similar to the one for the decrease of spatial coherence in Fig. 3.9b. However, this time the reconstructed phase is not disturbed by the relative drift. This is an indication that the relative drift does not change the position of the interference maxima and minima. The reconstructed amplitude, on the other hand, is affected by the relative drift. The pixel size of the simulated detector was $13.5\,\mu\mathrm{m}$. In terms of pixel size, a drift of $2\,\mathrm{px}$ will lead to a relative error of the amplitude of $\approx 1\,\%$. For a stable source with high photon flux, like for synchrotron radiation, this does not pose a significant problem. For HHG radiation with its lower photon flux, however, the exposure time can reach values where the inherent drift of the experiment will become a significant source of amplitude error. Therefore, during the HHG experiment, a trade-off between the drift error due to too long exposure times and the shot noise error due to too short exposure times must be found.

3.3 XUV Scattering Chamber

Most of the experiments presented in this thesis were performed with the XUV scattering chamber constructed and commissioned in the frame of this thesis (Fig. 3.11). We have designed this chamber to be highly flexible for various experimental geometries and photon sources. Both experiments with synchrotron radiation and HHG-XUV light were performed with the XUV scattering chamber as endstation, with exception of the L-edge measurements. Here, we used the MAXI vacuum chamber of the Max Born Institute as

Table 3.2: Parameters associated with the basic scattering geometry (Fig. 3.10). For the three different radiation sources used in our experiments, the energy E, the FWHM beam diameter $2w_0$ in focus, the distance between focus and sample z_0, the FWHM beam diameter $2w(z_0)$ on the sample, the distance between sample and detector d, and the maximum scattering angle $q_{\max}$ that can be measured by the detector are given. The focus size of the beam from UE112-PGM1 and UE52-SGM was taken from [44, 45].

source type	E (eV)	$2w_0$ (µm)	z_0 (mm)	$2w(z_0)$ (µm)	d (mm)	$q_{\max}$ (1/µm)
HHG	54.3	10	70	80	75	50
UE112-PGM1	45–75 135–170	80 (opt.)	100	≈ 190	135	23–39 70–88
UE52-SGM	770–800	≈ 60	≈ 50	> 250	720	75–78

endstation. For a description of the MAXI vacuum chamber, we refer to [58, 59]. A sketch of the basic scattering geometry employed at the HHG source and synchrotron sources is given in Fig. 3.10. All relevant parameters associated with the scattering geometry are summarized in Tab. 3.2. In the following, we will describe the instrumentation of the XUV scattering chamber in the spectroscopic and dynamic triple-slit experiments, as well as in the small-angle scattering pump-probe experiment.

At the bottom of the XUV scattering chamber, a 500 mm × 800 mm in-vacuum optical breadboard allowed to freely arrange the required experimental instruments. Figure 3.11a shows the configuration for the pump-probe measurements at the HHG-source. The spherical multilayer mirror (custom order, optiX fab, Germany), described in section 3.2, refocuses the XUV beam. The multilayer is specifically designed to reflect only the harmonic needed for the experiment. The angle between the incident and reflected XUV is minimized to avoid off-axis aberrations.

The sample holder can be moved in all three translation axes by a piezo-driven stage (SmarAct GmbH, Germany) to align the sample inside the 3 mm gap of an electromagnet. The electromagnet was able to generate a magnetic field up to a magnetic flux density of 230 mT with a current through the coils of 4 A. Both the electromagnet and the piezo-stage were mounted on a three-axes stepper-motor stage (Standa Ltd, Lithuania) and could be moved relative to the focus of the XUV beam to adjust the spot size on the sample.

The back-illuminated in-vacuum CCD camera (GE-VAC, Greateyes GmbH, Germany) detects the diffraction pattern with a raster of 2048 px × 2048 px of 13.5 µm edge size and an electronic readout depth of 16 bit. During the experiment, the CCD is cooled down to −40 °C to reduce thermal noise. The detector was covered by a 200 nm Al filter on a 100 nm parylene N substrate (Luxel, USA) to prohibit all visible light and IR-pump light from reaching the CCD. With an optimized HHG source and a distance from sample to CCD of 75 mm, the exposure time for one diffraction pattern of the $Gd_{28}Fe_{72}$ triple-slit was on the order of 30 s for approximately 40 000 counts in the most intense pixel. Values above this count number will lead to a non-linear photon-count response of the CCD and in extreme cases to saturation and blooming artefacts.

Optionally, a beamstop can be moved by two stepper motors orthogonal to the beam to block the direct transmission from small-angle scattering experiments. An additional 200 nm Al filter can be inserted in the XUV beam at the entrance of the chamber to remove co-propagating IR light from the XUV.

The IR pump beam is coupled into the vacuum chamber through a window and is guided to the sample by two flat mirrors. The position of the IR pump on the sample, as well as the sample position itself, is monitored by a long-distance microscope (DistaMax K2, Infinity Photo-Optical Company, USA) located outside the vacuum chamber.

The XUV scattering chamber is evacuated by two turbo pumps, which are supplemented by a backing pump. The pressure inside the vacuum chamber reached values in the order of 1×10^{-6} mbar. The volume between the CCD and the Al-filter of the CCD is connected to the volume of the chamber by two small angled channels. To prevent a higher pumping rate for the chamber volume in comparison to the small volume behind the Al-filter, a pressure regulator constrained the pumping rate.

For the M-edge experiments at the synchrotron radiation source, the spherical mirror and the IR-pump beam were not needed. The sample and the CCD were configured inside the XUV scattering chamber in a forward geometry. The vacuum of the XUV scattering chamber was coupled to the vacuum of the beamline via a pre-chamber, which was connected to the XUV scattering chamber through a differential pumping stage.

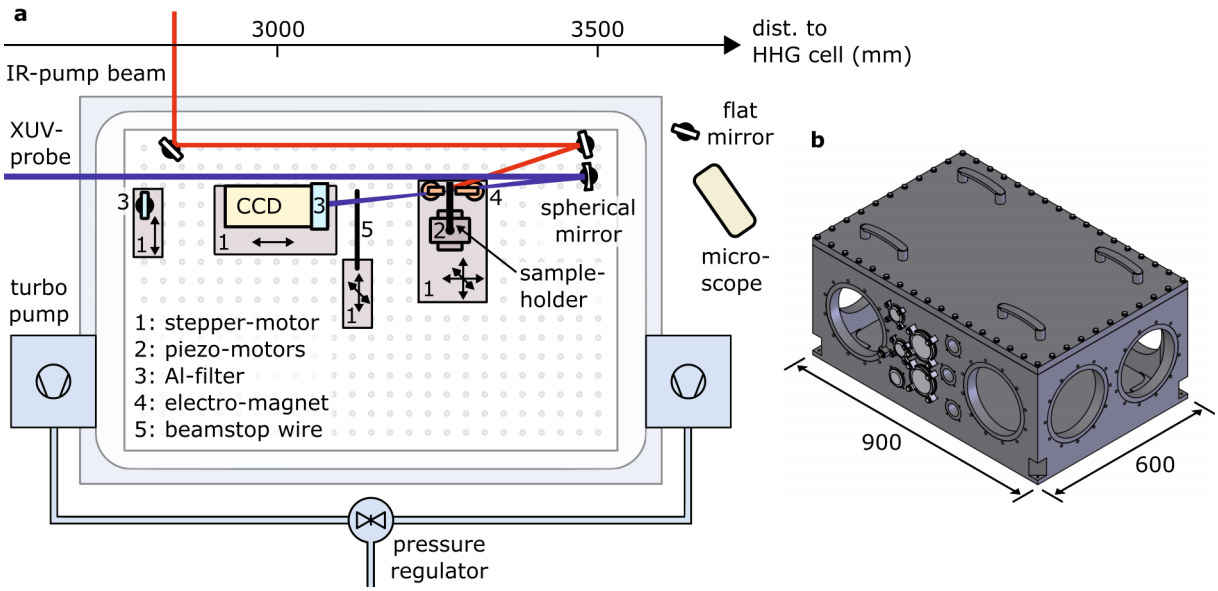

Figure 3.11: XUV scattering chamber. **a** Schematic top view of the pump-probe geometry used for the HHG triple-slit experiment. The XUV beam is refocused under nearly normal incidence onto the sample via a spherical multilayer mirror. The sample is surrounded by an electromagnet with cut-outs for the XUV-probe and IR-pump beam. The sample holder can be moved in all three axes via piezo motors. The piezo motors and the electromagnet are attached to a three-axes stepper motor to adjust the magnet gap with the sample in relation to the XUV-focus. The movement of the stepper motors are indicated by the arrow direction. For general scattering experiments, a beamstop wire can optionally block the forward scattered light. The far-field diffraction pattern is recorded by a CCD. A stepper motor moves the CCD along the beam direction to set the distance between sample and CCD. The CCD is covered by an Al-filter to block the scattered IR light. An additional Al-filter can be moved in the XUV-beam at the entrance of the chamber to remove co-propagating IR light from the XUV. The pressure of the XUV scattering chamber is lowered via two turbo-pumps, which are supplemented by a backing pump. A pressure regulator adjusts the pumping and venting rates to protect the Al-filter from damage. A long-distance microscope monitors the position of the sample as well as the size and position of the pump beam. **b** Drawing of the XUV scattering chamber. The vacuum chamber was designed to provide high flexibility for different experimental geometries at the HHG source as well as at synchrotron sources. The dimensions of the chamber are given in mm.

CHAPTER 4

Static Measurements

4.1 Introduction

In this chapter, we will first present the results of the simultaneously measured dispersive and absorptive contributions to the complex refractive index of transition metals. The XMCD contrast is used for investigating the magneto-optical changes to the refractive indices. We investigate the resonant spectroscopic response from Co and Fe at the M- and L-edges, and from Gd at the N-edge. We note that to our knowledge no simultaneous measurement of the dispersive and absorptive part of the magneto-optical constants of Gd in GdCo alloys or pure Gd at the N-edge resonance was published.

The results presented in this chapter are showing samples with out-of-plane magnetization ($Gd_{25}Co_{75}$, $Gd_{25}Fe_{75}$, and $[Co(4)Pt(7)]_{20}$). The experiments were carried out at the beamlines UE112-PGM1 (M-edges) and UE52-SGM (L-edges) at the synchrotron facility BESSY II. A sketch of the basic scattering geometry is shown in Fig. 4.1

To gain access to the complex refractive index of Co around the M-edge resonance, we used circularly polarized XUV radiation in the energy range of 45 to 75 eV. The data were recorded by a 2048×2048 pixelated CCD with 13.5 µm pixel edge size. The CCD was placed 135 mm behind the sample plane and cooled to $-40\,^{\circ}\mathrm{C}$ to reduce thermal readout noise. The sample was exposed to a 200 mT magnetic field from an electromagnet in the out-of-plane direction of the sample. The magnetic field was switched in polarity for every energy data point by inverting the current of the electro magnet from 3 to -3 A.

4.2 Magneto-optical response from $Gd_{25}Co_{75}$ and $[Co(7)Pt(6)]_{\times 12}$

4.2.1 Co M-edge Resonance

In this section, we are investigating the magneto-optical properties of Co at the M-edge. We used a $Gd_{25}Co_{75}$ alloy as sample layer for the triple-slit setup. The atomic composition

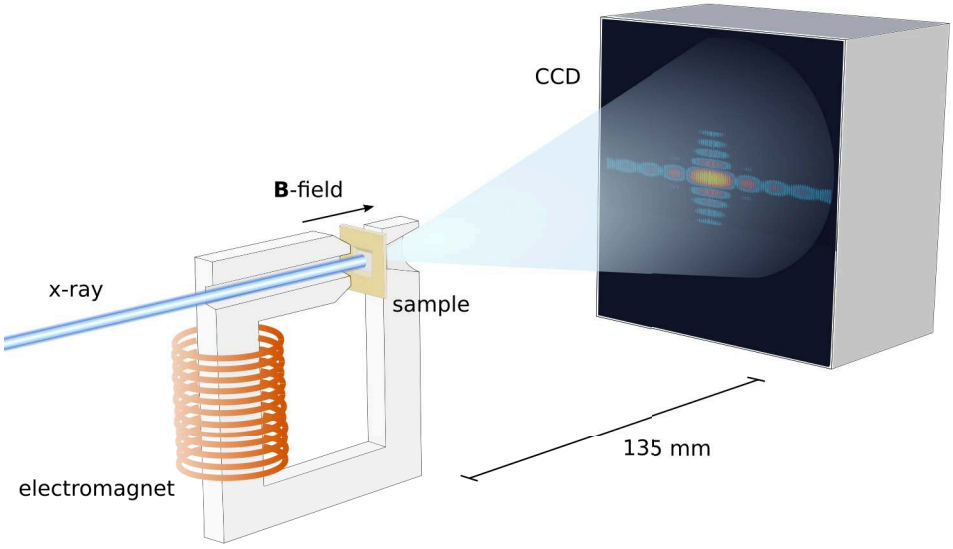

Figure 4.1: Transmission geometry of the triple-slit setup. The sample is magnetized out-of-plane. The electromagnet is able to saturate the sample magnetization in both out-of-plane directions. Circular polarized XUV radiation is used in the energy range of 45 to 75 eV. The CCD is placed 135 mm behind the sample.

used for the alloy are 25 % for Gd and 75 % Co. The $Gd_{25}Co_{75}$ layer was seeded with 3 nm and capped with 2 nm Ta. The geometry of the three slits is shown in Fig. 4.2. We will call the left vacuum slit V1 and the vacuum slit in the middle V2. The distances between the slits were chosen such that the cross-correlations in the reconstructions were not overlapping. More details about this sample are given in Ch. 3.1.1.

Figure 4.3 shows the center section of a typical dark-current corrected triple-slit diffraction pattern in logarithmic intensity scale. The exposure times varied with the different photon energies. Depending on the transmission of the sample and the photon flux of the beamline, the exposure time ranged from 300 ms to 1200 ms. Along the vertical axis in Fig. 4.3, only one spatial frequency is visible. At the vertical center axis, slight

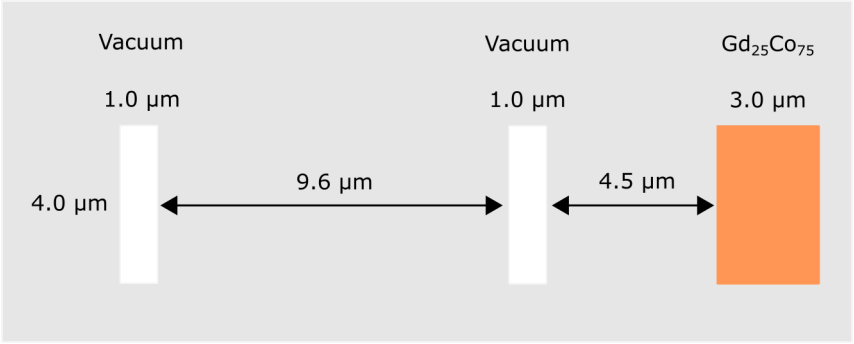

Figure 4.2: Triple-slit geometry for the $Gd_{25}Co_{75}$ sample. We will call the left vacuum slit V1 and the vacuum slit in the middle V2.

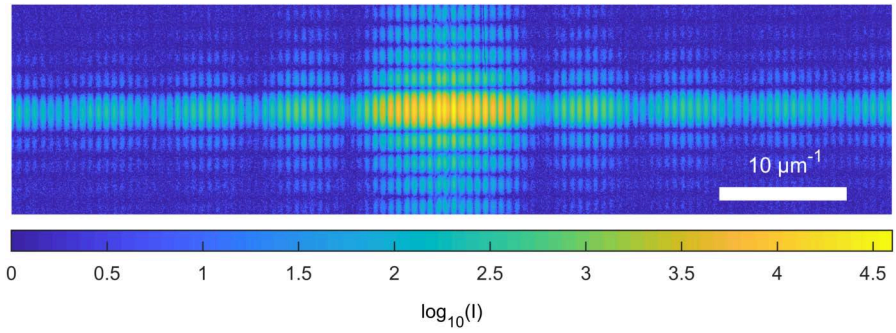

Figure 4.3: Dark-current corrected scattering pattern from the $Gd_{25}Co_{75}$ triple-slit at 75 eV in log-scale. The exposure time was 300 ms.

changes of this modulations are visible. The dominant vertical spatial frequency and the small deviations along the center are due to small deviations from the height of the slits. Along the horizontal axis, the high-frequency spatial intensity modulation originates from the largest distance in the triple-slit geometry (vaccum slit V1 to material slit, 11 µm). The low-frequency modulation is related to the width of the two vacuum slits (1 µm). Beyond the scattering along the the horizontal center axis in Fig. 4.3, the signal is dominated by shot noise. This will not have an impact on the reconstruction since only the scattering along the horizontal axis from the center is important.

To reconstruct the magneto-optical indices, first, a 2D discrete Fourier transformation is used on the diffraction pattern (upper and lower panel of Fig. 4.4). Before the transformation is applied, it is important that the diffraction pattern is centred with subpixel accuracy (see Appendix A for the complete analysis protocol). Otherwise, a phase ramp will offset the phase values from the cross-correlations[1]. Beside the autocorrelation in the center, the cross-correlation and twin images of the the cross-correlations of the three slits are visible. The phase noise in between the auto/cross-correlation areas, visible in the phase reconstruction in the upper panel in Fig. 4.4, has no physical meaning, as the amplitude in this noisy region is nearly zero. Therefore, the phase is masked out in these regions for the line scans in the center panel of Fig. 4.4.

The center panel of Fig. 4.4 shows the amplitude and phase of a horizontal line scan through the Fourier transformation of the diffraction pattern. The highest amplitude peak in the center corresponds to the autocorrelation. The phase of the autocorrelation is nearly zero. This points to the fact that the plane wave approximation is valid, as otherwise a phase ramp would be visible. The next plateau at 10 µm stems from the cross-correlation between the material slit and the adjacent vacuum slit V2. The amplitude and phase values for the transmission and phase shift through the sample are averaged over this plateau. The next peak at 20 µm corresponds to the vacuum-vacuum cross-correlation. As the two vacuum slits have both the same width, the maximum of this cross-correlation is sampled by only one pixel. The phase of the vacuum-vacuum cross-correlation is nearly zero for both twin correlations. This implies first, that the phase front incident

[1]This fact is related to a property of the Fourier transformation, which is known as time-shifting property. A shift in time corresponds to a rotation of the phase in the frequency domain: $(\mathcal{F}x)(t-t_0) = \exp(-i2\pi f t_0)X(f)$, with t denoting the time, t_0 the time shift and f being the frequency. Instead of the time/frequency pair, in our case the shift in spatial frequency is connected with a phase rotation in real space.

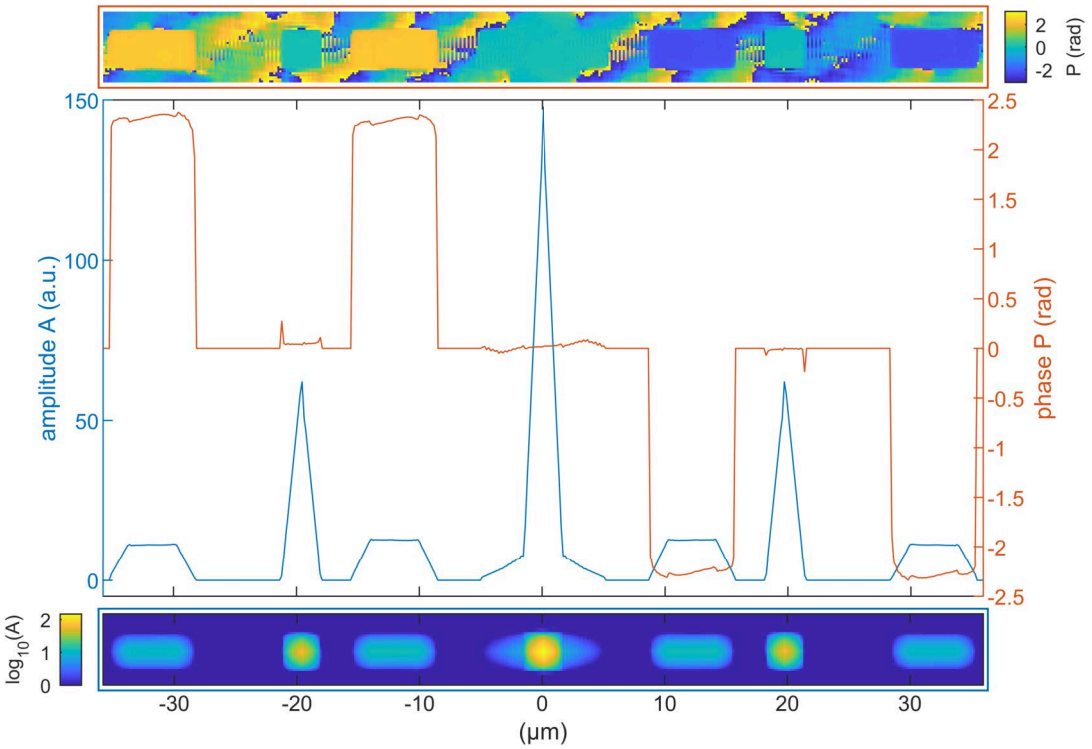

Figure 4.4: Reconstruction for $Gd_{25}Co_{75}$ triple-slit at 75 eV. Upper (lower) panel shows the phase (amplitude) of the Fourier transformation of the triple-slit diffraction pattern. The graph in the middle shows the horizontal center line scan through the amplitude and phase of the reconstruction. At 0 µm, the autocorrelation is located. Towards positive distances first, the cross-correlation of the material and vacuum slit V2 appear. This plateau is used for extracting the transmission and phase shift through the material layer. The next peak, around 20 µm, corresponds to the vacuum-vacuum cross-correlation, of which the amplitude is used for normalization. The last plateau stems from the cross-correlation of the material slit with the vacuum slit V1. The line scan of the phase is set to zero for amplitude values below 0.8 a.u. to mask out phase noise. This noise is still visible in the upper panel around the 2D phase cross-correlations.

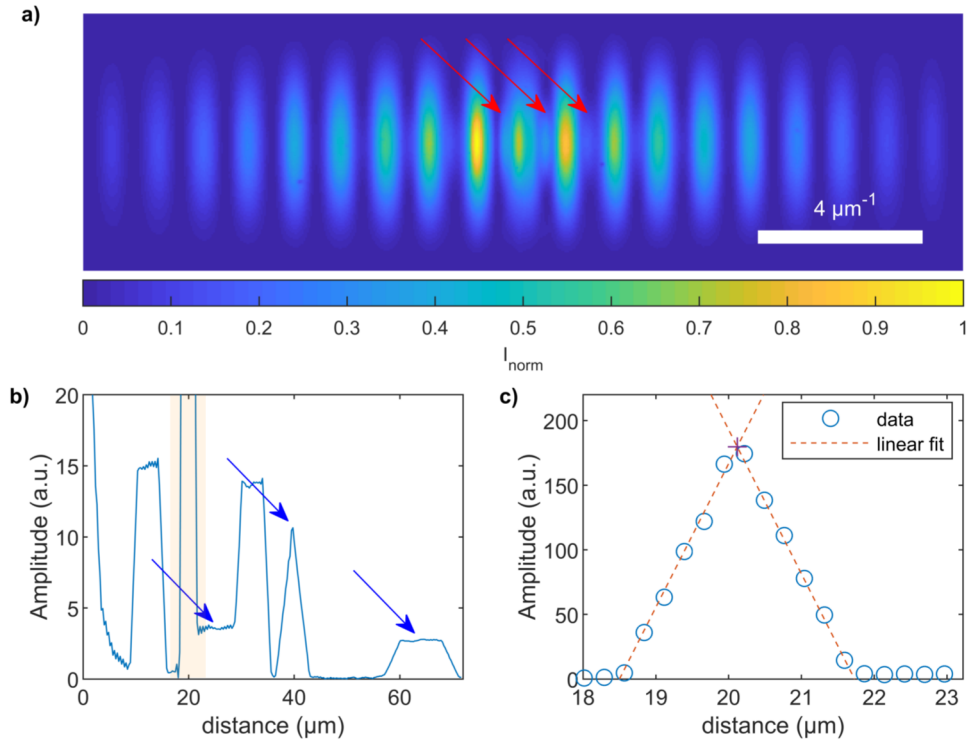

Figure 4.5: Complications of the $Gd_{25}Co_{75}$ triple-slit analysis. **a** Center part of the $Gd_{25}Co_{75}$ triple-slit diffraction for 45 eV in linear scale (normalized). Diffraction from second harmonic is visible (red arrows). **b** Amplitude of the center line scan in positive direction through the cross-correlations of the Fourier transformed diffraction pattern from **a**. The blue arrows mark the cross-correlations from the second harmonic. The second order reconstruction fits between the correlations from the fundamental order. The vacuum-vacuum cross-correlation at 20 µm is highlighted by the light orange area. **c** Magnification of the vacuum-vacuum cross-correlation for 46 eV. For this photon energy, the maximum falls between two sample points. The maximum is approximated by the intersection of two linear fits. Note that at 46 eV no significant contribution of second harmonics is visible.

on both vacuum slits had the same phase as only the relative phase between the slits is reconstructed and second, that the diffraction pattern was centred sufficiently. The amplitude of this correlation peak was used to normalize the material slit transmission to the incident photon intensity.

The plateau on the far right side in Fig. 4.4 corresponds to the material slit correlation with the vacuum slit V1. This plateau is not used for reconstruction as interference of both slits with a distance of 17 µm is already effected by the finite longitudinal incoherence. This can be seen from the comparison of the plateau height of both material cross-correlations. The amplitude of the outer correlation is lower by 12 % compared to the inner one, showing that the visibility for a distance of 17 µm is reduced.

Before we look at the reconstructed spectra, we will first mention two issues with the reconstruction. At the lower photon energies, there was a significant contribution of second

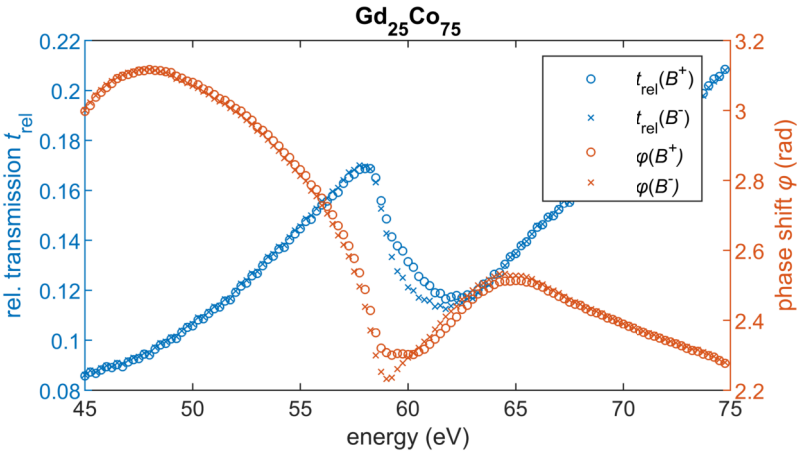

Figure 4.6: Spectroscopic response of the relative transmission t_{rel} and phase shift φ at the Co M-edge with circularly polarized light for parallel and anti-parallel out-of-plane magnetization of the Si_3N_4(150 nm)/Ta(2 nm)/$Gd_{25}Co_{75}$(30 nm)/Ta(2 nm) sample layer.

harmonics in the beam (Fig. 4.5a). This leads to the addition of three cross-correlations with twice the distance to the center and twice the size of the plateaus (Fig. 4.5b). Because of the choice of our triple-slit geometry, the reconstruction of the second harmonic material-vacuum correlation was falling in between the gap of the fundamental vacuum-vacuum correlation and the outer material-vacuum correlation (left arrow in Fig. 4.5b). Only the outer edge of the left flank overlaps with the fundamental vacuum-vacuum correlation. Considering the height of the vacuum-vacuum correlation, this adds a possible error of below 1 %. From 52 eV to higher photon energies, the contribution of the second harmonic is negligible. We note that the a possible error from the second harmonic has no impact on the calculation of the magneto-optical constants as the error is subtracted out in the difference of both magnetic field polarities. If the error of higher harmonics had an influence on the quality of our reconstruction, the error could be corrected by interpolating the fundamental triple-slit correlations by the factor two to match the sampling of the second harmonic, adjusting interpolated correlations to the height of the measured second harmonic correlations and subtracting them from the reconstruction.

Another problem with our triple-slit geometry arises when we analyse the data for different photon energies. As both vacuum slits have the same width, their correlation maximum is sampled by a single point. If the photon energy is changed, this maximum falls periodically between two sampling points, effectively lowering the amplitude of the correlation (Fig. 4.5c). To correct this periodic error in our normalization signal, we used a linear fit to the sides of the vacuum-vacuum correlation. Their intersection was used for the normalization signal which suppressed the periodic errors in the spectrum. A complete protocol of the triple-slit reconstruction can be found in Appendix A.

Figure 4.6 shows the relative transmission and the relative phase shift through the Si_3N_4(150 nm)/Ta(2 nm)/$Gd_{25}Co_{75}$(30 nm)/Ta(2 nm) sample layer for the photon energy range from 45 eV to 75 eV. The most prominent feature is the overlapping Co M_2 ($3p_{1/2}$) and M_3 ($3p_{3/2}$) absorption edges around 59 eV. In contrast to the L-edge resonance, no $3p_{1/2}$ and $3p_{3/2}$ separation is visible as the spin-orbit split core levels strongly overlap. Another visible feature is a Ta signature from post O_2 $5p_{1/2}$ absorption edge below 50 eV.

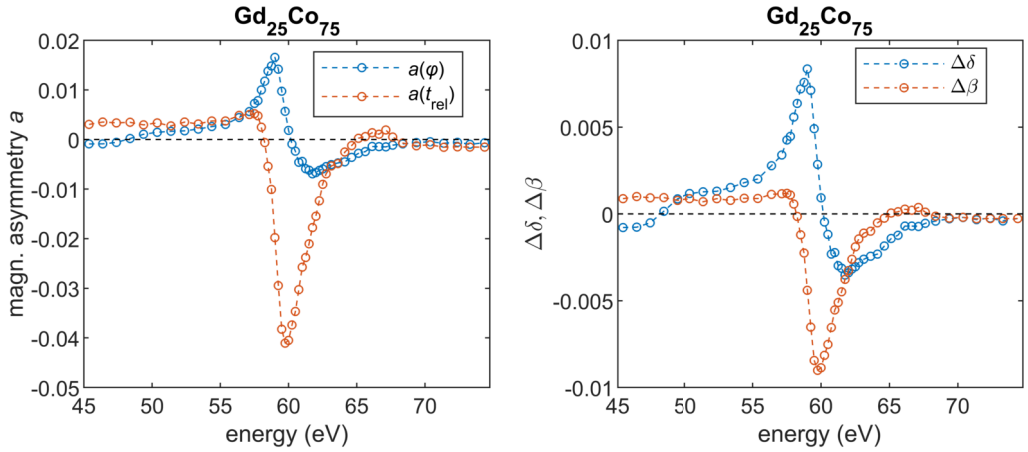

Figure 4.7: Spectroscopic response of the complex dichroic part of the optical constants from $Gd_{25}Co_{75}$ at the Co M-edge with circularly polarized light. The left panel shows the magnetic asymmetry for the relative transmission t_{rel} and phase shift φ, and the right one shows the magneto-optical constants of the Co content in the $Gd_{25}Co_{75}$ sample layer. The values of $\Delta\delta$ and $\Delta\beta$ are not corrected for the incomplete out-of-plane magnetization of the sample. For the rescaled spectra see Fig. 4.9.

For comparison, the transmission and phase shift spectrum of a pure Ta layer on Si_3N_4 for the energy range between 45 eV and 60 eV can be found in the appendix B.1. Close to the M-edge resonance at 59 eV, the spectrum for the two magnetization directions differs clearly.

The magnetic asymmetry[2] of the spectrum in Fig. 4.6 is found in the left panel of Fig. 4.7. In the off-resonant regions, where the asymmetry is nearly constant (45–57 eV and 68–75 eV), two adjacent data points were binned to one point located at the photon energy average. The maximum standard deviation for those regions is $\sigma(a(\varphi)) = 8 \cdot 10^{-5}$ for the phase asymmetry and $\sigma(t_{rel}) = 1.5 \cdot 10^{-3}$ for the asymmetry of the relative transmission.

The magneto-optical constants (right panel in Fig. 4.7) were calculated according to Eq. 2.78 and Eq. 2.79 for the Co content of the $Gd_{25}Co_{75}$ alloy. The effective thickness d_{Co} of an equivalent pure Co layer was calculated to 15 nm from the atom percentages of the $Gd_{25}Co_{75}$ sample, using the atomic mass and molar volume for Co and Gd.

The magneto-optical constants show the sum of the overlapping dichroic signals of the M_2- and M_3-edges. Further, we observe a pre-edge asymmetry in accordance to literature [3]. Below 48 eV, $\Delta\delta$ changes the sign. The maximum of the phase shift φ visible at 48 eV in Fig. 4.6 suggest, that the sign change of $\Delta\delta$ at 48 eV in Fig. 4.7 can be attributed to the Ta layer. We observe the same sign change also in the $Gd_{25}Fe_{75}$ sample (see Fig. 4.21 in Ch. 4.3.1), which also contained a Ta layer for protection against oxidation. In the post-edge region above 65 eV, $\Delta\beta$ becomes slightly positive until 68 eV. This observation also occurs for the $Gd_{25}Fe_{75}$ sample (Fig. 4.21 in Ch. 4.3.1) to an even greater extent.

To compare these results to the literature, a scaling factor must be considered. The $Gd_{25}Co_{75}$ sample layer magnetic easy-axis was in-plane (Fig. 4.8) despite the intention

[2]The magnetic asymmetry is defined as $a(S) = (S^+ - S^-)/(S^+ + S^-)$, with $S^\pm$ being the signal for positive (+) or negative (−) magnetic saturation.

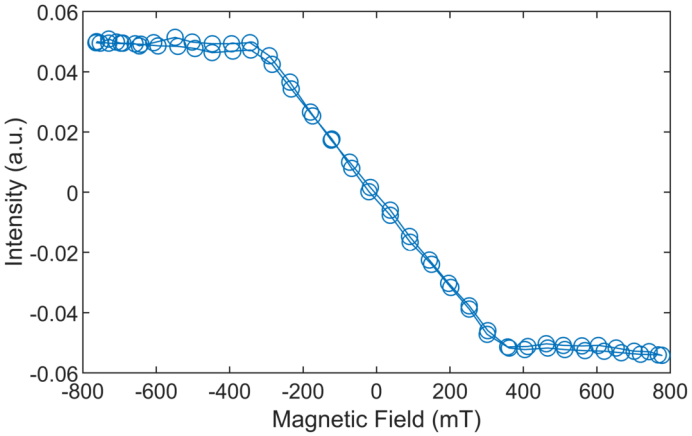

Figure 4.8: Out-of-plane hysteresis for the $Gd_{25}Co_{75}$ sample.

during the sputtering process of an out-of-plane magnetization. The applied magnetic field of 200 mT was only able to yield an out-of-plane magnetization of around $(58 \pm 2)\,\%$ from the saturation magnetization. The uncertainty of the scaling factor is due to the uncertainty of the value for the magnetic field at the exact sample position. We estimate the error of the value of the magnetic field at the sample position to be 10 mT.

Our rescaled curves of the magneto-optical indices from Co are compared to the results obtained by Willems et al. [3] in Fig. 4.9. Their work determined the absorptive and dispersive part of the magneto-optical indices by independently measuring XMCD and the Farady rotation on pure Co. In the following, we will label our results with the index Gd25Co75 and the results by Willems et al. with the index Co to indicate the chemical composition of the sample. Note that the derived magneto-optical indices refer to the Co content in the sample layer.

The density of states (DOS), locally at pure Co, is not expected to be significantly different from the DOS at a Co atom in $Gd_{25}Co_{75}$, as for a given Co atom most of their neighbours are itself Co atoms. The substitution of Co by Gd is expected to lead to a slightly different spectrum due to the different valence DOS. Further, the lower electronegativity of Gd compared to Co, is expected to slightly shift the spectrum of the absorption edge towards lower energies.

In Fig. 4.9, we observe a shift of our spectrum by 0.5 eV to the one from literature. The minimum for our $\Delta\beta_{\mathrm{Gd25Co75}}$ appears at 59.8 eV and the one from $\Delta\beta_{\mathrm{Co}}$ at 60.3 eV. As mentioned, this shift is expected due to the lower electronegativity of Gd compared to Co, but we note that a difference in the calibration of the beamline can not be excluded. Apart from that, the quantitative agreement of the spectra coincides very well. At lower energies (below 51 eV), the signal-to-noise ratio (SNR) of our $\Delta\delta_{\mathrm{Gd25Co75}}$ measurement is clearly favourable compared to the SNR from the Faraday rotation. At 48.1 eV, $\Delta\delta_{\mathrm{Gd25Co75}}$ changes sign in our measurement. This is not in accordance with the Kramers-Kronig (KK) inversion of $\Delta\beta_{\mathrm{Gd25Co75}}$ (comparison between $\Delta\delta_{\mathrm{Gd25Co75}}$ with the KK inversion of $\Delta\beta_{\mathrm{Gd25Co75}}$ is shown in the Appendix B.2). The zero crossing happens at the Ta edge (see the phase shift φ at 48 eV in Fig. 4.6). Therefore, we relate this sign change to the Ta in the sample. A further indication of the Ta contribution to the magnetic asymmetry is that the sign change of $\Delta\delta_{\mathrm{Co}}$ at 48.1 eV was neither observed nor calculated by Willems

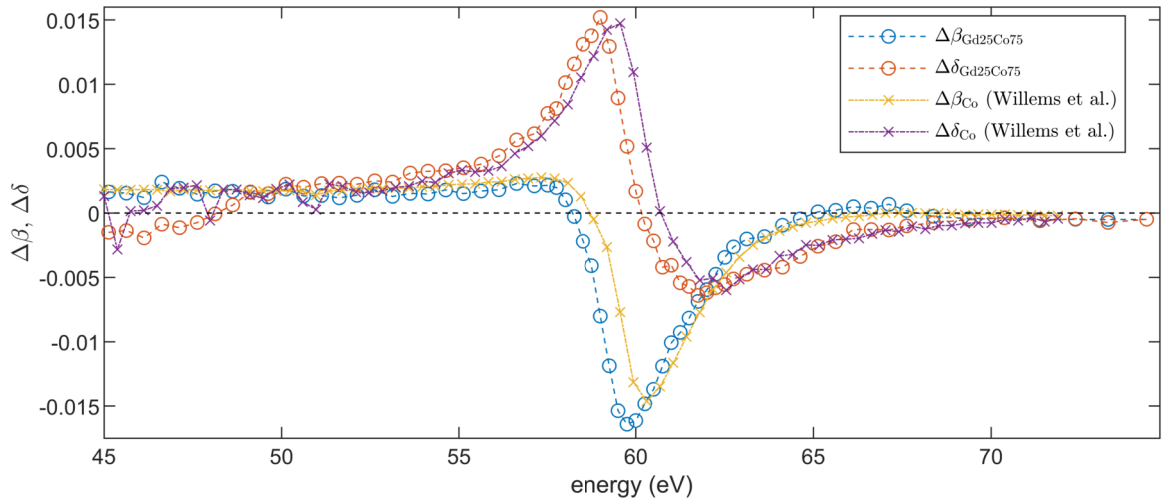

Figure 4.9: Comparison of the corrected magneto-optical constants from the Co content of the $Gd_{25}Co_{75}$ layer at the Co M-edge with data measured by Willems et al. [3] on a pure Co sample.

et al. for their sample which used Al layer instead of Ta layer [3][3].

We observe the same significant off-resonance signal as Willems et al. below the absorption edge. Due to their findings, the finite pre-edge values are stemming from Fermi level electrons excited to higher unoccupied states [3]. A difference between our data and the one from Willems et al. is found in the region from 64 eV to 68 eV, where our $\Delta\beta_{Gd25Co75}$ becomes slightly positive. The values of $\Delta\beta_{Co}$ stay below zero in this region. Due to the calculation by Willems et al. the positive maximum of $\Delta\beta$ after the M-edge resonance can be attributed to the magnitude of the exchange splitting of semicore states [3].

4.2.2 Gd N-edge Resonance

Next, we take a look at the Gd $N_{4,5}$-edge spectrum. Figure 4.10 shows the $Gd_{25}Co_{75}$ relative transmission and phase shift spectra for both parallel and anti-parallel magnetization direction from 135 eV to 165 eV. The transition minimum can be found at 148.0 eV for positive magnetization direction and at 148.8 eV for negative direction. The energy shift of the transmission for different magnetization orientations originates from the $4d^{10}\,4f^{7}[^{8}S] \rightarrow 4d^{9}\,4f^{8}[^{8}P]$ transitions and stems from a different allowed intermediate state. For parallel orientation of photon spin and sample magnetization, the $^{8}P_{5/2}$ state (148 eV) is populated, for anti-parallel orientation, the $^{8}P_{9/2}$ state (150 eV) [60]. In comparison to the 0.8 eV energy shift of the N-edge resonance maximum, the pre-edge features from 138 eV to 143.5 eV only change in amplitude when the sample's magnetization is reversed. These findings are in line with results from pure Gd samples [61, 62].

The spectrum of the normalized difference of both magnetization directions is shown in the left panel of in Fig. 4.11. The magneto-optical constants for the Gd content of the

[3]The SNR of the $\Delta\delta_{Co}$ measured by Willems et al. is too low to exclude a sign change with certainty, but the calculated data for $\Delta\delta$ at the Co M-edge shows no sign change at 48.1 eV. For the calculated spectrum and the calculation details we refer the reader to [3].

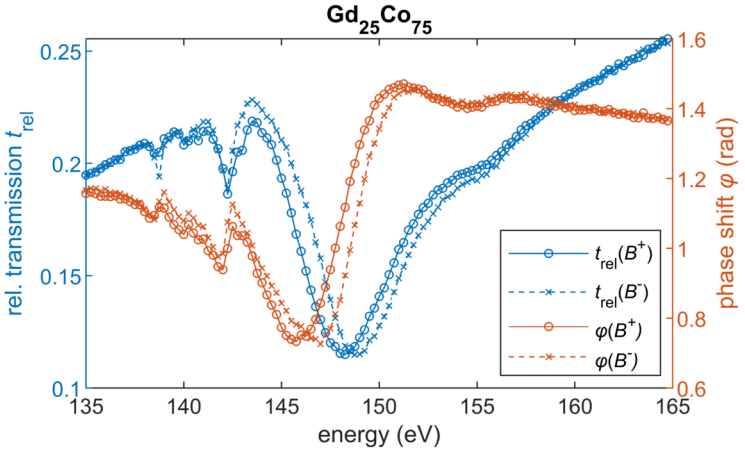

Figure 4.10: Spectrum of relative transmission t_{rel} and phase shift φ of $Si_3N_4(150\,\mathrm{nm})/Ta(2\,\mathrm{nm})/Gd_{25}Co_{75}(30\,\mathrm{nm})/Ta(2\,\mathrm{nm})$ at the Gd N-edge with circularly polarized light for parallel and anti-parallel out-of-plane magnetization.

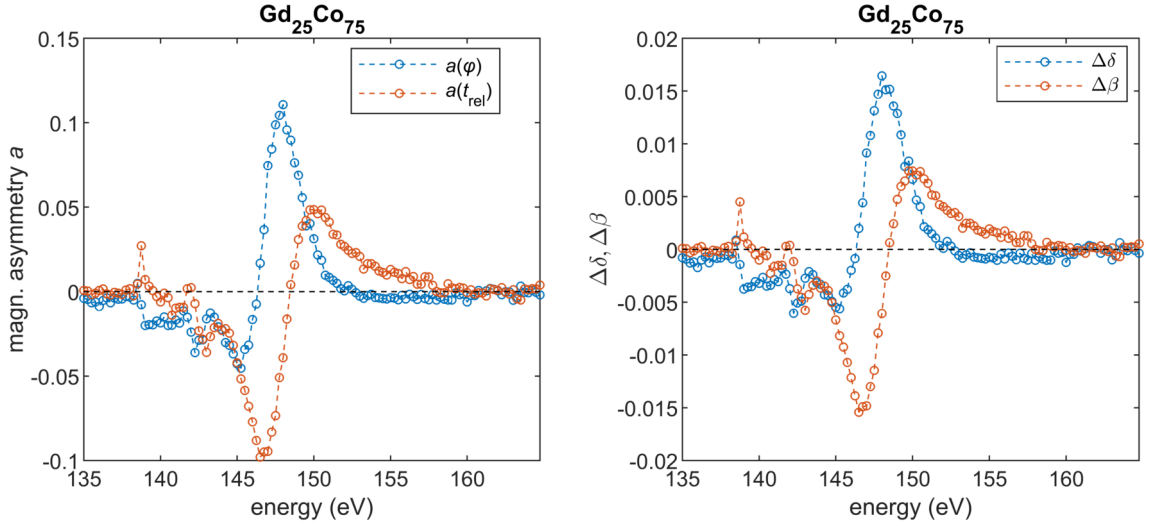

Figure 4.11: The left panel shows the magnetic asymmetry for the relative transmission t_{rel} and phase shift φ. The right panel shows the magneto-optical constants calculated for the Gd content in the $Gd_{25}Co_{75}$ sample at the $N_{4,5}$-edge.

$Gd_{25}Co_{75}$ alloy are shown on the right panel of Fig. 4.11. The absorptive part crosses zero at 148.5 eV which is comparable to the findings of Willems et al. on a $Gd_{29}Co_{71}$ alloy [63] and Prieto et al. on a pure Gd sample [61]. Beyond the N-edge resonance, the magnetic asymmetry converges to zero, and no magnetic contrast is observed.

Figure 4.12 shows the comparison of the magneto-optical indices at the Gd N-edge for the Gd content of our $Gd_{25}Co_{75}$ sample to the data measured by Prieto et al. and Willems et al. The values of $\Delta\beta_{\mathrm{Gd}}$ from Pietro et al. were calculated from absorption spectra by total electron yield on in-plane magnetized thin Gd films, while the values of $\Delta\delta_{\mathrm{Gd}}$ were derived by a Kramers-Kronig inversion of $\Delta\beta_{\mathrm{Gd}}$ [61, 62]. Prieto et al. calibrated the absorption spectrum by matching the regions of the spectrum where the influence of the resonance is expected to be negligible to tabulated absorption coefficient from Henke et al. [5]. Due to this calibration, they attribute an error of $\pm 15\,\%$ to the maximum of $\Delta\beta_{\mathrm{Gd}}$. The absorptive and the dispersive part of the magneto-optical contributions to the refractive index are both significantly larger (by a factor of 11 ± 2) compared to our results. It is also notable that the magneto-optical indices found by Prieto et al. converges significantly slower to zero after the N-edge resonance and before the pre-edge features, than our data suggests.

Willems et al. derived $\Delta\beta_{\mathrm{Gd29Fe71}}$ from absorption spectra on $Gd_{29}Co_{71}$ alloys [63]. The values of $\Delta\beta_{\mathrm{Gd25Co75}}$ from our measurement are larger by a factor of 1.9 than the values of $\Delta\beta_{\mathrm{Gd29Fe71}}$ from Willems et al. Note that Willems et al. analysed $\Delta\beta_{\mathrm{Gd29Fe71}}$ for the entire $Gd_{29}Co_{71}$ alloy instead of the Gd content [64]. If one would convert the data from the $Gd_{29}Co_{71}$ alloy to the Gd fraction, one would expect a scaling factor of 1.8. Taking this scaling factor into account, the data from Willems et al. are in good agreement with our data. The off-resonance convergence to zero is, like in our data, more pronounce in the data of Willems et al. compared to the data found by Prieto et al. The pre-edge features are not as pronounced as in our spectrum. Especially the feature of $\Delta\beta$ at 139 eV is not visible in the data by Willems et al., which could be due to the lower photon energy sampling (Fig. 4.13d shows a detailed view of the pre-edge spectrum).

Last, we compare our data to an *ab initio* TD-DFT linear response calculation[4] done for a $Gd_{50}Co_{50}$ alloy [65] with the ELK code [66] (Fig. 4.13). Additionally, Fig. 4.13 also shows the Kramers-Kronig inversion of our data for $\Delta\beta_{\mathrm{Gd25Co75}}$, the data for $\Delta\beta_{\mathrm{Gd29Fe71}}$ of Willems et al. [63], and for the fine structure of the pre-edge region (136.5 eV to 146.5 eV) the magneto-optical constants, $\Delta\delta_{\mathrm{Gd}}$ and $\Delta\beta_{\mathrm{Gd}}$, from Prieto et al. [61].

The overall shape of magneto-optical constants from the *ab initio* calculation is in reasonably good agreement with our data. In particular, the size of giant resonance is in much better agreement to our experiment than to the values from Prieto et al. (see Fig. 4.12 for the magneto-optical constants from Prieto et al. at the giant resonance) or the values for $\Delta\beta$ from Willems et al. (Fig. 4.13b). However, the calculation differs from our measured data in two aspects. In general, the calculation does not include large smearing effects coming, e.g., from temperature, finite energy resolution, or instrumental broadening. Therefore, the calculated spectrum shows more variations in its energy dependency then our measured data.

The second deviation between the calculation and our data can be found in the position and scaling of the pre-edge features. While the features of the pre-edge can be found

[4]The method of the calculation and the approximations involved are similar to the ones listed in [3].

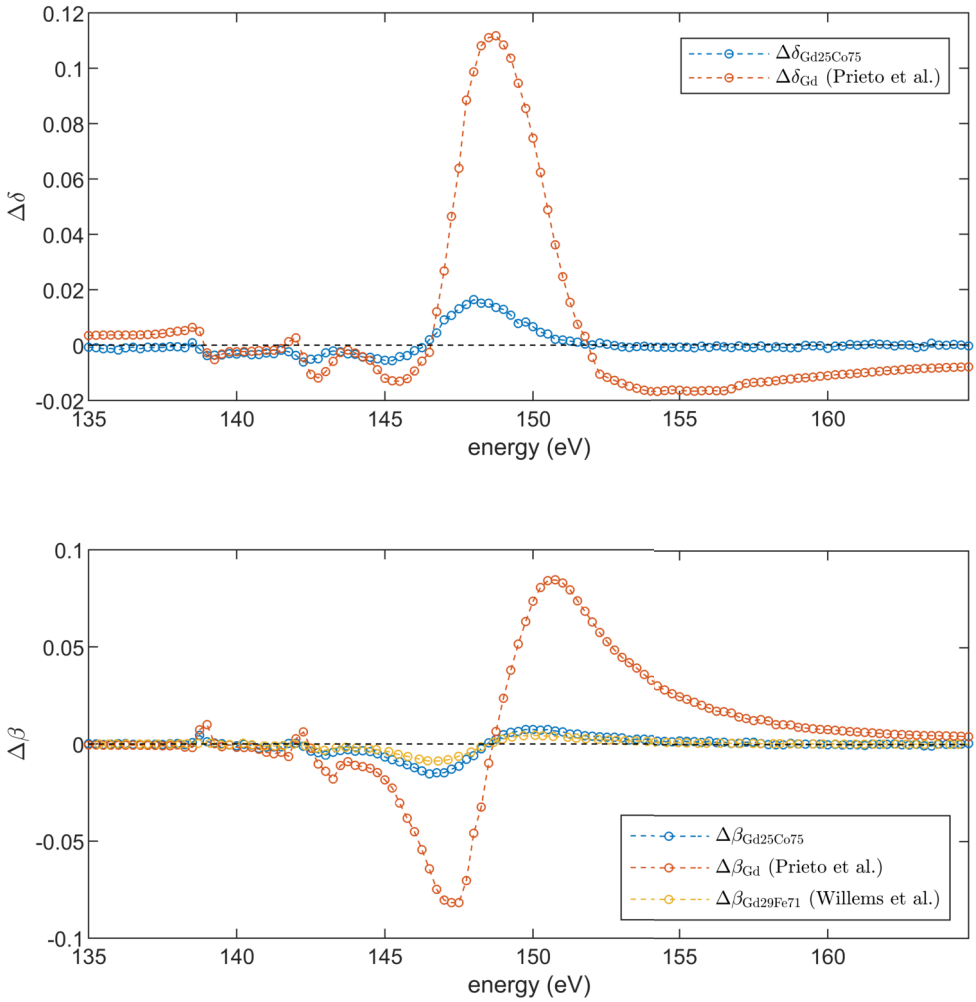

Figure 4.12: Comparison of magneto-optical indices at the Gd N-edge. The values for $\Delta\beta_{\mathrm{Gd}}$ from Prieto et al. were derived from absorption spectra on thin Gd films [61]. Similarly, Willems et al. derived $\Delta\beta_{\mathrm{Gd29Fe71}}$ from absorption spectra on $Gd_{29}Co_{71}$ alloys [63]. Note that Willems et al. analysed $\Delta\beta_{\mathrm{Gd29Fe71}}$ for the entire $Gd_{29}Co_{71}$ alloy instead of the Gd content [64]. The values of $\Delta\delta_{\mathrm{Gd}}$ were obtained by Kramers-Kronig transformation. These values are compared to our analysis of $\Delta\delta_{\mathrm{Gd25Co75}}$ (top panel) and $\Delta\beta_{\mathrm{Gd25Co75}}$ (bottom panel). The values of Willems et al. and the pre-edge features are show in Fig. 4.13 in greater detail.

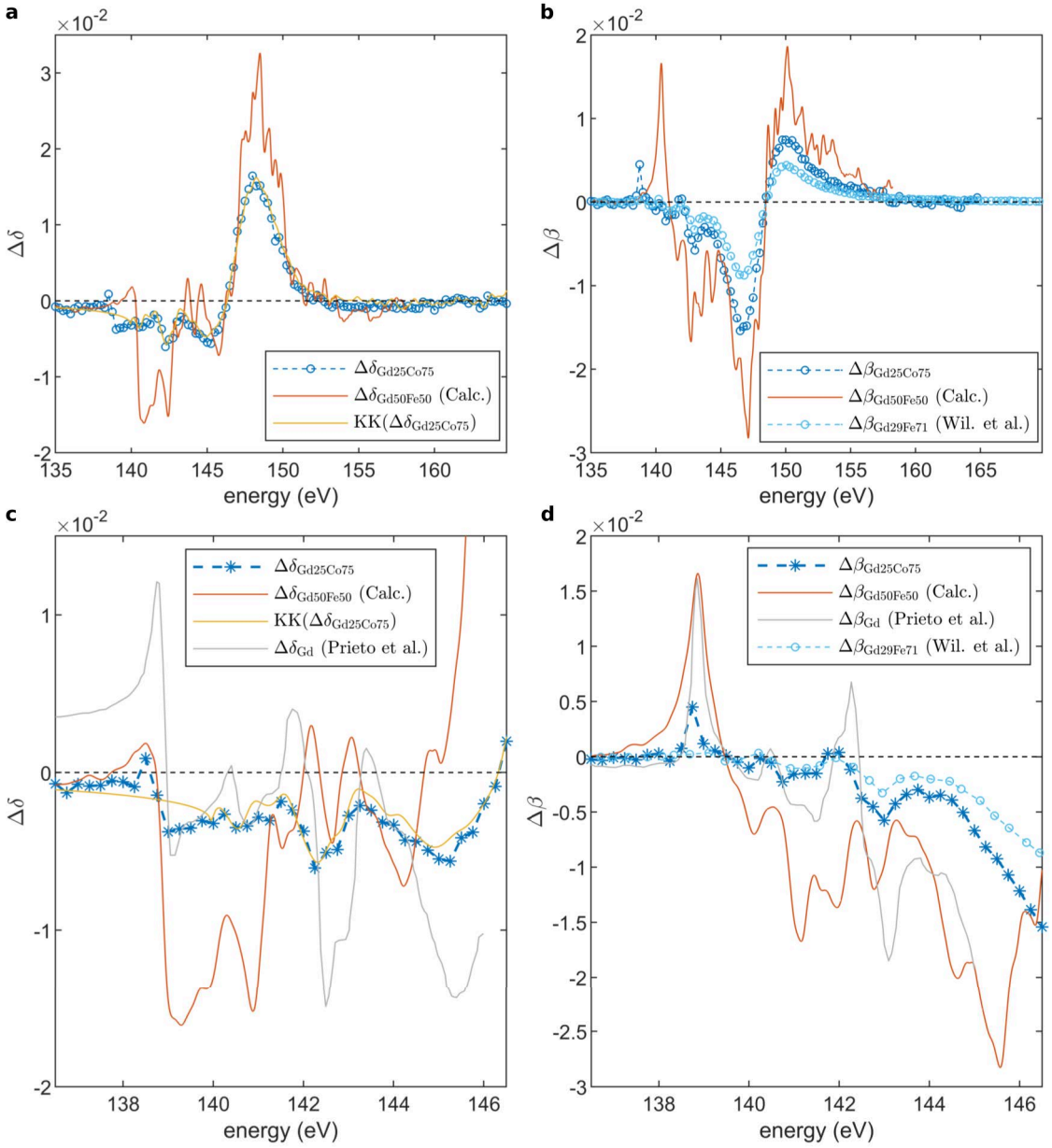

Figure 4.13: Comparison of magneto-optical indices with *ab initio* calculations (Calc.). $\Delta\delta$ and $\Delta\beta$ are shown for the pre-edge structure and the giant resonance in **a** and **b**, respectively, and are compared to the solution of the TD-DFT linear response equation for $Gd_{50}Co_{50}$. Additionally, in **a** the Kramers-Kronig inversion (KK) of $\Delta\beta_{Gd25Co75}$ and in **b** the data for $\Delta\beta_{Gd29Fe71}$ from Willems et al. [63] is shown. Note that Willems et al. analysed $\Delta\beta_{Gd29Fe71}$ for the entire $Gd_{29}Co_{71}$ alloy instead of the Gd content [64], while our magneto-optical constants are shown for the Gd content of $Gd_{25}Co_{75}$. In **c** and **d** the fine structure of the pre-edge region is magnified and compared against the data measured by Prieto et al. [61]. The values of the calculated pre-edge features are shifted by 1.55 eV to match the slope of the measured data.

between 138.3 eV and 146.2 eV for our data, the calculated spectra show the pre-edge features between 139.1 eV and 146.2 eV. For better comparability, we have shifted the calculated pre-edge fine structure by 1.55 eV in Fig. 4.13c and Fig. 4.13d to match the measured data. In the energy interval of the fine structure, the magnitude of the values from Prieto et al. seems to agree more with the theoretical calculation than our data, while the spectral position of the maxima and minima of $\Delta\delta$ and $\Delta\beta$ from Prieto et al. agree more with our data then with the calculated data.

A significant difference between the values of $\Delta\delta$ from Prieto et al. compared to our data and the calculated data can be found in the off-resonant region below 138 eV. Here, the $\Delta\delta$ from Prieto et al. shows a positive offset of about 0.4×10^{-2}, while our data and the calculated values for $\Delta\delta$ are slightly negative (-0.1×10^{-2}). The values for $\Delta\beta$, on the other hand, converge to zero below 138 eV for all data shown in Fig. 4.13d (including the one from Prieto et al.). While it is possible that the magneto-optical constants $\Delta\delta$ and $\Delta\beta$ have both a finite weight in the pre-edge regions (see Co M-edge in Fig. 4.9, Ch. 4.2.1 and [3]), it is unusual that only $\Delta\delta$ stays significantly above zero below the resonance, while $\Delta\beta$ converges to zero. Also, above the Gd N-edge resonance (> 155 eV, Fig. 4.12), the values for $\Delta\delta$ from Prieto et al. have an offset significantly different from zero. An offset for $\Delta\delta$ above and below the resonance cannot be found in our data, nor in the data from Willems et al., nor in the *ab initio* calculation (Fig. 4.13). Prieto et al. calculated the values of $\Delta\delta$ via a Kramers-Kronig inversion. The accuracy of the Kramers-Kronig inversion depends mainly on the spectral range, which is available for integration. Prieto et al. integrated the absorption spectra over an extended photon energy range of 110 eV to 200 eV. At both ends of their experimental photon energy range, the absorption difference between both magnetization direction becomes asymptotically small. Although Prieto et al. have explicitly taken care of providing suitable conditions for the integral of the Kramers-Kronig inversion, we attribute the fact that $\Delta\delta$ from Prieto et al. converges to non-zero values and does not match the other data in the off-resonant regions to artefacts of the Kramers-Kronig inversion integral.

In Fig. 4.13a and 4.13c, we show the Kramers-Kronig inversion of our $\Delta\beta$ and compared it to our measured $\Delta\delta$. While for the giant resonance and the most part of the pre-edge structure both $\Delta\delta$ and the Kramers-Kronig inversion of $\Delta\beta$ are in good agreement, below 140 eV $\Delta\delta$ shows structure which is not present in the Kramers-Kronig inversion. This deviation and the uncertainty of the off-resonant $\Delta\delta$ offset in the data of Prieto et al. emphasizing the strength of our method to exactly measure real and imaginary parts of the refractive index at the same time.

4.2.3 Co L-edge Resonance

In this section, we present our measurements of the dichroic dispersion and absorption from Co at the $L_{3,2}$ edge measured at the UE52-SGM beamline of the synchrotron-radiation facility BESSY-II. The photon energy was varied from 770 eV to 797 eV, and the photons were circularly polarized. The CCD was placed 720 mm behind the sample. The sample was moved 170 mm behind the beamline focus to increase transverse coherence and to fulfil the plane wave approximation.

We used a $[\mathrm{Co}(4)\mathrm{Pt}(7)]_{20}$ multilayer providing out-of-plane magnetization. We used a different triple-slit layout than for the M-edge measurement. Most importantly, we

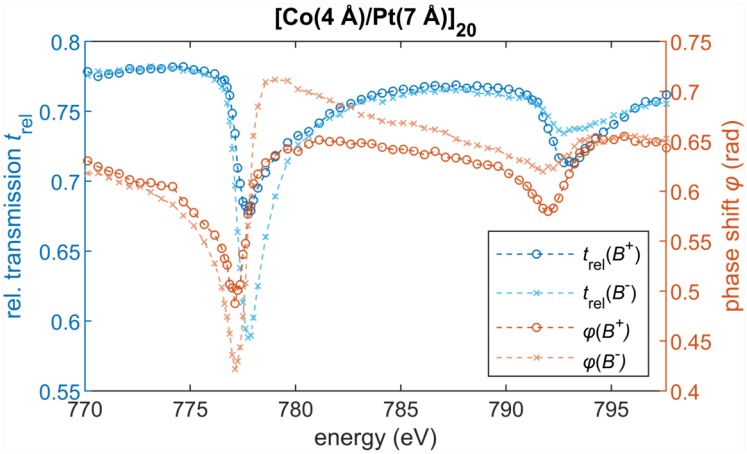

Figure 4.14: Spectroscopic response of relative transmission t_{rel} and phase shift φ of $Si_3N_4(200\,\mathrm{nm})/Ta(2\,\mathrm{nm})/[Co(4)Pt(7)]_{20}/Pt(2\,\mathrm{nm})$ at the Co L-edge with circularly polarized light for parallel and anti-parallel out-of-plane magnetization.

changed the two vacuum slits from having the same width to different widths. This ensures that there are no more sampling problems for the vacuum-vacuum cross-correlation during the spectroscopic measurements. The three slits (vacuum, vacuum, $[Co(4)Pt(7)]_{20}$) were 2 µm in height (vertical) and 0.5 µm, 0.1 µm, and 0.5 µm wide (horizontal), respectively.

There was no change in the reconstruction process, except that now there was no need to use the fitting routine shown in Fig. 4.5c. Instead, the vacuum-vacuum cross-correlation c_{23} now shows a plateau, which enables the averaging of c_{23} like it is described in the discussion to Eq. 2.57.

Figure 4.14 shows the spectroscopic response of the relative transmission and the phase shift of our $[Co(4)Pt(7)]_{20}$ multilayer in the photon energy range from 770 eV to 797 eV for both magnetization directions[5]. We found the L_3 absorption at 777.1 eV and the L_2 absorption at around 792 eV. In contrast to the data from the x-ray data booklet [67], our data appears shifted by approximately 1.0 eV towards lower energies. Compared to the spectrum from the Co M-edge, we observe two clearly separated absorption peaks due to the large spin-orbit splitting of the Co $2p$ levels.

In Fig. 4.15 (left), the normalized difference of both magnetization directions is shown. The derived magneto-optical constants for the Co content are shown on the right side of Fig. 4.15. The sign change of $\Delta\beta$ is a direct result of the sign change of the spin-orbit coupling for both fine structure resonances. Between both edges, $\Delta\delta$ does not fall to zero and stays between 0.4×10^{-3} and 0.25×10^{-3}. The Kramers-Kronig inversion of $\Delta\delta$ is compared in Fig. 4.15 (right) with our measured $\Delta\beta$. Both graphs align very well, except for the region below 776 eV. The very good agreement elsewhere suggests that also the non-zero values in between the absorption edges are reliable.

In Fig. 4.16, we compare our results for the magento-optical index of Co at the Co L-edge to data from literature. Mertins et al. obtained the values of $\Delta\delta$ and $\Delta\beta$ by analysing magneto-optical Kerr rotation and ellipticity spectra of Co samples. Kortright et al. published the complex first-order scattering factor f_{m1}. They measured the imaginary part f_{m1} by magnetic circular dichroism absorption spectroscopy and provided the real

[5]We note that the data for M-edge of this sample system can be found in the appendix B.3.

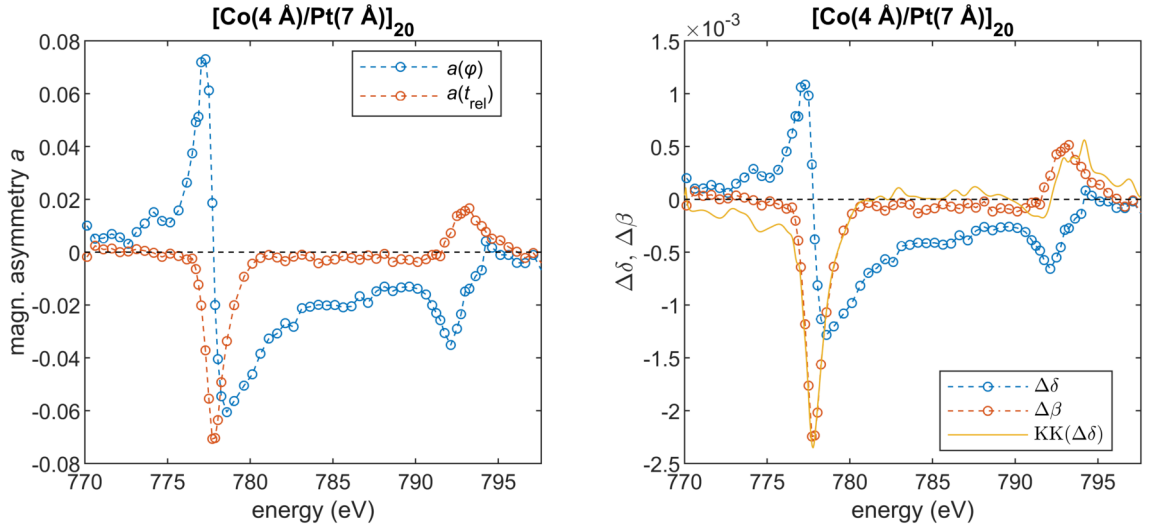

Figure 4.15: Spectroscopic response of the complex dichroic part of the optical constants at the Co L-edge with circularly polarized light. The left graph shows the magnetic asymmetry, and the right one shows the magneto-optical constants of the Co content from the $[\mathrm{Co}(4)\mathrm{Pt}(7)]_{20}$ multilayer. The values of $\Delta\beta$ is compared with the Kramers-Kronig inversion of $\Delta\delta$.

part of f_{m1} via a Kramers-Kronig transformation. On the basis of the complex first-order scattering factor f_{m1} from Kortright et al., we calculated the complex magneto-optical index (shown in yellow in Fig. 4.16) by [25]

$$\Delta\delta - i\Delta\beta = -\frac{n_{\mathrm{a}} r_{\mathrm{e}} \lambda^2}{2\pi}(\mathrm{Re}\, f_{\mathrm{m1}} + \mathrm{Im}\, f_{\mathrm{m1}}), \tag{4.1}$$

with n_{a} being the Co number density and r_{e} the classical electron radius.

The spectra of $\Delta\delta$ and $\Delta\beta$ measured by our triple-slit method appear shifted by 0.2 eV to lower energies compared to the spectra from Mertins et al. and by 0.3 eV to lower energies compared to the spectra from Kortright et al. We attribute this shift to calibration errors of the beamlines, as the both measurements on Co/Pt multilayer are shifted in a different direction compared to the Co measurement. We find that the derived magneto-optical indices from the scattering factor of Kortright et al. are too large by the factor 2 compared to our data and the data from Mertins et al. Scaled by a factor of 0.5 the derived magento-optical indices from Kortright et al. are in very good agreement with the data from Mertins et al. while both of them are in good agreement to our data. However, it is noticeable that the magnitude of our data at the L_3-edge is by about 23 % larger and at the L_2 edge by about 19 % smaller compared to the data of Mertins et al.

For the analysis of our triple-slit data, we use the effective thickness d_{eff} of Co in the $[\mathrm{Co}(4)\mathrm{Pt}(7)]_{20}$ multilayer as given parameter. If the effective thickness of Co $d_{\mathrm{eff}} = 8$ nm has an error of $\Delta d = 0.4$ nm the resulting $\Delta\beta$ and $\Delta\delta$ have an error of 5 %. The effect of the different magnitudes of $\Delta\beta$ at the L_3 and L_2 edge is larger than our estimated error and is known in the literature as an enhancement of the orbital moment in Co/Pt multilayers via interfacial hybridization [30, 70].

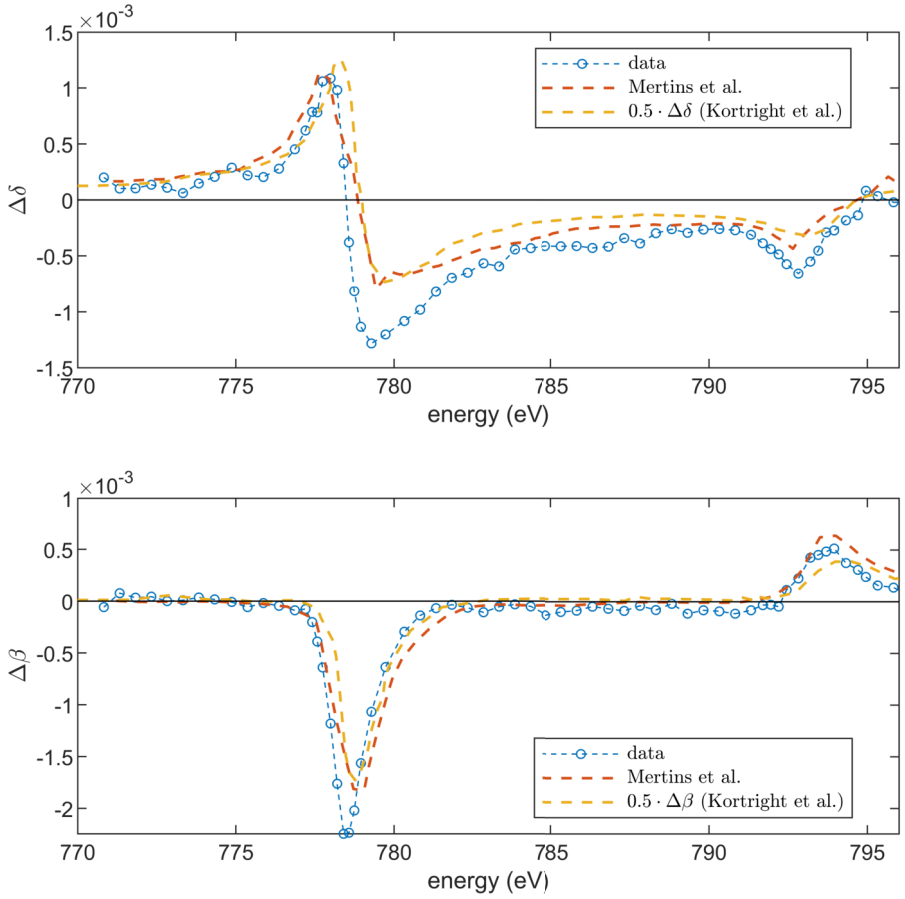

Figure 4.16: Comparison of the magneto-optical indices $\Delta\delta$ and $\Delta\beta$ from Co at the Co L-edge. Our data (blue circles) was measured on a $[\mathrm{Co}(4)\mathrm{Pt}(7)]_{20}$ multilayer. The values from Mertins et al. were obtained by longitudinal magneto-optical Kerr rotation and ellipticity spectrometry on a Co sample capped with Al [68]. Kortright et al. published the first-order magnetic scattering factors f_{m1}. They obtained the imaginary part of f_{m1} by transmission absorption measurements with circularly polarized light on a $\mathrm{Pt}(20\,\mathrm{nm})/[\mathrm{Co}(6)\mathrm{Pt}(4)]_{50}/\mathrm{Pt}(3\,\mathrm{nm})$ multilayer, while the real part of f_{m1} was calculated via the Kramers-Kronig transformation [69]. The magneto-optical index shown as yellow curve was derived by us on the basis of the scattering factors by Kortright et al. through the relationship between scattering factor and the refractive index. We scaled the derived values from Kortright et al. by a factor of 0.5 for easier comparison with the other spectra.

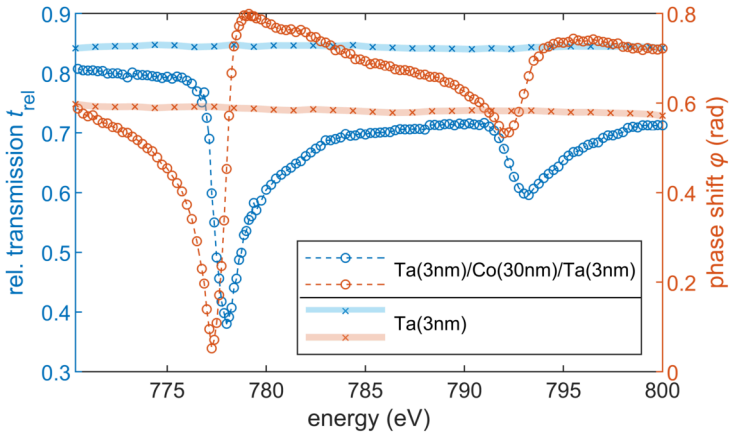

Figure 4.17: Spectroscopic response of relative transmission t_{rel} and phase shift φ at the Co L-edge with linear polarized light for [Ta(3 nm)/Co(30 nm)/Ta(3 nm)]. The relative transmission and phase shift of a sample layer with 3 nm Ta is shown in less saturated colors. In both samples a 200 nm thick Si_3N_4 layer was present.

In a next step, we aim to reconstruct the non-dichroic optical constants of Co at the L-edge. For this, we used horizontally polarized synchrotron radiation. We changed the sample system to a pure Co layer with 30 nm thickness with a 3 nm thick Ta layer above and below. To correct the influence of the Ta layer and Si_3N_4 layer on the Co spectra, we measured the relative transmission and phase shift of a Si_3N_4(200 nm)/Ta(3 nm) sample as reference. The spectral response of the relative transmission and the phase shift through both samples are shown in Fig. 4.17. While we observe the well known Co L_3 and L_2 absorption for the Co layer, the Ta sample shows a nearly constant spectroscopic dependency for the observed energy range.

Compared to the relative transmission and phase shift of the $[Co(4)Pt(7)]_{20}$ multilayer, the following differences between the Co layer and the $[Co(4)Pt(7)]_{20}$ multilayer can be observed[6] (Fig. 4.18):

- The relative transmission of the Co sample exhibits a less pronounced transmission recovery in the L_3/L_2 interpeak region than the $[Co(4)Pt(7)]_{20}$ multilayer.
- The maximum after the zero crossing at L_3 (779 eV) of the relative phase shift is more defined for the Co sample.
- The spectrum of the Co sample appears shifted to higher energies by 0.2 eV.

These results are in accordance with literature [71] and can be explained by the hybridization of the Co 3d and Pt 5d bands at the interfaces (see [63] for a discussion at the Co M-edge). The hybridization shifts the distribution of the free states above the Fermi level closer to the Fermi level. For the same reason there are consequently less free states for Co/Pt 3d-states further away from the Fermi level and therefore a lower 2p–3d transition

[6]Note that the influence of the additional Ta layers in the Co sample and the Si_3N_4 layer in both the Co sample and the $[Co(4)Pt(7)]_{20}$ multilayer is negligible for the following comparison. In Fig. 4.18, we subtracted the linear trend visible before the L_3 resonance from the spectra.

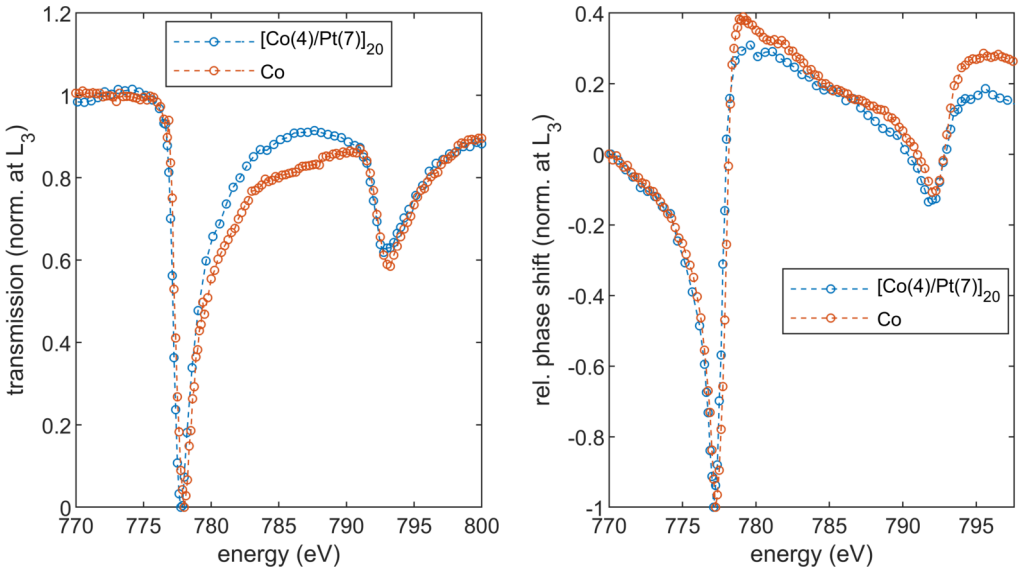

Figure 4.18: Normalized transmission spectra and relative phase shift spectra around the Co L_3-edge for the Co sample and the $[Co(4)Pt(7)]_{20}$ multilayer. The spectra are linear offset corrected and are normalized to the amplitude between the values before the L_3 resonance and the L_3 peak. The spectrum of $[Co(4)Pt(7)]_{20}$ was averaged between the spectra of parallel and anti-parallel out-of-plane magnetization from Fig. 4.14.

probability for energies between the L_3 and L_2 resonance, which explains the differences between Co/Pt and Co in this spectral region.

Between the relative phase shift of the Co layer and the Co/Pt multilayer, another difference after the L_2 resonance above 793.5 eV can be found. Here, the value of the relative phase shift for the Co layer stabilizes at more positive values than the relative phase shift from the Co/Pt multilayer. We attribute this difference after the resonance to the influence of the substrate of the samples.

In order to determine the optical constants from Co at the L-edge resonances, we used the reference data of the Ta sample and subtracted the contributions of the Si_3N_4 and Ta layers from data of the Co sample. The optical constants were calculated by:

$$\beta_{\mathrm{Co}} = -(\ln|c^{\mathrm{n}}_{12,\mathrm{Co}}| - \ln|c^{\mathrm{n}}_{12,\mathrm{Ta}}| + \phi_\beta)/(2kd_{\mathrm{Co}}) \tag{4.2}$$

and

$$\delta_{\mathrm{Co}} = (\arg c^{\mathrm{n}}_{12,\mathrm{Co}} - \arg c^{\mathrm{n}}_{12,\mathrm{Ta}} + \phi_\delta)/(2kd_{\mathrm{Co}}) \tag{4.3}$$

with the correction terms:

$$\phi_\beta = k\beta_{\mathrm{Ta}}d_{\mathrm{Ta}} \tag{4.4}$$

and

$$\phi_\delta = k\delta_{\mathrm{Ta}}d_{\mathrm{Ta}}. \tag{4.5}$$

The correction terms are needed because the Co sample contained 6 nm of Ta and the Ta reference sample was only a 3 nm thick layer. The optical constants for the Ta correction

term were taken from CXRO [48]. This correction is valid because there are no Ta resonances around the Co L-edge, making the CXRO values of Ta a good approximation in this photon energy interval.

The uncertainty in the Ta layer thickness adds an error to the values of δ and β. However, our data analysis is not strongly affected by the error in the Ta layer thickness. For example, even if the difference in Ta film thickness was twice as large as the 3 nm specified in the sample fabrication process, the error in β and δ would be only $\epsilon_\beta = -1.2 \cdot 10^{-4}$ and $\epsilon_\delta = 2.7 \cdot 10^{-4}$ for the measured spectral region.

We show the resulting optical constants δ and β in Fig. 4.19 and compare them to the values from literature[7]. The complex refractive index of Co from Mertins et al. was determined via Faraday measurements and Bragg scattering [68]. Kortright et al. obtained the imaginary part of the charge scattering factor f_c by transmission absorption measurements using circular polarization on a Pt(20 nm)/[Co(6)Pt(4)]$_{50}$/Pt(3 nm) multilayer and calculated the real part of f_c by Kramers-Kronig transformation. On the basis of the complex charge scattering factor f_c from Kortright et al., we calculated the refractive index (shown in yellow in Fig. 4.19) according to Eq. 4.1. In Fig. 4.19, we also include values from CXRO [48]. We note that the model used for the calculation of the values from CXRO is not correct at resonances, as it approximates the response by the superposition of the the pure atomic responses, not taking the fine structure in the vicinity of the absorption edges into account. Nevertheless, we can use those values to verify if our measured data is converging to the CXRO data in the off-resonance energy regions.

The values of β from Mertins et al. agree very well with our data. However the values of δ from Mertins et al. seem to have a constant negative offset. This can be seen from the fact that below the L_3 resonance, the values of δ of Mertins et al. are significantly lower (offset approximately 1×10^{-3}) than those of CXRO and our data.

Our spectrum of β agrees very well with that of Kortright et al., while small deviations of δ are visible below and at the L_3 resonance and at the L_2 resonance. We attribute the small deviations of the δ between our values and the values from Kortright et al. to the fact that Kortright et al. used a Kramers-Kronig transformation to obtain δ which can cause artefacts. This can be seen, e.g., in the range below 772 eV, where our δ values approach the CXRO curve, but the Kortright et al. values have a slight negative offset. This again demonstrates the value of our method to be self-normalizing and to determine the real and imaginary part of the refractive index simultaneously.

4.3 Magneto-optical response from $Gd_{25}Fe_{75}$

In this subsection, we are analysing the Fe M- and L edge, and the Gd N-edge on a $Gd_{25}Fe_{75}$ sample layer. The sample was measured during the same beamtime as the $Gd_{25}Co_{75}$ alloy. The reconstruction process and discussion follows the same steps as described in the section Ch. 4.2.1.

[7] For better comparability, we have aligned the spectra to the edge of the CXRO data. Our data were shifted by 0.7 eV, the spectrum from Mertins et al. by −2.3 eV, and the spectrum from Kortright et al. by −0.4 eV

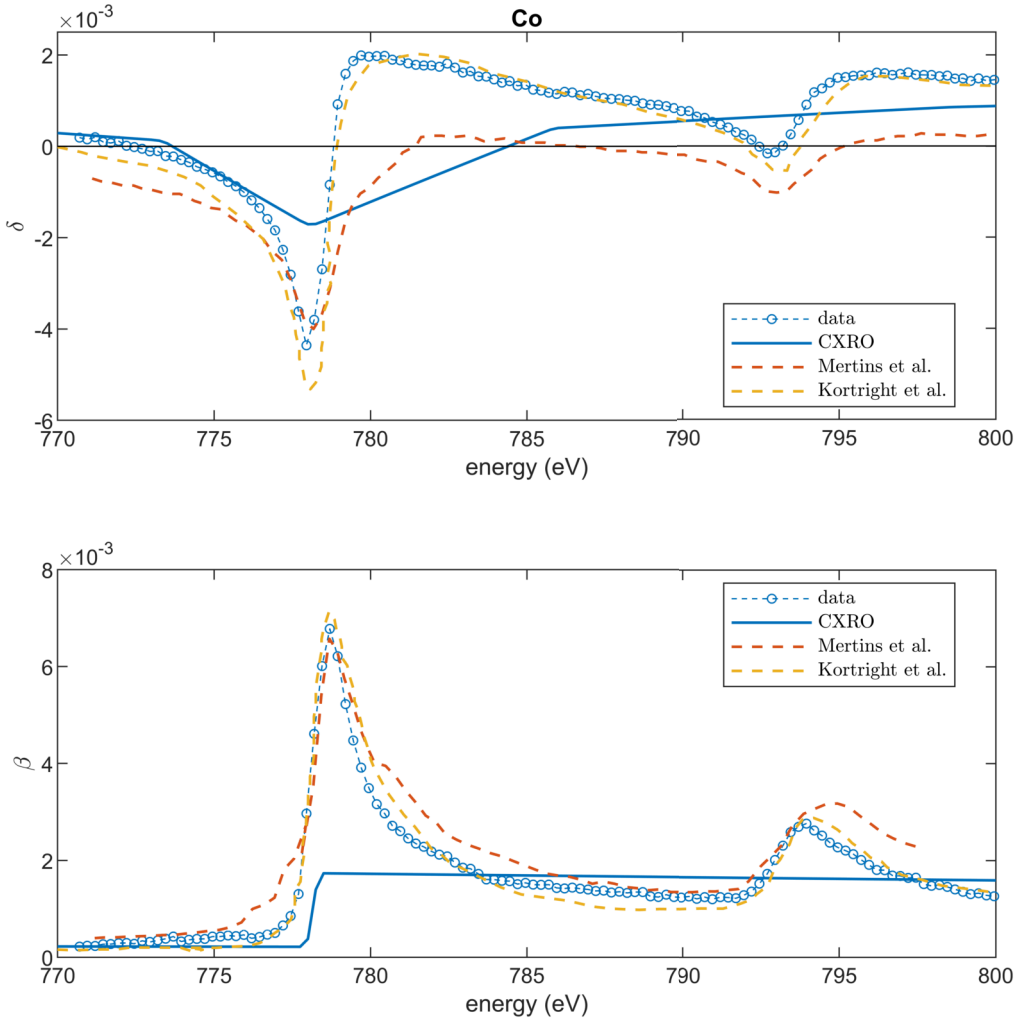

Figure 4.19: Optical constants from Co at the L-edge resonances compared to values from literature. Mertins et al. determined the complex refractive index of Co via Faraday measurements and Bragg scattering [68]. Kortright et al. obtained the imaginary part of the charge scattering factor f_c by transmission absorption measurements using circular polarization on a Pt(20 nm)/[Co(6)Pt(4)]$_{50}$/Pt(3 nm) multilayer and calculated the real part of f_c by Kramers-Kronig transformation. The refractive index shown as yellow curve was derived by us on the basis of the charge scattering factors by Kortright et al. The values of CXRO [48] approximates the response by the superposition of the the pure atomic responses and are shown to verify off-resonant convergence off the data. The spectra are shifted to align with the edge of CXRO for better comparability. The individual shifts are given in the text.

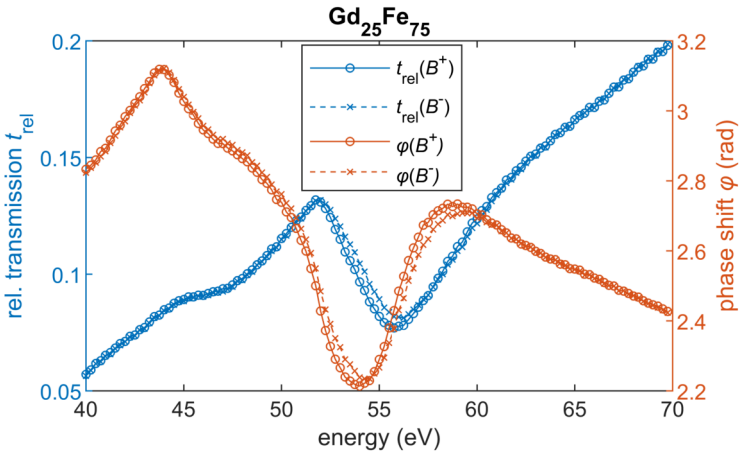

Figure 4.20: Spectroscopic response of relative transmission t_{rel} and phase shift φ of the Si_3N_4(150 nm)/Ta(2 nm)/$Gd_{25}Fe_{75}$(30 nm)/Ta(2 nm) sample layer at the Fe M-edge with circularly polarized light for both magnetic out-of-plane saturation directions.

4.3.1 Fe M-edge Resonance

In Fig. 4.20, we show the spectrum of the relative transmission and phase shift in the energy range from 40 eV to 70 eV for the $Gd_{25}Fe_{75}$ sample for both magnetic saturation fields. The Fe M-edge begins at about 52 eV. Compared to the values from [67], this is shifted by 0.7 eV to lower energies. The spectral shift is comparable to the one between the measured spectrum of $Gd_{25}Co_{75}$ and pure Co. The same argumentation for the origin of the spectral shift as for $Gd_{25}Co_{75}$ applies to $Gd_{25}Fe_{75}$, too (see Ch. 4.2.1). The lower electronegativity of Gd compared to Fe is expected to cause a shift of the $Gd_{25}Fe_{75}$ spectrum toward lower energies compared to the spectrum for pure Fe. Nevertheless, we cannot exclude a small energy offset due to a miscalibrated beamline.

Beside the M-edge resonance, the Ta signature below 47 eV is visible. The slope of the whole spectrum can be explained by the Ta present in the sample. The relative transmission and phase shift of a Ta layer is given in the appendix B.1.

In Fig. 4.21 (right panel), we show the normalized difference of the spectrum for both saturation fields. In Fig. 4.21 (left panel), the magneto-optical constants are calculated.

In the off-resonant regions, where the asymmetry is nearly constant (40–51 eV and 61–70 eV), two adjacent data points were binned to one point located at the photon energy average. The maximum standard deviation for those regions is $\sigma(a(\varphi)) = 3 \cdot 10^{-5}$ for the phase asymmetry and $\sigma(t_{\mathrm{rel}}) = 6.5 \cdot 10^{-4}$ for the asymmetry of the relative transmission. The overall shape of the magneto-optical constants for Fe are similar to the one of Co (see Fig. 4.7, left panel).

As for the Co data, we have a sizeable magnetic asymmetry in the pre-edge region. For the dispersive part $\Delta\delta$ of the Co and Fe data, the asymmetry changes sign at around 44 eV. In Ch. 4.2.1, we explained this sign change with the presence of Ta in the sample. This explanation applies to the measurement with the $Gd_{25}Fe_{75}$ sample as well. In the post-edge region at 57.6 eV, $\Delta\beta$ overshoots to positive values and falls to zero at 63.4 eV. This overshoot is stronger than in the Co data. The maximum of $\Delta\beta$ can be found at 54.6 eV.

In Fig. 4.22, we compare the magneto-optical constants from our triple-slit measurement

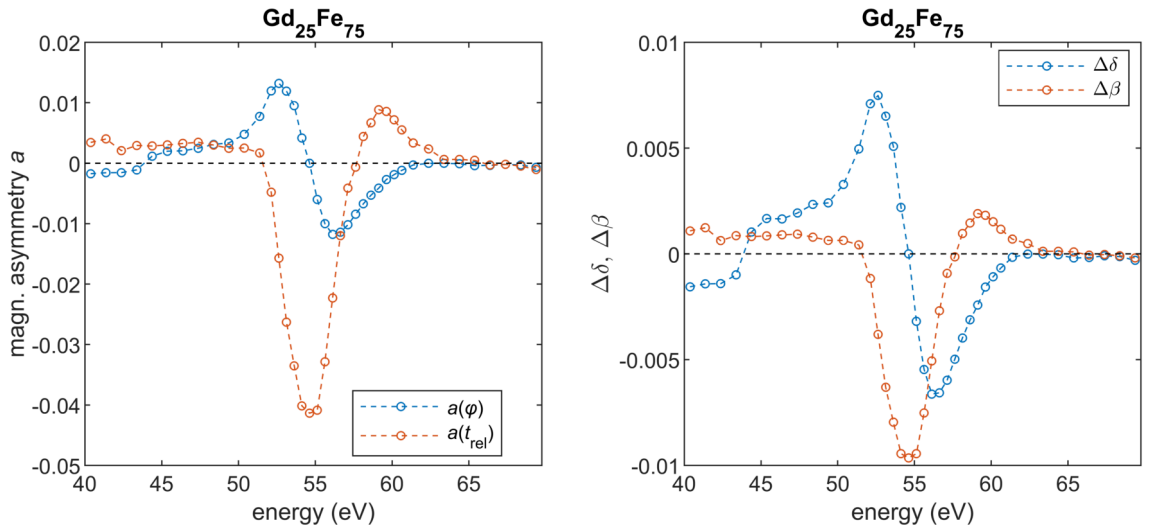

Figure 4.21: Spectroscopic response of the complex dichroic part of the optical constants for the Fe content of the $Gd_{25}Fe_{75}$ alloy at the Fe M-edge with circularly polarized light. Magnetic asymmetry a is shown on the left side, the magneto-optical constants are shown on the right side.

to the ones published by Willems et al. [3]. Their work determined the absorptive and dispersive part of the magneto-optical indices by independently measuring XMCD and the Farady rotation on pure Fe. Even though the data is in qualitative good agreement, the pre-edge and on-resonance values of our $\Delta\delta$ and $\Delta\beta$ are only 70 % in size compared to the values from Willems et al. For the $Gd_{25}Co_{75}$ alloy, the deviation from the literature values could be explained by the in-plane magnetization of the sample and corrected by an appropriate scaling factor. In the case of our $Gd_{25}Fe_{75}$ data, the sample magnetic easy axis was out-of-plane and saturated (hysteresis is shown in Fig. 3.4). It is possible that an error during the sample fabrication process caused an error in the $Gd_{25}Fe_{75}$ layer thickness or the $Gd_{25}Fe_{75}$ composition. Both uncertainties would manifest themselves as scaling errors in the reconstruction of the magneto-optical indices, as the layer thickness of the magnetic material is included in the calculation as a linear scaling factor. For example, if the exact effective layer thickness of Fe would be 12.5 nm instead of 15.5 nm (corresponding to 67 atomic % of the alloy instead of 75 atomic %), both the data of Willems et al. and our data would match within the measurement error.

To investigate the parameters of the sample layer, we analysed slices of the sample with transmission electron microscopy (TEM) and the sample composition with energy dispersive x-ray analysis (EDX). The TEM analysis showed that the $Gd_{25}Fe_{75}$ layer thickness was 27.5–32.0 nm $\pm$ 1.00 nm (Fig. 4.23), i.e., within the measuring error the $Gd_{25}Fe_{75}$ layer thickness was as intended. Due to the low SNR of the EDX analysis, we cannot clearly deduce the correct fraction of the Fe content. Within the measuring error of the EDX analysis, it is possible that our sample Fe content was too low. An overestimation of the layer thickness would explain the underestimation of the magneto-optical indices. We note that usually the error in stoichiometry is below 1 % due to the precise deposition rate (0.2 Å s^{-1}) in the magnetron sputtering process. Taking into account the results of the TEM and EDX analysis, we are convinced that the values we determined for the

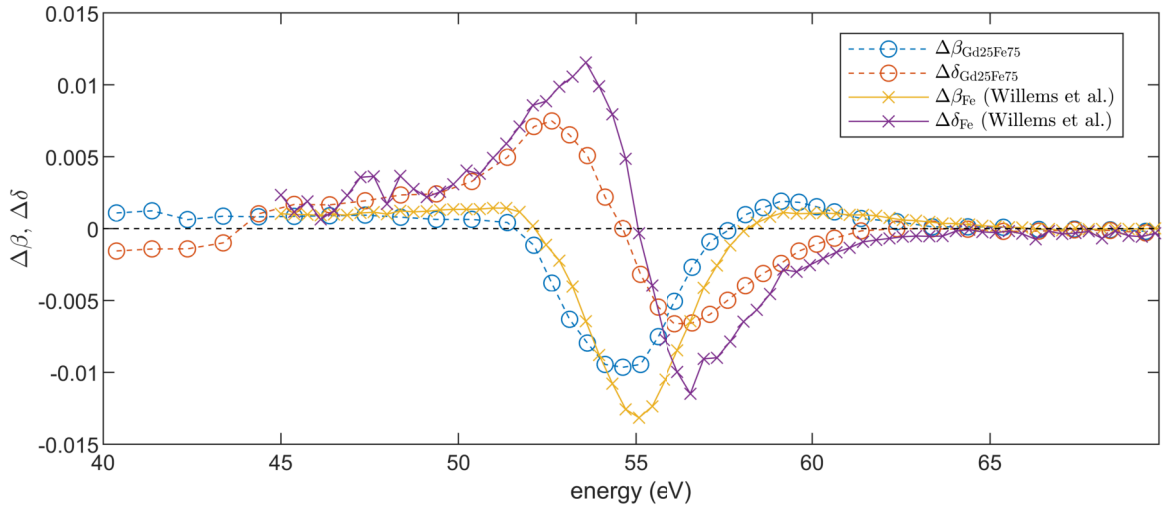

Figure 4.22: Comparison of the magneto-optical constants for the Fe content in $Gd_{25}Fe_{75}$ alloy with data measured by Willems et al. measured on a pure Fe sample [3] at the Fe M-edge.

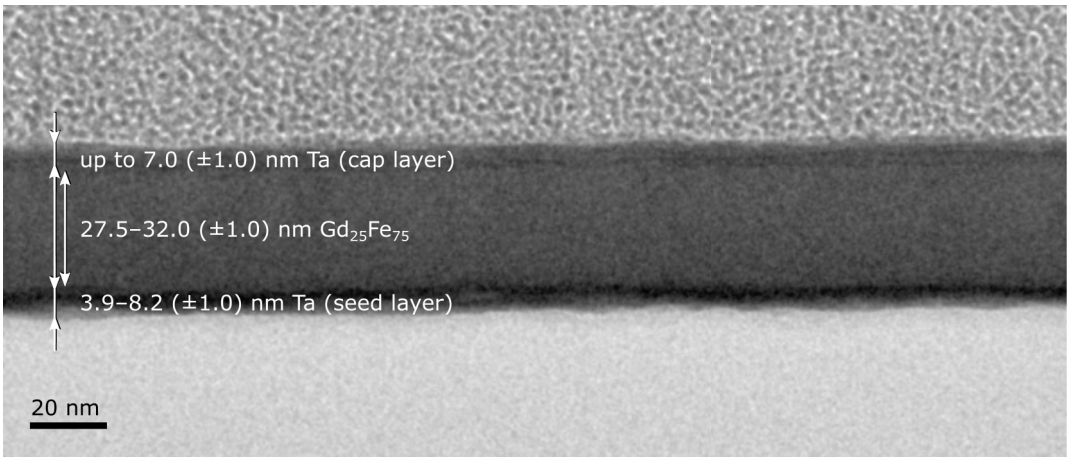

Figure 4.23: TEM slice of $Gd_{25}Fe_{75}$ alloy.

complex magneto-optical index are most likely accurate.

Besides the mismatch in the pre-edge and on-resonance values, it is noticeable that the post-edge $\Delta\beta$ becomes slightly more positive at around 59 eV. If our values of $\Delta\beta$ are scaled to match the on-resonant amplitude of $\Delta\beta$ from Willems et al., the post-edge peak is larger by 160 % in our measurement compared to the findings by Willems et al. This deviation from our data to the data of Willems et al. was also slightly visible in the comparison between our $Gd_{25}Co_{75}$ spectrum and the spectrum for pure Co from Willems et al. (Fig. 4.9). According to Willems et al., this difference can be attributed to a different magnitude of the exchange splitting of the semicore states.

4.3.2 Gd N-edge Resonance

The spectrum for the $Gd_{25}Fe_{75}$ sample at the Gd N-edge for both saturation field directions is shown in Fig. 4.24. The transition minimum can be found at 148.0 eV for positive

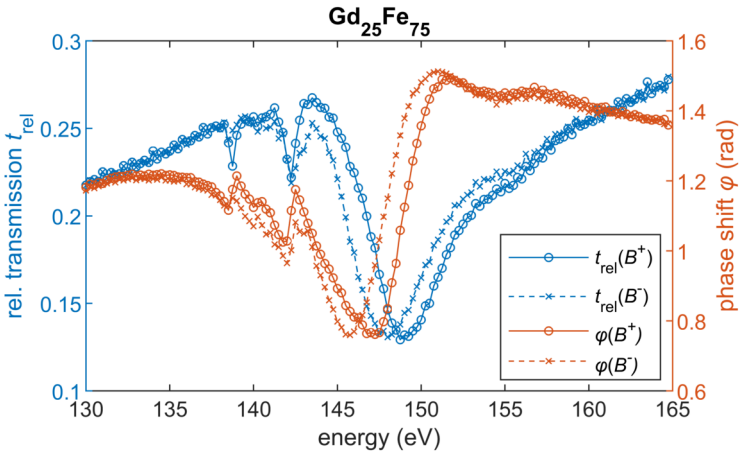

Figure 4.24: Spectroscopic response of relative transmission t_{rel} and phase shift φ at the Gd N-edge with circularly polarized light for the Si_3N_4(150 nm)/Ta(2 nm)/$Gd_{25}Fe_{75}$(30 nm)/Ta(2 nm) sample layer.

magnetization direction and at 148.8 eV for negative direction. Contrary to the energy shift of the N-edge resonance, the pre-edge features from 138 eV to 143.5 eV only change in amplitude for different magnetization directions. This observation is similar to the results from the results from the $Gd_{25}Co_{75}$ alloy in Ch. 4.2.2: The energy shift of the transmission for different magnetization orientations originates from the $4d^{10}\,4f^7[^8S] \rightarrow 4d^9\,4f^8[^8P]$ transitions and stems from a different allowed intermediate state. For parallel orientation of photon spin and sample magnetization, the $^8P_{5/2}$ state (148 eV) is populated, for anti-parallel orientation, the $^8P_{9/2}$ state (150 eV) [60].

In Fig. 4.25 (left panel), we show the normalized difference of the spectrum of both magnetization directions. On the right panel of Fig. 4.25, the magneto-optical constants of the Gd content in the $Gd_{25}Fe_{75}$ alloy are shown and compared to the ones from the $Gd_{25}Co_{75}$ measurements. The overall appearance of the spectrum of both alloys, from the pre-edge features to the resonance, and the off-resonant convergence to zero, matches very well. The only deviation is a small difference in the on-resonance values. That the deviation of both spectra is small is to be expected, since the electron configuration of Fe and Co are similar. However, we cannot exclude the possibility that an uncertainty in the composition of the $Gd_{25}Fe_{75}$ alloy leads to the small deviation of both spectra (see EDX discussion in Ch. 4.3.1). Other than that, the good agreement of the magneto-optical values for the Gd N-edge for both independently measured alloys increases the confidence in our new method.

4.3.3 Fe L-edge Resonance

In this subsection, we discuss the measurement of the Fe L-edge for the $Gd_{25}Fe_{75}$ sample. Due to experimental constraints, we could not change the sample-to-CCD distance to a more beneficial distance. The results are presented as a demonstration for the performance of the triple-slit method in an unfavourable experimental case.

As the scattering angle of the far-field diffraction pattern scales inversely with the photon energy, our measurement at the Fe L-edge started to have sampling problems.

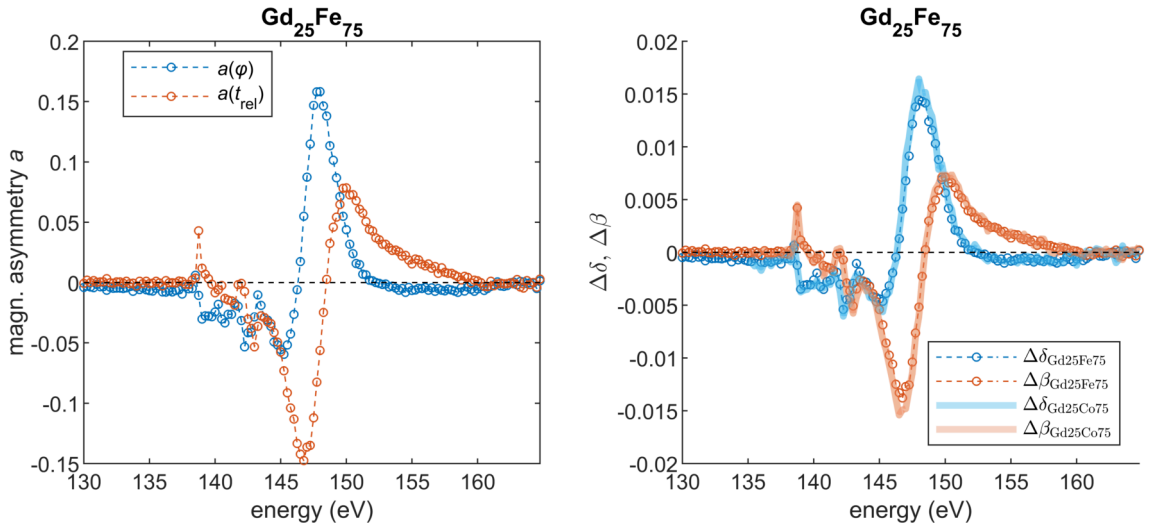

Figure 4.25: Spectroscopic response of the complex dichroic part of the optical constants for the Gd content of the $Gd_{25}Fe_{75}$ alloy at the Gd N-edge with circularly polarized light. Magnetic asymmetry a is shown on the left panel, the magneto-optical constants are shown on the right panel and compared to the magneto-optical constants of the Gd content from the $Gd_{25}Co_{75}$ alloy.

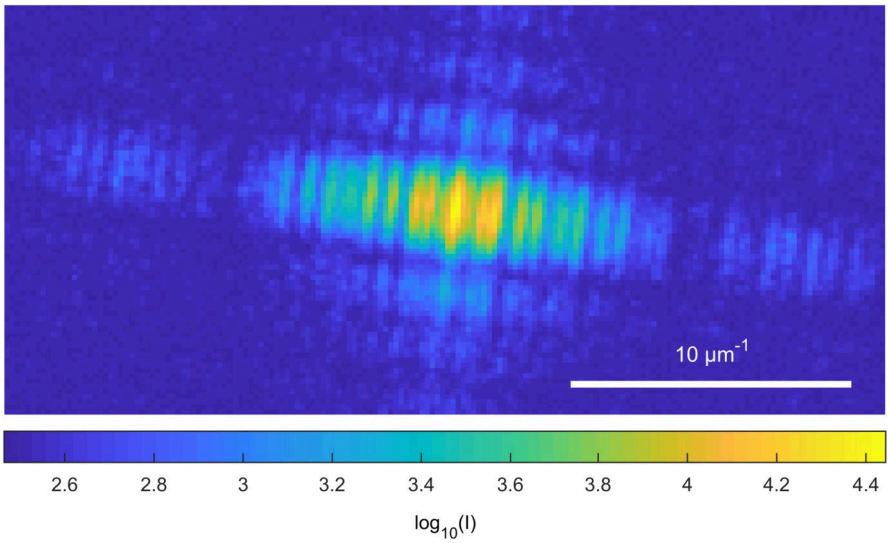

Figure 4.26: Center part of nearly undersampled triple-slit scattering from the $Gd_{25}Fe_{75}$ alloy at 730 eV.

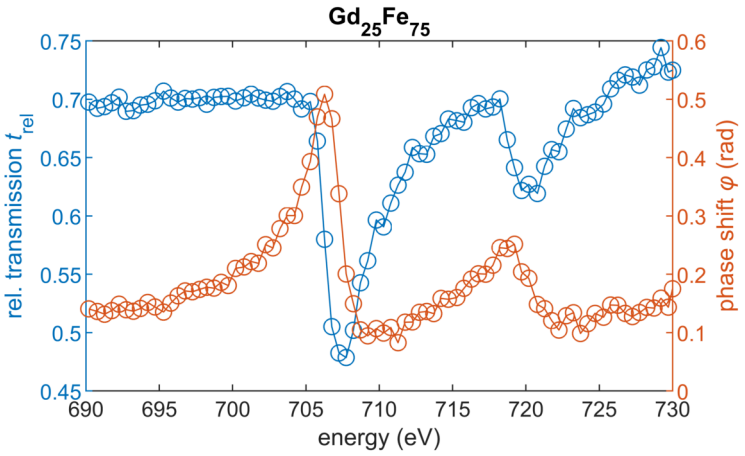

Figure 4.27: Spectroscopic response of relative transmission t_{rel} and phase shift φ at the Fe L-edge with circularly polarized light for the $Si_3N_4(150\,\mathrm{nm})/Ta(2\,\mathrm{nm})/Gd_{25}Fe_{75}(30\,\mathrm{nm})/Ta(2\,\mathrm{nm})$sample layer. The data was nearly undersampled. The relative transmission and phase shift in this figure was averaged over both magnetization directions.

We will discuss the effect of undersampling on the reconstruction process in detail in Ch. 5.2. Fig. 4.26 shows the center section of a scattering pattern at the Fe L-edge. The diffraction pattern appears slightly rotated because the sample was not mounted parallel to the axis of the CCD. In the case of a sufficiently sampled triple-slit diffraction pattern, this is not a problem, as the center line scan through the tilted axis of the Fourier transformation can be interpolated. In the case of undersampled data, this interpolation adds an additional error as the effective pixel size becomes larger in a diagonal direction. The undersampling in this data is apparent as the interference minima are slightly larger as the size of one pixel. From a certain degree, undersampling leads to an overlapping of cross-correlations between the slits whose interference can no longer be sufficiently sampled and the cross-correlations of the sufficiently sampled slit interference. This changes the plateau height of the affected cross-correlations and thus leads to an error in the measurement signal.

Besides this problem, the SNR of the data is low. Only the first diffraction maximum of the small vacuum slits had tolerable SNR. A weak signal for photons with higher momentum transfer leads to a reduction of the resolution of the cross-correlations. For a robust analysis of the triple-slit data, a clearly defined plateau of the cross-correlations is needed (see discussion to Eq.2.55 in Ch. 2.2.3). Any degeneration of this plateau and its amplitude, like through real space resolution loss, leads to errors in data analysis.

For the spectral response of the relative transmission and the phase shift shown in Fig. 4.27, we averaged over six neighbouring values for the relative transmission and phase shift (three of both magnetization directions) and binned them to their average photon energy. The spectrum shows clearly both L-edges. The L_3-edge can be found at 706.2 eV. In the literature, the L_3-edge is located at 706.8 eV [67]. The same energy shift of around 0.6 eV also appears at the L_2-edge, for which the literature noted the value 719.9 eV. Since we have not measured pure Fe, but a $Gd_{25}Fe_{75}$ alloy, we expect an energy shift to lower energies, due to the electronegativity of Gd compared to Fe. However, we

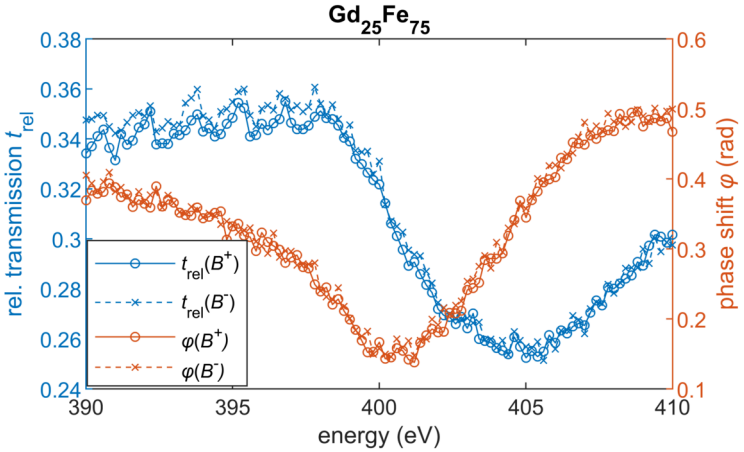

Figure 4.28: Spectroscopic response of relative transmission t_{rel} and phase shift φ from the Ta content from $Si_3N_4(150\,\mathrm{nm})/Ta(2\,\mathrm{nm})/Gd_{25}Fe_{75}(30\,\mathrm{nm})/Ta(2\,\mathrm{nm})$ at the Ta N-edge. The dichroic signal is most likely due to a relative beam-sample shift. The scan was done first for one magnetization direction followed by the other. The periodic artefact from the relative transmission stems from the fact that the reference slits had the same size.

cannot exclude an influence of the beamline calibration. The beamline was optimized for the Gd N-edge. It is still worth mentioning that despite the undersampled scattering data and the low SNR shown in Fig. 4.26, it is possible with our triple-slit method to clearly detect the Fe L-edges, provided we average over a sufficient number of data points.

The standard deviation for the relative transmission in the energy interval 690 eV to 703 eV (pre-edge) is $\sigma = 0.004$ and for the phase shift $\sigma = 0.005$ in the same energy interval. These standard variations should be sufficient to resolve the magneto-optical constants at the L-edge resonance through a XMCD difference measurement. However, we have used a different measurement routine for measuring the Fe L-edge spectrum than for the other data we have presented so far. Instead of alternating the magnetic saturation of the sample for every photon energy, we first recorded a spectrum for one magnetic saturation direction for the entire photon energy interval under investigation and then the spectrum for the other magnetic saturation direction. Due to the greater time interval between the acquisition of the associated XMCD data points, local beam parameters have changed and thus become impressed as errors in the measurement signal. In the next section and in Ch. 5.1 we will discuss this error in more detail.

4.4 SNR Analysis

Order of Data Acquisition

In this section, we continue to explore the experimental constraints of our interferometric triple-slit method. In the discussion about the data from the Fe L-edge we have seen that opposite magnetization states of the sample should be measured one after another in time. If the total spectrum is measured first for one magnetization state and then for the other, local beam parameters change over the longer time interval between the related XMCD pairs. This introduces errors to the analysis of the magneto-optical and optical constants.

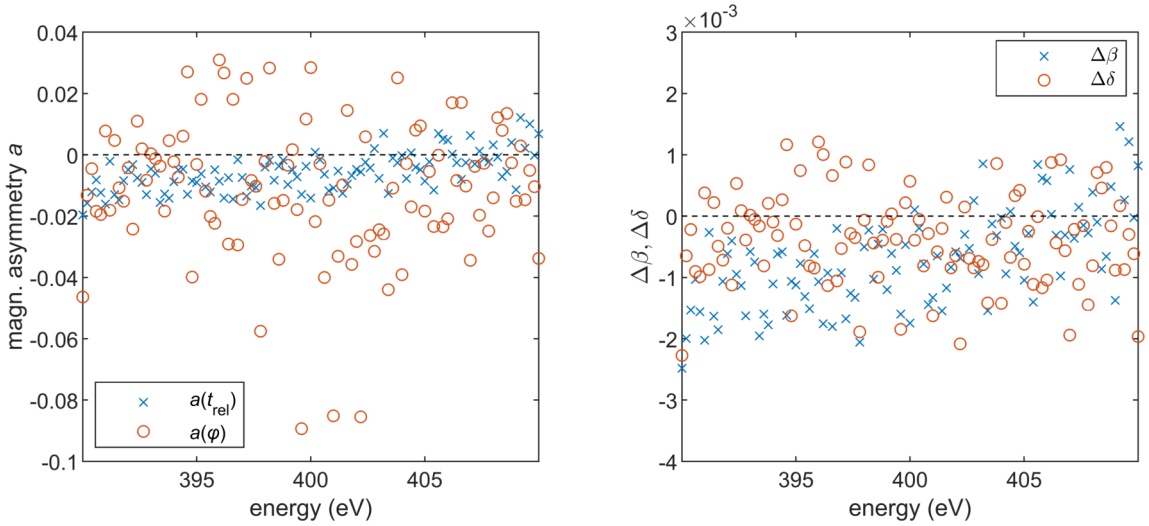

Figure 4.29: Spectroscopic response of the complex dichroic part of the optical constants at the Ta N_3-edge with circularly polarized light from the Si_3N_4(150 nm)/Ta(2 nm)/$Gd_{25}Fe_{75}$(30 nm)/Ta(2 nm) sample. The magnetic asymmetry a is shown on the left side, the magneto-optical constants are shown on the right side.

In order to analyse the errors introduced by the order of data acquisition, we measured the whole non-magnetic Ta N_3-edge spectra of the relative transmission and phase shift for one magnetic saturation directions followed by the other (Fig. 4.28). We measured the Ta spectrum with the same Si_3N_4(150 nm)/Ta(2 nm)/$Gd_{25}Fe_{75}$(30 nm)/Ta(2 nm) sample from Ch. 4.3, but a different triple-slit geometry, and the same setup as used during the Gd N-edge measurement. With an exposure time of 120 ms and a read-out time of 4 s, there is a minimal time difference between points for the same photon energy of $\Delta t =$ 7 min. We expect that no measurable dichroic signal should be present in the Ta spectra, as its magnetic susceptibility is $\chi = 154.0 \cdot 10^{-6}\,\mathrm{cm^3\,mol^{-1}}$ [72] and no resonance of Fe and Gd is overlapping with the Ta N_3-edge. Any difference between both spectra of different magnetization should be due to a change of the beam parameters (curvature of phase and amplitude) along the area of the triple-slit, making the plane wave approximation no longer applicable.

At 400.9 eV, we see a clear signature of Ta which was used in the sample as seed and capping layer to protect the $Gd_{25}Fe_{75}$ layer against oxidation. In the relative transmission (390–398 eV), a periodic artefact with a period of approximately 1.4 eV is visible. As described in Ch. 4.2.1, this artefact originates from sampling problems of the cross-correlation if both reference slits have the same width, which was the case for this triple-slit sample. The artefact can be avoided by proper choice of the slit width, as discussed in Ch.4.2.1. If present, the artefact can be corrected (see Fig. 4.5 c)) but was untreated here for demonstration purposes. As this periodic sampling artefact is only dependent on the experimental geometry and not on the magnetization of the sample, it will have no influence on the difference of the spectra. Furthermore, the SNR of the spectra is not optimal (comparable to the measurement at the Fe L-edge) and was caused by sampling problems of the scattering pattern. This problem is circumvented in our default setup with a suitable CCD to sample distance.

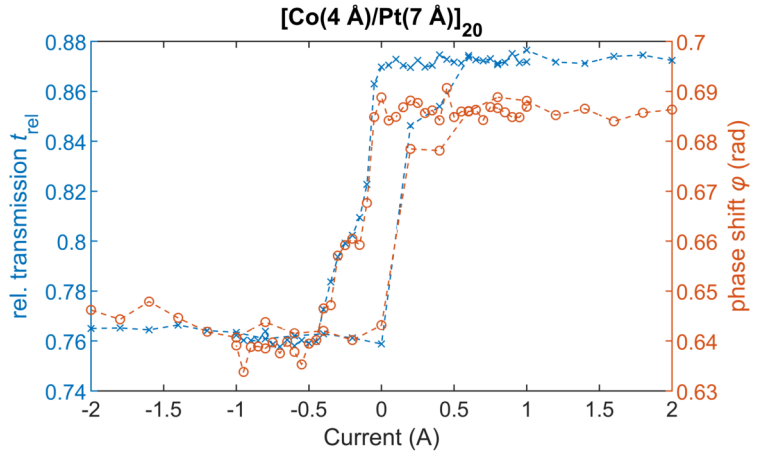

Figure 4.30: Hysteresis of the $[Co(4)Pt(7)]_{20}$ multilayer sample. The relative transmission t_{rel} and phase shift φ are measured by our triple-slit method. The conversion from current (A) to magnetic flux density (mT) can be found in Fig. 3.3.

The difference of both spectra normalized to the sum, and the resulting magneto-optical constants are shown in Fig. 4.29. A linear drift in the relative transmission is clearly visible. The acquisition time difference between related XMCD point was sufficient that the sample significantly drifted relative to the intensity profile of the incident beam. We note that the magnitude of the linear drift error is approximately one order of magnitude smaller than the magnitude of the resonant magneto-optical indices of the elements presented in this chapter. The dichroic signal of the phase shift shows constant noise ($\sigma = 0.022$) with no apparent dependence on linear beam drift. We attribute this behaviour to the fact that the phase is more strongly affected by the sampling problems of the scattering pattern than the amplitude.

From these findings, one can conclude that it is advisable to measure both saturation directions for one photon energy directly after the other to minimize drift artefacts. This, on the other hand, could still include a global drift in the non-difference spectra of the relative transmission and phase shift. To prevent this error, it is important that the incident phase front can be approximated with a plane wave for the whole photon energy range or the sample is realigned appropriately. The effects of beam drift and beam curvature are discussed in more detail in Ch. 5.1.

As we will see in the time-resolved data in Ch. 6, the magnitude and time-scale of the beam drift compared to the sample size and measurement times are a serious constraint for the experiment.

Magnetic Contrast and SNR

For the reconstruction of the magneto-optical indices, the sensitivity of the measurement signal to the sample magnetization plays an important role. To investigate the SNR of the magnetic difference signal, we measured the hysteresis of the $[Co(4)Pt(7)]_{20}$ multilayer sample (Fig. 4.30) with our triple-slit method.

The maximal magnetic difference signal for the $[Co(4)Pt(7)]_{20}$ multilayer sample has to correspond to two times the magnetization in its magnitude. This corresponds to the

difference of the relative transmission for both oppositely saturated states, amounting to 0.1110 ± 0.0006. The difference of the phase shift for both saturation direction corresponds to 0.0454 ± 0.0008. The error is given by the standard error. The relative error of the phase shift is much higher compared to the relative error of the transmission. This finding is in accordance with the simulations in the next chapter. The phase is much more prone to errors like beam drifts or violations of the plane wave approximation than the transmission.

Exposure Time and SNR

Lastly, we investigate the influence of the exposure time on the quality of the reconstructed asymmetry. This experiment used the same experimental geometry as the $[\mathrm{Co(4)Pt(7)}]_{20}$ multilayer measurements in Ch. 4.2.3. In Fig. 4.31, we show the absolute difference between the relative transmission t_{rel} and phase shift φ in relation to the weighted average, $\overline{t_{\mathrm{rel}}}$ and $\overline{\varphi}$, determined from the entire data. The absolute difference of the relative transmission is given by

$$\epsilon_{\mathrm{abs}}(t_{\mathrm{rel},n}) = |t_{\mathrm{rel},n} - \overline{t_{\mathrm{rel}}}| \tag{4.6}$$

and the absolute difference for the phase reads:

$$\epsilon_{\mathrm{abs}}(\varphi_n) = |\varphi_n - \overline{\varphi}|, \tag{4.7}$$

with the weighted average

$$\overline{t_{\mathrm{rel}}} = \frac{\sum t_{\mathrm{exp.},n} t_{\mathrm{rel},n}}{\sum t_{\mathrm{exp.},n}} \tag{4.8}$$

and

$$\overline{\varphi} = \frac{\sum t_{\mathrm{exp.},n} \varphi_i}{\sum t_{\mathrm{exp.},n}}, \tag{4.9}$$

respectively. Here, $t_{\mathrm{exp.},n}$ denotes the exposure time of the n-th measurement from the exposure time series.

For higher exposure times (around 1500 ms), the absolute difference converges to stable values ($\epsilon_{\mathrm{abs}}(t_{\mathrm{rel},1500\,\mathrm{ms}}) = 0.0011$ and $\epsilon_{\mathrm{abs}}(\varphi_{1500\,\mathrm{ms}}) = 0.0028$). For lower exposure times, the fluctuations of the absolute difference increases. These fluctuations are due to dominance of shot noise for the lower exposure times, as expected from the Poisson distribution.

The effects of different exposure times, like shot noise and resolution cut-off, will be discussed in greater detail in Ch. 5.

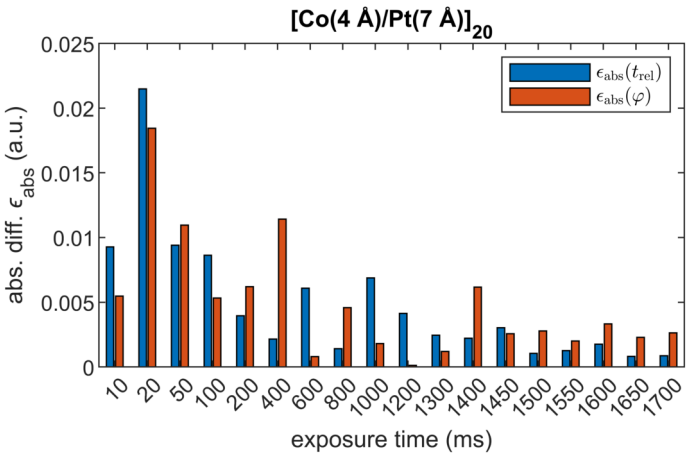

Figure 4.31: Absolute differences between the relative transmission (phase shift) and their respective weighted averages for different exposure times.

CHAPTER 5

Simulations of Experimental Parameters

In this section, we will model the influence of experimental noise and different geometric parameters on the analysis of the triple slit data to determine the main sources of error and to find optimal experimental parameters for the sample, source, and setup to improve the practical application of the method.

In general, our simulation focuses on two aspects: the incident wave on the sample surface and the far-field wave measured by the detector, and their respective influence on the amplitude and phase of the slits cross-correlation plateaus. The data analysis of the simulated triple-slit diffractions is performed similar to the data analysis presented in the last chapter.

5.1 Beam Divergence and Curvature

Beam divergence plays a crucial part in the triple-slit experiment. On the one hand, it is favourable that as much light as possible is transmitted through the slits, on the other hand, the incident wave front should be as homogeneous as possible. One has, therefore, to find a trade-off between efficient use of photons towards the focal position and a robust and uniform illumination. This is especially important for the HHG source as photon flux and beam stability are limiting issues for this transmission experiment. In this section, we are investigating both the effect of incident wave front curvature across the area of the three slits as well as the influence of beam drift orthogonal to the optical axis for XMCD difference measurements.

In Fig. 5.1, we demonstrate the influence of a Gaussian beam curvature in combination with an orthogonal beam drift on triple-slit transmission. The beam parameters were chosen to be comparable to the HHG experiment. For this simulation, the following derivation was used. The complex electric field vector $\boldsymbol{\psi}(r,z)$ of a Gaussian beam propagating in $+z$-direction with a polarization in the x-direction is given by [73]:

$$\boldsymbol{\psi}(r,z) = \psi_0 \hat{\boldsymbol{e}}_x \frac{w_0}{w(z)} \exp\left(\frac{-r^2}{w(z)^2}\right) \exp\left(-i\left(kz + k\frac{r^2}{2R(z)} - \psi(z)\right)\right). \tag{5.1}$$

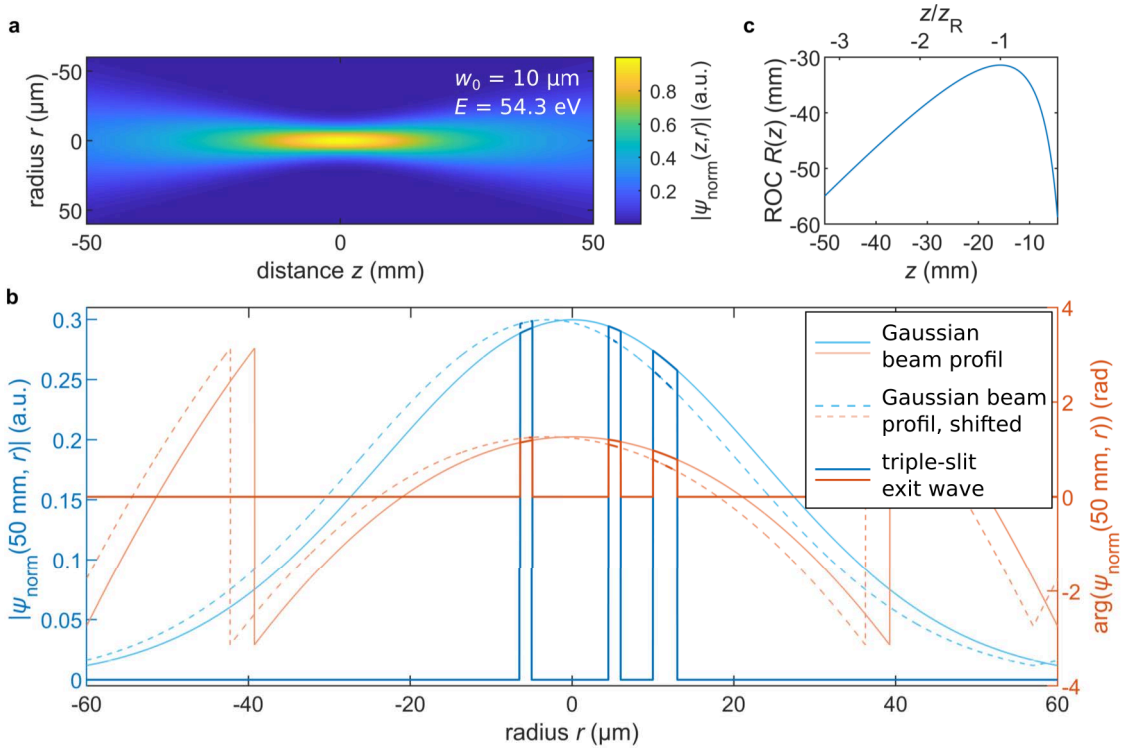

Figure 5.1: Effects of curvature and beam drift orthogonal to the optical axis on the triple-slit transmission. **a** Simulation of a normalized Gaussian beam amplitude $|\psi_{\mathrm{norm}}(z, r)|$ as a function of the focus distance z and radius r for a photon energy of 54.3 eV. A beam waist of $w_0 = 10\,\mu\mathrm{m}$ was used, which is comparable to the beam in the HHG experiment. **b** Demonstration of the triple-slit exit wave depending on curvature and beam drift orthogonal to the optical axis. A line scan orthogonal to the optical axis through the Gaussian beam at the $z = -50\,\mathrm{mm}$ plane is shown. The amplitude and phase of the Gaussian beam profile are given in light blue and light orange. The transmission profile through three vacuum slits is indicated by more saturated colors. The Gaussian beam profile is shifted by $\Delta r = 3\,\mu\mathrm{m}$ for demonstration purpose (dashed line). **c** Radius of curvature (ROC) $R(z)$ of the wave front for the beam given in **a** as a function of distance to the focus. The wave fronts have the strongest curvature (the smallest ROC) one Rayleigh length z_{R} away from the focus. At this point, the error in the phase reconstruction reaches its maximum.

Here, r denotes the radial coordinate, z the distance from the focus along the propagation direction, and k the wave number. The Gaussian beam parameters are given by the $1/e$-value of the radial field amplitude $w(z)$, the beam waist radius at the focal position $w_0 = w(0)$, the radius of curvature $R(z)$, and the Gouy phase $\psi(z)$.

In Fig. 5.1a, the Gaussian beam amplitude profile around the focus position is shown. The beam waist of $w_0 = 10\,\mu\text{m}$ is comparable to the focus diameter during the HHG experiment as is the photon energy of $E = 54.3\,\text{eV}$. From the intensity profile around the focus position, it can be derived that the radial decrease in intensity causes a deviation from a plane wave illumination across the area of the three slits that is stronger the closer the slits are to the focus. Would the beam be stable over the time frame of the experiment, the inhomogeneous illumination would cause an offset for the measurements of the optical constants. For measurements investigating the difference in two sample states, however, this is not a concern, as the curvature effects cancel out each other. Only when combined with beam drift orthogonal to the optical axis between the two exposures for the different sample states, beam curvature becomes a problem.

Figure 5.1b visualizes both sources of error at a distance of $z = -50\,\text{mm}$ to the focus of the Gaussian beam shown in Fig. 5.1a and for a slit geometry with a maximal spacing between the slits of $19\,\mu\text{m}$[1]. The measurement signal is based on the relation of the slit's profile heights. Any change in this relative height that is not due to a change in the sample response causes an error to the reconstruction.

For the reconstruction of the sample's magnetic properties, only the difference of two measurements is important. From Fig. 5.1b we can see that if the curvature of the beam would be stable in the time frame of the two measurements, the curvature error would cancel itself out. However, a relative orthogonal shift between the beam and the three slits would change the height of the slit transmission profile in dependence of the local beam curvature. This shift would, therefore, lead to an error in the reconstruction of the magnetic properties.

From Eq. 5.1 and Fig. 5.1a, it is apparent that the curvature of the amplitude decreases with the distance to the focus. The phase curvature, however, does not decrease monotonously with z. Figure 5.1c shows the radius of curvature (ROC) $R(z)$ as a function of distance to the focal position. We can see that the absolute value of the ROC has a minimum at $z = z_R$, where $z_R = \pi w_0^2/\lambda$ refers to the Rayleigh range[2]. At this point, the curvature of the phase fronts is maximal as is the error in the reconstructed dispersive part of the optical indices. For the experiments, it is, therefore, important to be sufficiently far away from the Rayleigh range of the beam. In the remaining part of this section, we will quantify our consideration regarding the error caused by the beam curvature and the beam drift.

As we have seen in Ch. 2.2.3, the central quantities for the reconstruction are the magnitudes of the cross-correlations c_{nm} between the slits, where we used the label 1 for the material slit, and 2 and 3 for the reference slits. We now ask for the error in c_{nm} if the illumination of slit n and m is not a plane wave. Equation 2.56 implies that the

[1]For demonstration purposes, the amplitude and phase transmission profiles are shown for three vacuum slits, instead of two vacuum slits and one slit containing material layers.

[2]The Rayleigh range is defined by the distance to the beam waist w_0 where the area of the beam's cross-section is doubled.

cross-correlation c_{12} between the material and a vacuum slit is proportional to:

$$c_{12} \propto e^{-\beta kd} e^{i\delta kd} |\psi_{\mathrm{c}}|^2. \tag{5.2}$$

If we substitute the incident plane wave ψ_{c} with the mean value of the Gaussian beam from Eq. 5.1 at the area of the nth slit

$$\psi_n = a_n e^{-i\phi_n}, \tag{5.3}$$

with the mean amplitude of the Gaussian beam called a_n and the mean phase called ϕ_n, Eq. 5.2 becomes:

$$\begin{aligned} c_{12} &\propto e^{-\beta kd} e^{i\delta kd} \psi_1^* \psi_2 && (5.4)\\ &\propto e^{-\beta kd} e^{i\delta kd} a_1 a_2 e^{-i(\phi_2 - \phi_1)}. && (5.5) \end{aligned}$$

With the cross-correlation between both reference slits

$$\begin{aligned} c_{23} &\propto \psi_2^* \psi_3 && (5.6)\\ &\propto a_2 a_3 e^{-i(\phi_3 - \phi_2)}, && (5.7) \end{aligned}$$

the normalized cross-correlation equals:

$$\begin{aligned} |c_{12}^{\mathrm{n}}| &= \left| \frac{c_{12}}{c_{23}} \right| && (5.8)\\ &= e^{-\beta kd} \frac{a_1}{a_3}. && (5.9) \end{aligned}$$

From this, we see that the cross-correlation $|c_{12}^{\mathrm{n}}|$ differs from that for a plane wave by the ratio of the amplitudes a_1/a_3 of the incident beam at the position of the material slit and one vacuum slit. As the material slit with the label 1 and the reference slit with the label 3 are furthest apart, their amplitude ratio is prone to the strongest deviation in presents of beam curvature. It could be beneficial to use the normalized cross-correlation c_{13}/c_{23} for the reconstruction, as it will result in the amplitude ratio a_1/a_2 of slit 1 and slit 2, which are closer together and, therefore, experience less curvature error. However, this method must be weighed against possible coherence problems that could arise when using the cross-correlation c_{13} between the material slit 1 and the reference slit 3, which are spaced furthest apart in the slit geometry.

From Eq. 5.9, we see that the absorptive part of the optical index in the presence of beam curvature is given by:

$$\beta = -\frac{\ln(|c_{12}^{\mathrm{n}}|)}{kd} + \frac{1}{kd} \ln\left(\frac{a_1}{a_2}\right) \tag{5.10}$$

The error of β is given by $\varepsilon_\beta(w(z), r)$, which depends[3] on the $1/e$ beam radius $w(z)$ and the radial distance r of the slit's position to the center of the Gaussian beam:

$$\varepsilon_\beta(w(z), r) = \frac{1}{kd} \ln\left(\frac{a_1}{a_2}\right). \tag{5.11}$$

[3]Both variables $w(z)$ and r are effecting the local averaged amplitude a_n

This error scales with the wave number k and the layer thickness d. For this reason, we define the exponent error $\varepsilon_a(w(z), r)$, which is only dependent on the local Gaussian beam parameters.

$$\varepsilon_a(w(z), r) = \ln\left(\frac{a_1}{a_2}\right). \tag{5.12}$$

In a similar way, we arrive from Eq. 5.5 to the dispersive part of the refractive index:

$$\delta = \frac{\arg(c_{12})}{kd} + \frac{(\phi_2 - \phi_1)}{kd}. \tag{5.13}$$

Here, the phase difference $\phi_2 - \phi_1$ between the material slit 1 and the reference slit 2 is responsible for the error of δ:

$$\varepsilon_\delta(w(z), r) = \frac{(\phi_2 - \phi_1)}{kd}. \tag{5.14}$$

As for the error of β, the error $\varepsilon_\delta(w(z), r)$ depends on the product kd. The error of the reconstructed phase is independent of kd and is given just by the incident phase difference at the position of the two slits:

$$\varepsilon_\phi(w(z), r) = \phi_2 - \phi_1. \tag{5.15}$$

The errors ε_δ and ε_ϕ are directly related to the geometry of the three slits. The larger the spacing between the slits, the larger is the effect of the curvature of the Gaussian beam. For the simulation in this section, we used the triple-slit geometry shown in Fig. 5.1b which is comparable to the geometries we used in this thesis.

Figure 5.2a and 5.2b depict the kd independent error ε_a and ε_ϕ as a function of beam radius $w(z)$, ROC $R(z)$, and radial distance r of the triple-slit to the center of the Gaussian beam. The range of the beam radius $w(z)$ and the range of the ROC $R(z)$ of both radiation sources, HHG and synchrotron radiation, available at the sample position during our experiments, are indicated by dashed lines[4]. To quantify the errors in relation to the experimental parameters, Fig. 5.2 shows the threshold curves were the relative errors $\varepsilon_\beta^{\text{rel}}$ and $\varepsilon_\delta^{\text{rel}}$ reaches 1 % of their respective optical constants. As stated before, this threshold curve depends on the photon energy E and the layer thickness d. As the errors ε_β and ε_δ are larger for larger wavelengths, we show the 1 % threshold curves for the Fe M-edge to give a worst case estimation for our experiments. At the Fe M-edge, we used the most favourable and unfavourable photon energies, i.e., the photon energies in the M-edge energy interval where the absolute value of the optical indices and magneto-optical indices is largest or smallest, respectively, for the threshold curves, to give an upper and lower bond of the threshold curve. As layer thickness, we used 15 nm of Fe. On the basis of Fig. 5.2a and 5.2b, we will first discuss the errors due to the triple-slit position r in relation the the beam center, the beam radius $w(z)$, and the ROC $R(z)$ at the synchrotron radiation source, followed by the errors for the HHG experiment.

From Fig. 5.2a, we see that our triple-slit experiment with synchrotron radiation at the Fe M-edge, where the beam radius was approximately 90 µm, could in the worst

[4]Note that the simulation assumes a perfect Gaussian profile, which is only an approximation to the experimental intensity distribution of the beam.

case tolerate a radial shift of 0.2 µm at 52.1 eV from the beam center before the error ε_β becomes larger than 1 %. During our synchrotron experiments, the alignment accuracy of the sample to the center of the beam was sufficiently accurate. Therefore, the curvature error for the determination of the β is negligible.

We estimate the ROC $R(z) = z(1 + (z_\mathrm{R}/z)^2)$, with z_R being the Rayleigh length, of the synchrotron beam with a photon energy near the Fe M-edge at our sample position to be approximately $R(z) = 7.5\,\mathrm{m}$ (see Tab. 3.2 for an overview of the geometrical parameters used during our experiments). In Fig. 5.2b, we show only one threshold line, because the difference between the threshold lines for different energies in the M-edge energy interval is not significant. We can see from Fig. 5.2b that in the synchrotron radiation ROC interval a radial deviation from the optimal position of even 10 µm would not cause the error ε_δ to be larger than 1 %.

The radiation we used from the HHG source had a beam radius of around 40 µm ($z_0 = 70\,\mathrm{mm}$) and an estimated ROC of 54 mm. While the beam size is in the same order of magnitude as the beam at the synchrotron source, the ROC of the HHG radiation is two orders of magnitude smaller than the beam of the synchrotron source. The smaller ROC is due to the smaller focus length of the focussing optics due to experimental constraints of our HHG setup.

Figure 5.2a shows the 1 % threshold line for the worst case magnitude of β ($E = 52.1\,\mathrm{eV}$) at a radial distance of around 50 nm from beam center. This radial distance is close to position accuracy of our sample stage.

The error ε_ϕ in Fig. 5.2b shows a minimum at a radial displacement of -5.5 µm. This distance corresponds with the radial displacement of the triple-slit from their center position to the position, where the material slit and the adjacent reference slits are exactly at opposite sides of the Gaussian beam profile, i.e., where the phases are the same at both slit positions. Around the radial displacement of -5.5 µm, a radial positioning error greater than 50 nm will lead to an error of $\varepsilon_\delta > 1\,\%$

Comparing Figure 5.2a and Figure 5.2b, it is noticeable that for a ROC $R(z) < 4\,\mathrm{m}$ (in combination with the simulated experimental parameters) there is no radial position of the triple-slit sample in the beam where the errors ε_β and ε_δ simultaneously become negligible. For the determination of the optical indices at a HHG source, one, therefore, needs a focussing optic with a longer focus length to increase the ROC of the phase and to reduce the error $\varepsilon_\delta(w(z), r)$ of the real part of the optical index.

The work presented in this thesis did only use synchrotron radiation for the determination of the optical constants. The HHG source was applied to determine the temporal change of the magneto-optical index of Fe after optical excitation. The benefit of the magneto-optical index calculation is that all beam curvature errors cancel out if they are the same for both sample magnetization directions. Similar to the cross-correlations from Eq. 5.5 and Eq. 5.7, the cross-correlations for the uniform magnetized sample are

$$c_{12}^{\pm} = e^{-(\beta \pm \Delta\beta)kd} e^{i(\delta \pm \Delta\delta)kd} a_m^{\pm} a_{r_1}^{\pm} e^{-i(\phi_{r_1}^{\pm} - \phi_m^{\pm})} \tag{5.16}$$

and

$$c_{23}^{\pm} = a_{r_1}^{\pm} a_{r_2}^{\pm} e^{-i(\phi_{r_2}^{\pm} - \phi_{r_1}^{\pm})}, \tag{5.17}$$

where the $\pm$ exponent symbolizes the magnetization direction.

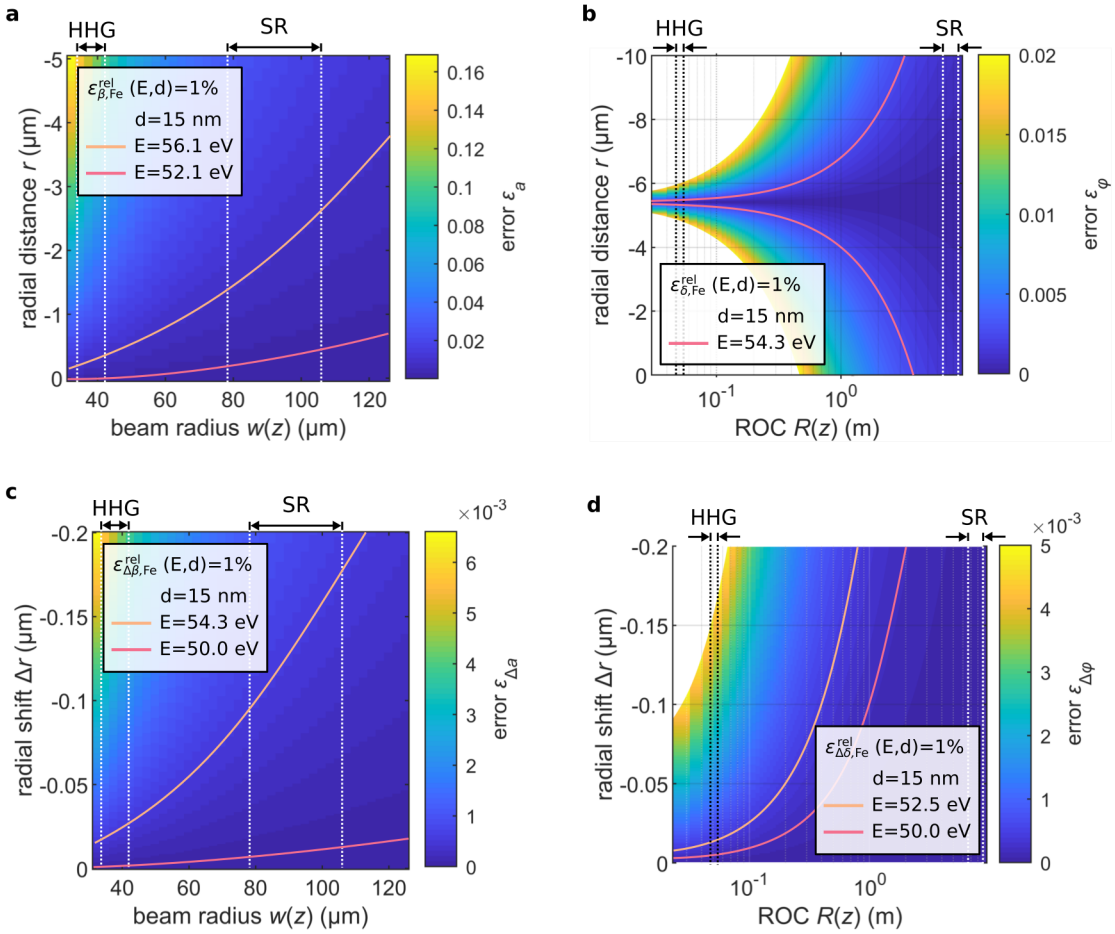

Figure 5.2: Relative 1 % threshold errors of the optical indices (magneto-optical indices) for Fe in the presence of beam curvature and radial distance r between the triple-slit position and the optical axis (radial sample-beam shift Δr between exposures). Note that the displayed errors depend on the geometry of the triple-slit. For this simulation, we used a triple-slit geometry similar to the one in Fig. 5.1. Intervals of the beam curvature parameters are marked by white dashed lines and are labeled HHG (SR) if they matched the beam parameters used during our HHG (synchrotron) experiments. To quantify the errors, threshold lines are given for the worst and best case photon energies around the Fe M-edge (specified by the respective inset), where the error of the optical or magneto-optical constants exceeds 1 %. **a** The error ε_a represents the change in the reconstructed real part of the logarithm of the material-reference slit cross-correlation c_{12}^{n} and is given as a function of beam radius $w(z)$ and radial distance r of the sample to the optical axis. **b** The error ε_ϕ of the imaginary part of the exponent of c_{12} is given as a function of ROC R and radial distance of the sample position to the optical axis. The dependency of ε_ϕ on R is shown in logarithmic scale. **c** The error $\varepsilon_{\Delta a}$ describes the logarithmic difference between $|c_{12}^{\mathrm{n},+}|$ and $|c_{12}^{\mathrm{n},-}|$ as a function of beam radius w and radial beam-sample shift Δr between the scattering patterns on which the cross-correlations are based. **d** The error $\varepsilon_{\Delta\phi}$ gives the difference change between the phases of c_{12}^{+} and c_{12}^{-} as a function of Δr, and R in logarithmic scale.

Comparable to the derivation in Ch. 2.4, the magneto-optical constants in the presence of beam curvature results in:

$$\Delta\beta = -\frac{1}{2kd}\left(\ln\left(\frac{c_{12}^{\mathrm{n},+}}{c_{12}^{\mathrm{n},-}}\right) - \ln\left(\frac{a_m^+}{a_m^-}\right) - \ln\left(\frac{a_{r_2}^-}{a_{r_2}^+}\right)\right) \tag{5.18}$$

and

$$\Delta\delta = \frac{\arg(c_{12}^+) - \arg(c_{12}^-)}{2kd} + \frac{\phi_{r_1}^+ - \phi_{r_1}^-}{2kd} + \frac{\phi_m^- - \phi_m^+}{2kd}. \tag{5.19}$$

The last two terms of Eq. 5.18 and Eq. 5.19 will become zero individually if the local beam curvature does not change between both exposures for the different magnetization states of the sample layer.

The errors the magneto-optical index are give by:

$$\varepsilon_{\Delta\beta}(w(z), r) = \frac{1}{kd}\ln\left(\frac{a_m^+}{a_m^-}\right) + \ln\left(\frac{a_{r_2}^-}{a_{r_2}^+}\right) \tag{5.20}$$

and

$$\varepsilon_{\Delta\delta}(w(z), r) = \frac{\phi_{r_1}^+ - \phi_{r_1}^-}{2kd} + \frac{\phi_m^- - \phi_m^+}{2kd}. \tag{5.21}$$

Figure 5.2c and Fig. 5.2d show the errors which result from a radial sample-beam shift between both exposures as a function of beam radius and ROC. The errors are displayed independently of the product kd and are called:

$$\varepsilon_{\Delta a}(w(z), r) = \ln\left(\frac{a_m^+}{a_m^-}\right) + \ln\left(\frac{a_{r_2}^-}{a_{r_2}^+}\right) \tag{5.22}$$

and

$$\varepsilon_{\Delta\phi}(w(z), r) = \phi_{r_1}^+ - \phi_{r_1}^- + \phi_m^- - \phi_m^+. \tag{5.23}$$

Figure 5.2c and Fig. 5.2d also display threshold curves, above which the errors $\varepsilon_{\Delta\beta}$ and $\varepsilon_{\Delta\delta}$ rise over 1 % of the magnitude of their magneto-optical constants. In our HHG experiment, we used the harmonic centred at 54.3 eV. At this photon energy, $\Delta\beta$ has a maximum and is, therefore, most robust against a radial sample-beam shift Δr between both exposures. For our HHG setup, we estimated a radial shift of $\Delta r = 25$ nm between two corresponding exposures to cause an error of approximately 1 % to $\Delta\beta$. As typical exposure time at our HHG source was around 30 s, special care to the sample alignment and beam stability was necessary.

At the photon energy of 54.3 eV, $\Delta\delta$ is close to zero. Therefore, every small change in sample position between two exposures in the presence of beam curvature will lead to a significant contribution of $\varepsilon_{\Delta\delta}$ to the measured dispersive part of the magneto-optical index.

As we see in Fig. 5.2c and Fig. 5.2d, our beam of the synchrotron radiation source provided better conditions in the presence of relative beam-sample drift between two corresponding exposures. For the worst case (Fe at 50.0 eV), a relative sample-beam drift

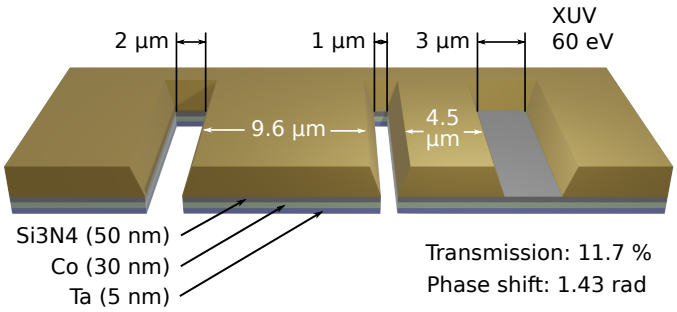

Figure 5.3: Cutaway drawing for the simulated triple slit sample. The calculations in this section are based on this sample geometry. The slits are 4 µm in height. The frame (golden color) is intransparent, the two 2 µm and 1 µm vacuum slits are fully transparent. The transmission and phase shift for light (60 eV) through the material layer are 11.7 % and 1.43 rad. The material layers consist of 50 nm Si_3N_4, 30 nm Co and 5 nm Ta. In the simulations, the whole sample is illuminated by 60 eV XUV with varying beam profiles. The slits are numbered from right to left (slit 1: material slit, slit 2: middle reference slit, slit 3: left reference slit).

of 12 nm between exposures will lead to an error of 1 % to $\Delta\beta$, for the best case (Fe at 54.3 eV), a relative sample-beam drift of approximately 130 nm will cause the 1 % error to $\Delta\beta$. The ROC of the synchrotron radiation at the sample position was sufficient that even a radial shift between sample and beam of 200 nm would only cause an error to $\Delta\delta$ significantly below 1 %.

The more the incident beam resembles a plane wave, the smaller the errors $\varepsilon_{\Delta\beta}$ and $\varepsilon_{\Delta\delta}$ will become. To improved our HHG experiment, a longer focus length to reduce the beam curvature is advisable. To measure the dynamic of $\Delta\delta$, it would also be beneficial to select a harmonic close to 52.5 eV to reduce the effect of $\varepsilon_{\Delta\delta}$ to $\Delta\delta$.

5.2 Sample-Detector Distance

The sample geometry, which is used throughout the last part of this chapter, is depicted in Fig. 5.3. All slits are 4 µm in height. For the two vacuum slits, different widths are used (2 µm and 1 µm). This ensures that there are no sampling problems in the reconstruction as it was discussed in Ch. 4.2.1. For the slit with the sample layer, the widest aperture (3 µm wide) is used. As the sample layer and the substrate layer are absorbing a significant fraction of the incident photons, the larger dimensions of the slit ensure sufficient transmission from this slit in relation to the transmission from the two vacuum slits. The slits are numbered from right to left (slit 1: material slit, slit 2: middle reference slit, slit 3: left reference slit). The distances between the slits are chosen such that the size of the the reconstructed cross-correlations would fit in between. The transmission of the sample layer was modelled by utilizing the optical constants of Si_3N_4 and Ta from CXRO [48] and the optical constants of the Co M-edge from Willems et al. [3].

First, we investigate the relation of the sample-detector distance and the quality of

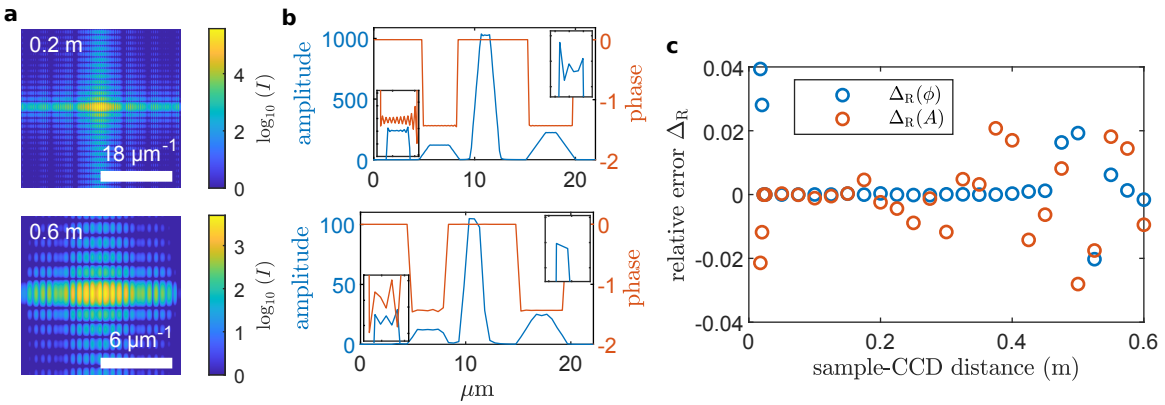

Figure 5.4: Simulation of triple-slit scattering with varying distance between sample and CCD. **a**, Scattering images of triple-slits for 0.2 m and 0.6 m CCD-sample distance plotted in logarithmic scale. **b** Center slice thorough cross-correlations of the three slits. Only the right half without autocorrelation is shown. The cross-correlation of the material slit with the small vacuum slit equals the left plateau peak (correspondingly: vacuum-vacuum cross-correlation equals middle plateau, material-large vacuum slit equals right plateau). The inset in the lower left (upper right) displays a 20 times scaled region of the left (middle) plateau. The upper (lower) panel corresponds to the 0.2 m (0.6 m) sample CCD distance scattering pattern on the left in **a**. **c** Relative error of the reconstructed phase shift and transmission amplitude to ground truth as a function of sample-CCD distances.

the amplitude and phase of the cross-correlations. The intensity values of the diffraction pattern will not be discretized into photon counts nor is there any thresholding to simulate CCD dynamic range. Any errors in the reconstruction originate from the windowing (also called apodization [74]) of the infinite diffraction pattern by the finite area and the sampling of the diffraction pattern on a finite pixel grid.

Figure 5.4c shows the resulting relative error Δ_{R} of the cross-correlation phase ϕ and normalized amplitude A as function of sample-CCD distance. The normalized amplitude A is given by dividing the cross-correlation c_{12} by c_{23}. For two selected sample-CCD distances (0.2 m and 0.6 m), the corresponding triple-slit scattering pattern are shown in Fig. 5.4a and the corresponding three cross-correlations in Fig. 5.4b. The auto-correlation (located at 0 µm) is not shown in Fig. 5.4b. The cross-correlation c_{12} is located at 6.5 µm, c_{23} at 11.0 µm, and c_{13} is located at 17.5 µm. The indices of the cross-correlation refer to the number of the slit (see Fig. 5.3). The cross-correlation c_{12} (c_{23}) is displayed 20 times magnified in the insets on the left (right) side of Fig. 5.4b.

From Fig. 5.4c, two regions can be identified in which the relative error diverges ($<$ 0.023 m and $>$ 0.15 m). The sample-CCD distance has a lower bound for our interferometric method. To use a discrete Fourier transformation as the reconstruction operator (see Appendix A for the triple-slit analysis protocol), the far field approximation must be valid. To test for this approximation, the Fresnel number $F = a^2/L\lambda$, with a: aperture size, L: distance from the aperture and λ: wavelength, provides a useful measure. If $F \ll 1$, far field diffraction occurs. For a photon energy of 60 eV and an aperture size in the range of 20 µm, the lower bound distance is in the range of 50 mm. Besides this lower bound for the sample-CCD distance, the pixelation of the CCD introduces another constraint on the minimal distance. If the distance is too small, the diffraction pattern will get undersampled (see first two data points in Fig. 5.4c).

The upper bound distance depends on the capability of the detector size to measure a certain amount of the angular distribution of the diffraction pattern. In our experiments and in this simulation, we used a 2048×2048 pixelated detector with a single pixel size of 13.5 µm. We find in general that for tolerable signal-to-noise ratio, the size of the detector must be large enough to measure at least up to the third order of the slit interference pattern.

The diagram of the relative error Δ_R in Fig. 5.4c shows a different behaviour for amplitude A and phase ϕ of the reconstructed signal for larger distances ($>$0.2 m). The relative error of the phase is much more stable to the resolution loss for higher distances than the relative error of the amplitude. Comparing this observation to the diagram of the cross-correlation (Fig. 5.4b), we noticed a different behaviour of amplitude (blue) and phase (red). The distortion on the plateau of the phase cross-correlation is stronger than for the amplitude plateau. This translates to the opposite behaviour of the relative errors when one normalizes the material-reference cross-correlation c_{12} with the reference cross-correlation c_{23} to get the normalized amplitude A. The reference slits are smaller than the material slit and are, therefore, more affected by the resolution loss when increasing the distance between CCD and sample. The phase signal, on the other hand, does not use normalization and is, therefore, not affected by an additional noise source.

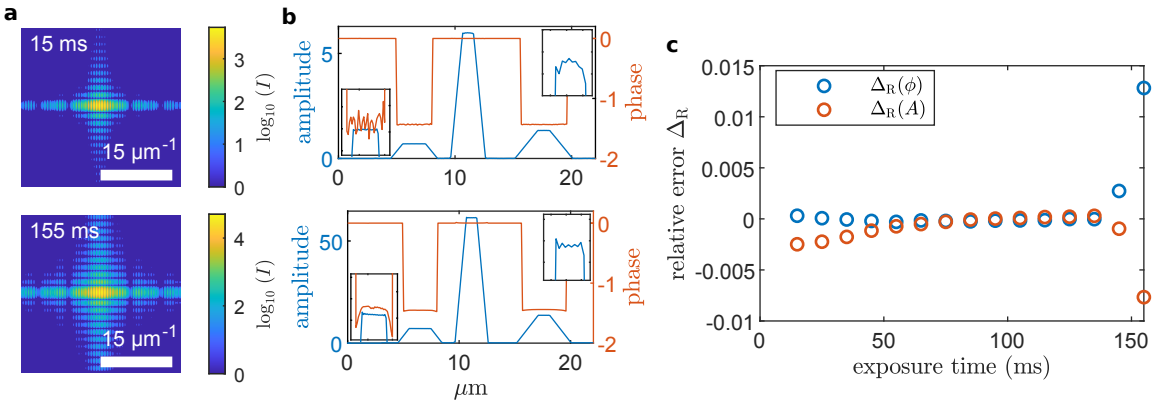

Figure 5.5: Simulation of triple slit scattering with varying exposure times (photonflux 5×10^{11} photons/s, sample-CCD distance 0.125 m). **a** Zoomed-in (2x) scattering images of triple slits for 15 ms and 155 ms exposure time plotted in logarithmic scale. **b** Center slice thorough cross-correlations of the three slits. The cross-correlations are described in the caption of Fig. 5.4. The inset in the lower left (upper right) displays a 20 times scaled region of the left (middle) plateau. The upper (lower) panel corresponds to the 15 ms (155 ms) scattering pattern on the left in **a**. **c** Relative error of reconstructed phase shift and transmission amplitude to ground truth as a function of exposure times.

5.3 Exposure Time and Random Noise

In this section, we are looking at the effects of different CCD exposure times on the reconstructed signal. Furthermore, the effects of random noise sources (shot noise and read out noise) will be investigated.

For the calculation of the exposure times, the photon flux of the XUV source was set to 5×10^{11} photons/s which is comparable to the experiments with the synchrotron radiation. In general, the exposure time influences the maximum measurable scattering angle and consequently the shape of the plateaus of the cross-corrections.

Figure 5.5c shows the relative error of the normalized amplitude and the relative error of the phase of the cross-correlation c_{12}. In Fig. 5.5a, two selected scattering patterns (for 15 ms and 155 ms) are shown, with the corresponding cross-correlation displayed in Fig. 5.5b.

As is expected and can be seen see from Fig. 5.5a, shorter exposure times mean less intensity detected at higher diffraction angles. If we examine the example of low exposure in Fig. 5.5b (15 ms), the noise on the phase plateau is stronger than on the amplitude plateau. The noise stems from the stronger intensity cut-off[5] in the scattering pattern, increasing the areas of zero intensity around the destructive interference. The relative error of the phase in Fig. 5.5c is less influenced by the noise on the plateau because the values of the plateau gets averaged for the reconstruction. As in the last section, the normalized amplitude's relative error is more affected by the noise due to the noise contributions of both the material-reference cross-correlation and the normalization cross-correlation.

[5]Only simulated photon events ≥ 1 are counted in this simulation

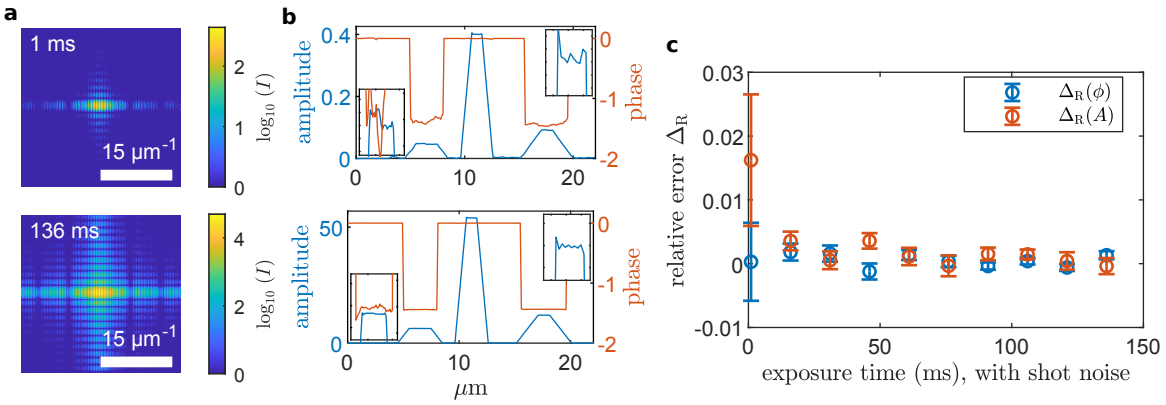

Figure 5.6: Simulation of triple slit scattering with shot noise and varying exposure times. The data points are averaged over 10 different simulations (photonflux 5×10^{11} photons/s, sample-CCD distance 0.125 m). **a** Zoomed-in (2x) scattering images of triple slits for 1 ms and 136 ms exposure time plotted in logarithmic scale. **b** Center slice thorough cross-correlations of the three slits. The cross-correlations are described in the caption of Fig. 5.4. The inset in the lower left (upper right) displays a 20 times scaled region of the left (middle) plateau. The upper (lower) panel corresponds to the 1 ms (136 ms) scattering pattern on the left in **a**. **c** Relative error of reconstructed phase shift and transmission amplitude to ground truth as function of exposure times.

For exposure times >140 ms, the relative error diverges. Here, the CCD begins to saturate. The reconstruction is very sensitive to this error. Just a few oversaturated pixels in the center of the diffraction pattern will lead to a disturbed reconstruction. The multiplicative function, which degenerates the true diffraction pattern into the saturated one, will lead to a convolution with an ariy-like pattern in real space. This error can be corrected in Fourier space through inpainting of the oversaturated areas (not shown).

For a XUV source with 5×10^{11} photons/s, even an exposure time of 15 ms leads to acceptable values with only 2 % relative error. During our HHG experiment, the photon flux behind the sample was more likely to be in the order of 1×10^{8} photons/s (see Ch. 3.2). An acceptable exposure time would thus be in the order of 10 s.

For the last simulation, the probability that a photon was detected was equal to one within the intensity cut-off determined by the exposure time. Next, we are investigating the effect of shot noise, following the Poisson distribution, on reconstructions with different exposure times. For the shot noise simulation, the shot noise generator from [75] was used. The relative errors in Fig. 5.6c were averaged over 10 runs each. The error bars indicate the standard deviation of this average. As before with lower exposure times, when the destructive interference minima were not measured smoothly, the relative error diverges. The influence of the Poisson noise can be seen from the noise on the cross-correlation plateaus. However, compared to the the noise-free data from Fig. 5.5, the average of the values of the correlation plateaus is only affected slightly by the Poisson noise distribution in the Fourier plane.

We now introduce Gaussian noise to the background to simulate the readout noise of

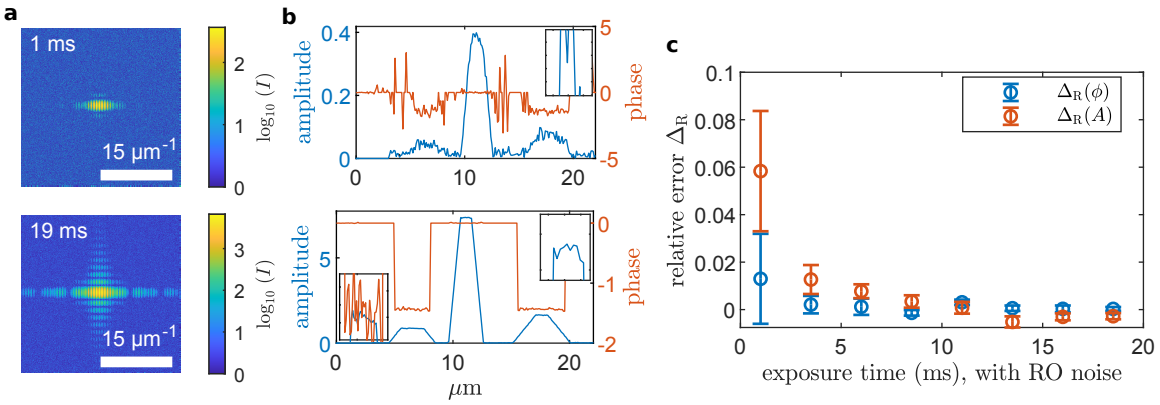

Figure 5.7: Simulation of triple slit scattering with readout noise and varying exposure times. The data points are averaged over 10 different simulations (photonflux 5×10^{11} photons/s, sample-CCD distance 0.125 m). **a** Zoomed-in (2x) scattering images of triple slits for 1 ms and 19 ms exposure time plotted in logarithmic scale. **b** Center slice thorough cross-correlations of the three slits. The cross-correlations are described in the caption of Fig. 5.4. The inset in the lower left (upper right) displays a 20 times scaled region of the left (middle) plateau. The upper (lower) panel corresponds to the 1 ms (19 ms) scattering pattern on the left in **a**. **c** Relative error of reconstructed phase shift and transmission amplitude to ground truth as function of exposure times.

the CCD ($\sigma = 15$ counts), which is comparable to the Gaussian noise from the experiment. The data points in Fig. 5.7c are averaged over 10 different runs. The error bars indicate the standard deviation of this average. Even though the noise on the correlation plateaus appears stronger than before (Fig. 5.7b), the evenly distributed Gaussian noise can be mostly averaged out in the reconstruction. Compared to the shot noise simulation at 1 ms, the effect of the read out noise has a stronger impact on the relative error. We attribute this to the disturbance of the destructive interference minima by the read-out noise.

CHAPTER 6

Time-Resolved Measurements

This section presents the first time-resolved measurements using the triple slit interferometric method. In Ch. 4, we demonstrated the capability of our method to simultaneously measure spectroscopic self-normalized amplitude and phase changes of Co, Fe and Gd. In this chapter, we will apply this capability to study the dynamics of the real and imaginary part of the magneto-optical index of Fe at the M-edge after excitation with a femtosecond 800 nm-laser.

Previous techniques aiming to investigate the temporal dynamics of the magnetic circular dichroism include femtosecond slicing at the synchrotron facility BESSY II [76] and femtosecond IR-pump/XUV-probe experiments on HHG sources [3, 77]. Both techniques access only the absorptive part of the refractive index. To our knowledge, our triple slit method is the first to simultaneously access both the dispersive and the absorptive part of the refractive index with temporal resolution in the femtosecond regime.

We performed our study with XUV light from a HHG source which offered a time resolution of approximately 50 fs. The photon energy range of the HHG source from 40 to 72 eV covered the M-edges from the $3d$ transition-metals. The properties of the generation of the higher harmonics, the experimental setup, and the sample geometry are described in more detail in Ch. 3.2 and in [46].

Figure 6.1 shows a schematic overview of the pump-probe experiment. A spherical multilayer mirror focussed the circularly polarized XUV-light from the HHG source onto the $Gd_{28}Fe_{72}$ sample. The mirror had a maximum reflectivity at 54.3 eV to select the 35^{th} harmonic. To minimize astigmatism, the angle between incoming and outgoing XUV was made as small as possible. The sample was magnetized out-of-pane and was mounted in normal incidence transmission geometry. The electromagnet was able to saturate the sample in both directions with up to maximal 250 mT. The CCD was placed 75 mm behind the sample. The IR-pump was reflected by a flat mirror onto the sample (angle IR-pump/XUV-probe: 9°). A 200 nm Al-filter covered the CCD from stray IR-light.

In the next section, we show a small-angle scattering experiment demonstrating the capability of our setup to measure time resolved demagnetization in a pump-probe configuration. Afterwards, we show the dynamics of the magnetic asymmetry as measured

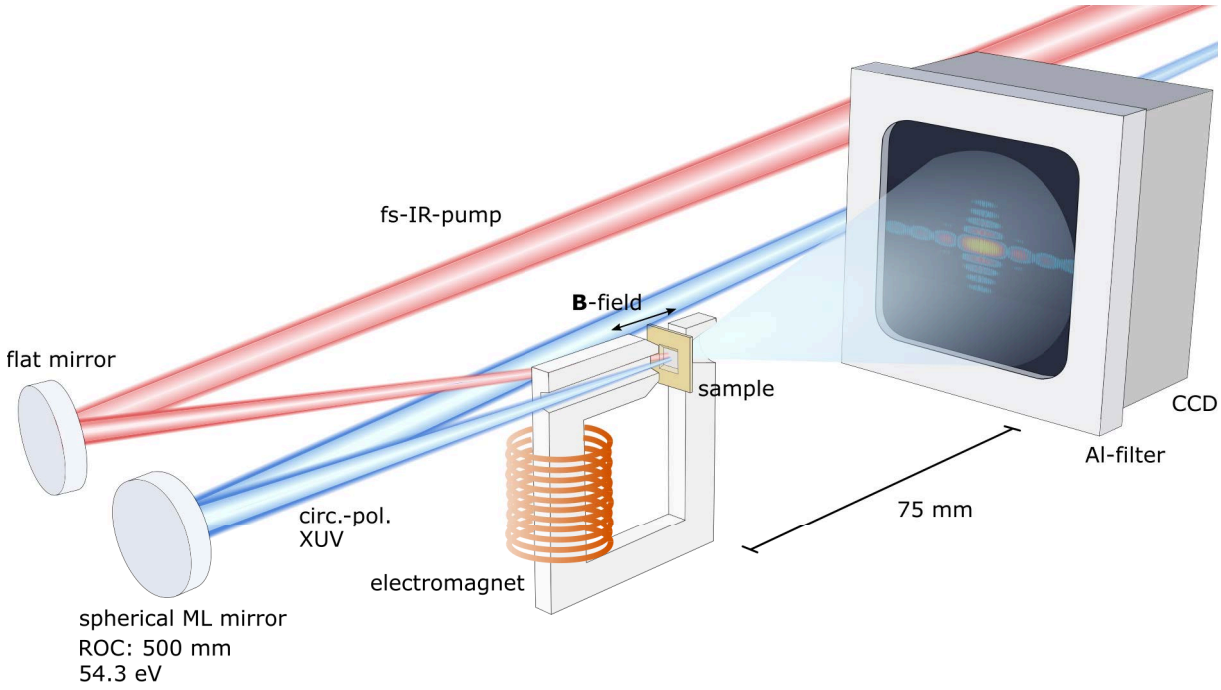

Figure 6.1: Triple slit transmission geometry for IR-pump and XUV-probe experiment. The $Gd_{28}Fe_{72}$ sample was magnetized out-of-plane. The electromagnet was able to saturate the sample magnetization in both directions with maximal 250 mT. Circularly polarized HHG light was used. The spherical mirror was selective for the harmonic at 54.3 eV and focused the XUV beam to the sample plane. The CCD was placed 75 mm behind the sample. A 200 nm Al-filter covered the CCD to block the stray light from the IR-pump beam.

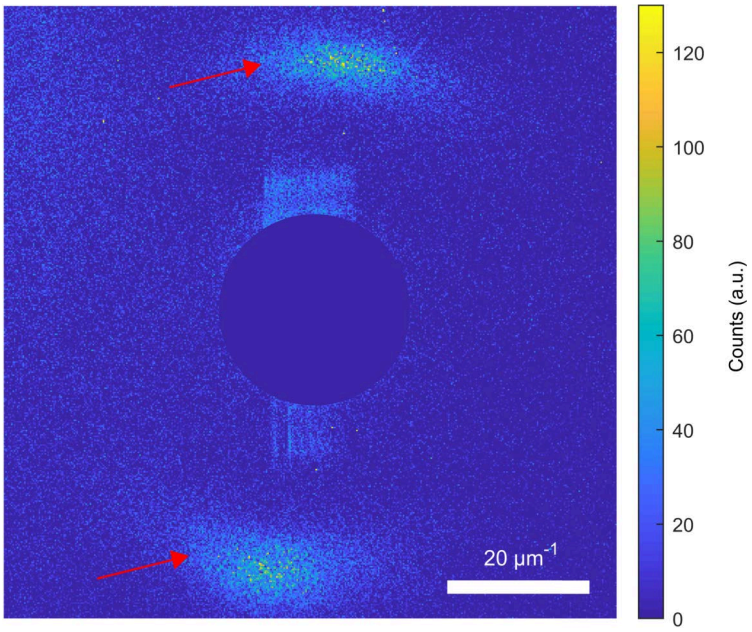

Figure 6.2: Small-angle resonant scattering from a $[\mathrm{Co}(8)/\mathrm{Pt}(8)]_{\times 16}$ multilayer. The domains were approximately horizontally aligned. The photons were circularly polarized and had an energy of 60.5 eV. The center part containing the shadow of the beamstop wire and parts of the direct beam is masked out by a circular disk. The first-order diffraction of the magnetic stripe domains is marked by red arrows.

by our triple slit experiment, followed by a discussion of the results.

6.1 Time-Resolved Small-Angle Scattering of Magnetic Domains

Before we present the time-resolved triple-slit data, we tested the performance of our experimental pump-probe setup by measuring the IR-laser-induced ultrafast demagnetization of a $[\mathrm{Co}(8)/\mathrm{Pt}(8)]_{\times 16}$ multilayer in a small-angle scattering experiment. This experiment itself is similar to the one published in [78]. The multilayer was deposited on a silicon nitride membrane by magnetron sputtering. The multilayer exhibits a perpendicular magnetic anisotropy which supports the formation of a nanoscale domain pattern of alternating magnetization direction. With a photon energy close to the Co M-edge resonance, the photoabsorbtion on the domains leads to a ring-like intensity distribution on the CCD. To maximize the SNR on the CCD, we prepared the domain structure into aligned stripes by an in-plane demagnetization routine. The diffraction of the aligned stripe domains will be concentrated into two first-order diffraction peaks. The intensity $I(\boldsymbol{q})$ of those areas is proportional to $|(\mathcal{F}M)(\boldsymbol{q})|^2$ with the operator of the Fourier transformation $\mathcal{F}$, the function of the magnetization of the sample M, and the reciprocal vector $\boldsymbol{q}$. The distance of the diffraction peaks from the center is reciprocal connected to the spacing of the domain lattice.

For scattering in resonance with the Co M-edge, we used a spherical multilayer mirror

with reflection maxima at 60.80 eV. We blocked the intense zero order with a narrow strip of aluminium to prevent CCD saturation. The beamblock was mounted and moved vertically by a stepper motor for alignment. Beyond these changes, the experimental setup did not need any modification compared to the triple slit setup. Specifically, it has the same time resolution of approximately 50 fs.

Fig. 6.2 shows a typical background corrected diffraction pattern before time zero. The slight unevenness in the background originates from intensity fluctuations from the IR pump laser, which were not completely filtered by the Al-filter in front of the CCD. From the position of the first-order diffraction, a domain periodicity of 180 nm can be derived.

We integrated the intensity in the first diffraction order radial and azimuthal for every time delay of the pump beam. While the position of the diffraction peaks displays no measurable change, indicating a recovery of the domain pattern with the same spatial statistical properties, the intensity decreased noticeable during the first 60 fs after the IR excitation (Fig. 6.3), indicating a transient reduction of the domain magnetization.

Figure 6.3 shows the ultrafast time evolution of the normalized magnetization M/M_0 for three pump fluences (4.0 mJ cm^{-2}, 7.5 mJ cm^{-2} and 9.9 mJ cm^{-2}). The magnetization M was calculated by the square root of the integrated intensity values and normalized to the unpumped magnetization M_0 during negative delay times. The data points were fitted by a double exponential fit:

$$\frac{M}{M_0} = G(t) * H(t) \left[A_0 t - \frac{(\tau_2 A_1 - \tau_1 A_2)\mathrm{e}^{-t/\tau_1} + \tau_2(A_2 - A_1)\mathrm{e}^{-t/\tau_2}}{\tau_2 - \tau_1} \right] \tag{6.1}$$

with a Gaussian $G(t)$ to account for finite temporal resolution, the Heaviside step function $H(t)$, the amplitudes of the exponentials A_n, and the time constants for de- and remagnetization τ_1 and τ_2. For every measured fluence, the characteristic demagnetization time τ_1 is in the range of 64 fs to 74 fs. For the highest fluence (9.9 mJ cm^{-2}), the relative magnetization decreases to 34 %. The ultra-fast demagnetization is followed by a slower recovery.

Table 6.1 shows the characteristic fit parameters for every fluences. The time constant for 4.0 mJ cm^{-2} was averaged over four measurements. Both other fluences were only measured one time, which explains the larger error. It should be noted that the SNR of this measurement depends on the number of photons recorded on the CCD. For lower magnetic scattering contrast, e.g., for stronger demagnetisation (9.9 mJ cm^{-2}, > 0.15 ps), fewer photons are scattered and, therefore, the SNR becomes unfavourable.

The Co demagnetization times found in this experiment are shorter compared to the dynamic HHG scattering experiment published in [78]. This can be explained by the different sample compositions. In [78], a Co/Pd multilayer was used. In our sample, the multilayer consists of Co/Pt. The enhancement of the demagnetization by Pt was observed and explained in recent literature by higher spin-orbit coupling [79]. With this experiment, we demonstrated the general capability of our setup to successfully perform pump-probe measurements of demagnetization dynamics with a temporal resolution of approximately 50 fs.

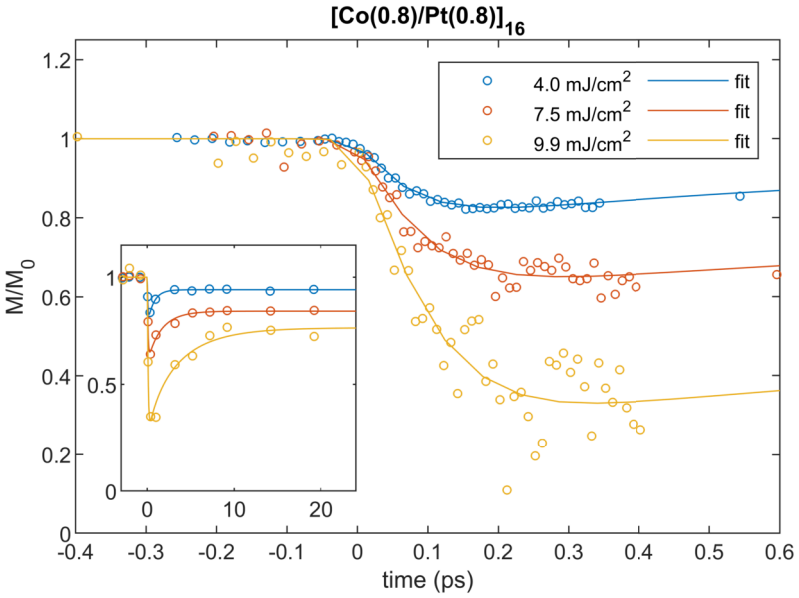

Figure 6.3: Fluence series of the normalized ultra-fast demagnetization of $[Co(8)/Pt(8)]_{\times 16}$ multilayer after fs-IR laser excitation derived from the small-angle scattering data. The inset shows the remagnetization for longer ps-range. The solid lines represent the best two-exponential fits through the data. The fit parameters are shown in Tab. 6.1.

Table 6.1: Characteristic fit parameters for ultra-fast demagnetization caused by different pump fluences. τ_1 and τ_2 are fitting parameters of the double exponential fit and are connected to the demagnetization and remagnetization times.

Fluence ($mJ\,cm^{-2}$)	min. rel. MCD (%)	τ_1 (fs)	τ_2 (ps)
4.0	0.83	64 ± 5	0.76 ± 0.07
7.6	0.65	74 ± 10	1.72 ± 0.48
9.9	0.34	69 ± 10	4.26 ± 1.49

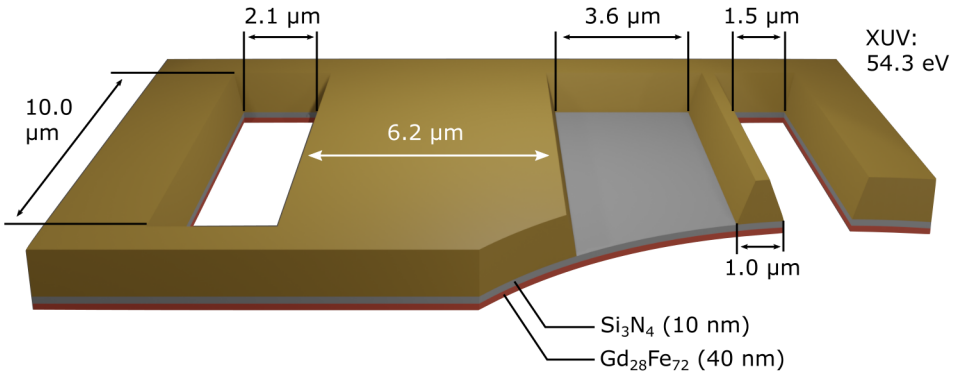

Figure 6.4: Cutaway drawing for the triple slit geometry used in the HHG pump-probe experiment. To account for the lower intensity of the HHG source compared to the synchrotron source used in the static measurements, the slits height was increased to 10 µm. Compared to the triple-slit geometry from the static measurement (Fig. 4.2), the material slit position was switched with one reference slit to allow better performance in combination with the longitudinal coherence of the HHG source. The sample was seeded and capped with 3 nm Ta (not shown) and masked with 1 µm Au.

6.2 Sample Layout

The triple slit layout for the HHG pump-probe experiment is shown schematically in Fig. 6.4. We used a 40 nm Ta(3)/$Gd_{28}Fe_{72}$(40)/Ta(3) layer for the pump-probe experiment. We adjusted the geometry of the slits to account for the different beam properties compared to the synchrotron experiments. Compared to the synchrotron experiment, the photon flux at the HHG source is lower by approximately three orders of magnitude (s. Ch. 3.2). It is, therefore, important to get as much interaction as possible from the cross section of the HHG radiation with the slits to achieve reasonable CCD exposure times. This goal has to be balanced with the necessary approximation that the incident wave has to be a plane wave over the sample area. Beam vibrations and long term beam drift also make the use of a small focus on the slits less beneficial. These instabilities can be countered by a larger focal beam spot on the sample. We found that a slit height of 10 µm and a beam diameter of 80 µm are a good compromise. The beam size ensures that small spatial vibrations orthogonal to the slit's height have reduced impact on the transmission through the slits, while the slit height optimizes the transmitted signal. The long term beam drift, on the other hand, has to be corrected after approximately every one hour of measuring, by aligning the sample back into the beam.

Another challenge of the HHG experiment is the inhomogeneity of the XUV beam profile. Imperfections in the optics and the non-linear HHG process add up to random fluctuations of the curvature of the XUV beam profile. Every phase difference greater than zero in the incident beam at the position of the individual slits cannot be distinguished from a phase shift caused by an interaction with the sample. This problem only becomes relevant for the XMCD difference measurement, when the vibrational and drift instabilities occur on faster time scales than two exposure times. To manage this problem, we, first, aimed at fast exposure times in expanse for higher SNR and, second, rearranged the

position of the slits. Specifically, we exchanged one vacuum slit with the material slit from the previous slit geometry and reduced their distance. The closer the material slit is to the neighbouring vacuum slit, the lower the impact of a incident wave deviation from a plane wave is on the data analysis. In the case of this geometry, the auto-correlation and the cross-correlation between the right vacuum slit and the material slit are not completely separated. For the reconstruction, we only used the separated part. Functioning as a control experiment, we analysed the reconstruction from the vacuum slit, which is further away from the material slit.

To further optimize the transmission through the sample, we changed the thickness of the Si_3N_4 membrane from 30 nm to 10 nm, which increased the transmission through this layer from approximately 50 % to 80 %. Additionally, we increased the $Gd_{28}Fe_{72}$ layer to 40 nm to enhance the magnetic signal. Another benefit of the $Gd_{28}Fe_{72}$ alloy was the fact that it can be driven into full saturation with an external field of 50 mT (see Ch. 3.1.4), which reduced the heat load from the electro-magnet in the vicinity of the sample.

6.3 Pump-Probe Measurement on the Fe M-Edge

This section presents the first time-resolved triple-slit experiment. The dynamics of the relative magnetic asymmetry of Fe after optical excitation with a 800 nm laser pulse are derived from the difference of the relative transmission and phase shift between the two out-of-plane magnetic saturation states of a $Gd_{28}Fe_{72}$ layer. The measured time-resolved data are compared to simulated data. As for the pump-probe small-angle scattering experiment from Ch. 6.1, the temporal resolution was approximately 50 fs. As probe, the harmonic at 54.3 eV, resonant to the Fe M-edge, was selected by a spherical multilayer from the HHG spectrum. The sample was pumped with 800 nm radiation at a fluence of $12\,\mathrm{mJ\,cm^{-2}}$. The experimental details are described in Ch. 3.2 and Ch. 3.3.

A center section from a typical background corrected diffraction pattern from $t < 0$ is shown normalized in logarithmic scale in Fig. 6.5b and compared to a simulated diffraction pattern (Fig. 6.5a). The geometry for the simulated slits was taken from a scanning electron microscope (SEM) image of the triple-slit sample. The magneto-optical constants for the simulated 40 nm $Gd_{28}Fe_{72}$ sample layer were taken from the equilibrium results from Ch. 4.3.1. We attribute the slight vertical shear distortion of the measured diffraction pattern (Fig. 6.5b) to the invalidity of the plane wave approximation during the HHG measurement. On the right side of the background in 6.5b, a larger area with lower intensity is visible. The sensitivity of these pixels was reduced, caused by a previous unwanted IR beam exposure. However, this has no major impact on the analysis of the data, as the reduced sensitivity is small, the periodicity of the triple-slit diffraction is not changed by it, and the area of less sensitive pixels is not changing the intensity of the zero-order diffraction. In the background of the simulated diffraction pattern, vertical lines are visible. These lines are an artefact of the shot noise generator only noticeable in the logarithmic scaling.

The upper panel of Fig. 6.6 shows the relative transmission through the $Gd_{28}Fe_{72}$ slit for both out-of-plane magnetization directions, extracted from interference pattern such as in Fig. 6.5b, recorded as a function of pump-probe delay. The corresponding scattering pattern of an individual data point took an exposure time between 20 s and

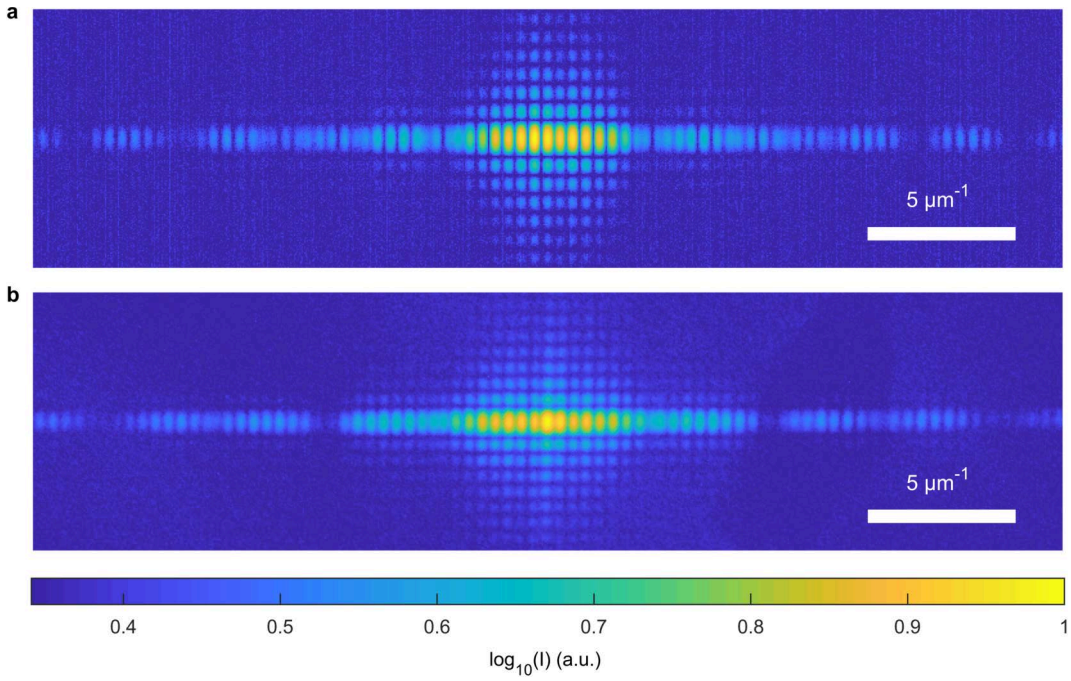

Figure 6.5: Comparison of a simulated (**a**) and measured (**b**) diffraction pattern produced by the $Gd_{28}Fe_{72}$ triple-slit sample geometry at the Fe M-edge (54.3 eV) in log-scale. The simulation used shot noise and read-out noise. We attribute the differences between **a** and **b** to the invalidity of the plane wave approximation during the HHG measurement.

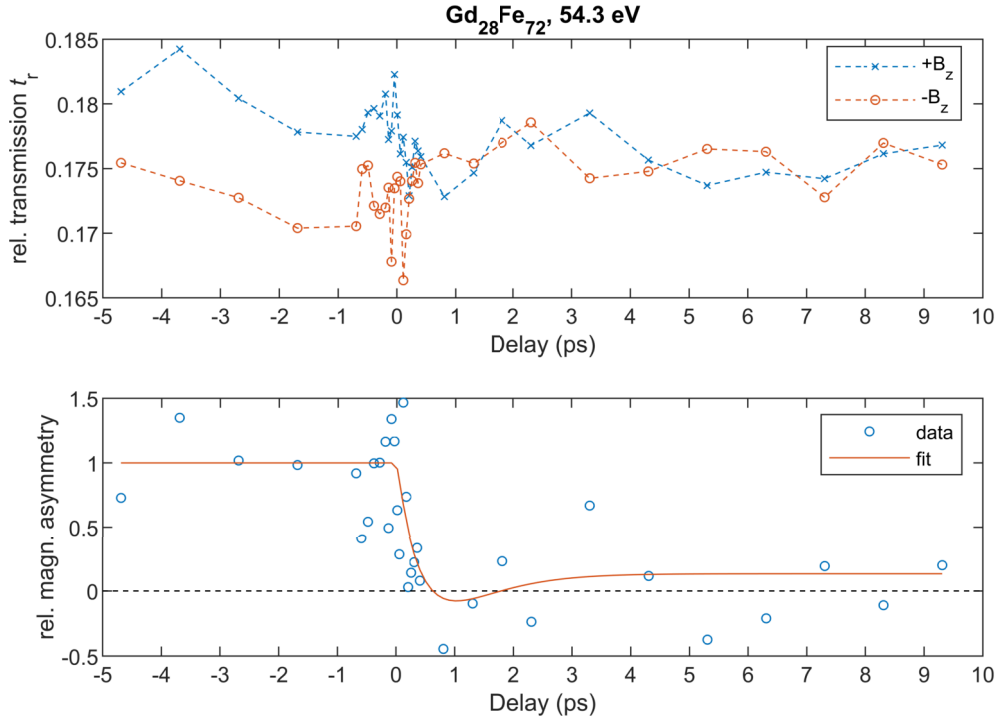

Figure 6.6: Measured transient relative transmission of $Gd_{28}Fe_{72}$ at 54.3 eV for both magnetic saturation directions after excitation with a fs-IR laser (upper panel). The lower panel shows the relative magnetic asymmetry and the corresponding two-exponential fit.

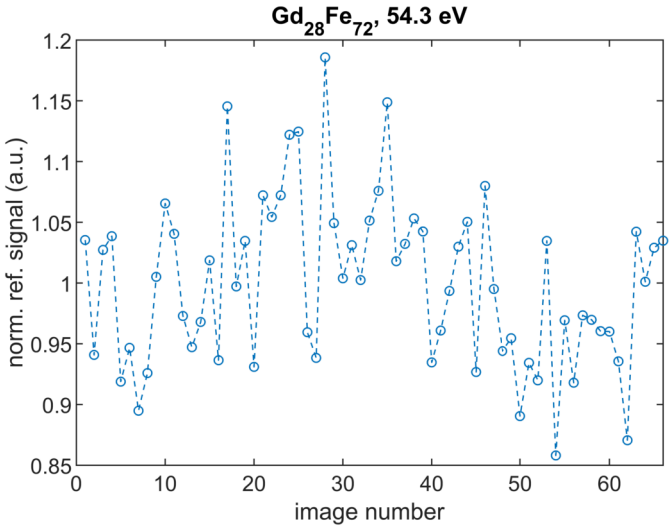

Figure 6.7: Reference cross-correlation normalized to its average. The reference cross-correlation was used for the normalization of the transmission of the $Gd_{28}Fe_{72}$ slit.

30 s depending on the performance of the HHG source at the respective time. The transmission is normalized to the intensity transmitted through the reference slits, and, therefore, normalized to the intensity of the incoming beam. The normalized reference signal is shown in Fig. 6.7. The standard deviation of the average value is 0.07. This demonstrates the importance of a reliable normalization signal when using a fluctuating source like a HHG source, as it would otherwise be impossible to measure changes to the demagnetization on the order of 2 % or less of the signal. The slower trend visible in the normalization signal in Fig. 6.7 originates from beam drifts over the sample area, while the faster fluctuations arise from intensity fluctuations of the XUV probe.

We define the magnetic asymmetry a as

$$a = \frac{S_p - S_m}{S_p + S_m}, \tag{6.2}$$

with S_i: signal for the magnetic saturation direction i. This quantity expresses the percentage of the magnetization dependent part of the transmission.

The measured magnetic asymmetry in the equilibrium state before time zero equals 2 %. This is below the maximum possible magnetic asymmetry (3.4 %) of the $Gd_{28}Fe_{72}$ sample, as the probe beam had not perfect circular polarization. The degree of circular polarization produced by the phase shifter was expected to be between 70 % and 80 %. Therefore, the MCD contrast is reduced by the same amount.

The relative magnetic asymmetry[1] of both magnetization directions is plotted in the lower part of Fig. 6.6. The fit of the data serves as guide to the eye.

Within the first picosecond, the relative magnetic asymmetry drops to zero and does not recover in the observed time delay window of 10 ps within the statistical error. Unfortunately, the SNR of our measurement is too low to make a quantitative statement about the demagnetization time. Probe vibration, long term probe drift and intensity

[1]The relative magnetic asymmetry equals the magnetic asymmetry normalized to the average value of the magnetic asymmetry before $t = 0$.

fluctuations of the HHG process may not be a problem for such experiments, in which the whole beam is transmitted through the sample and therefore the beam instabilities are averaged out, such as the time-resolved small-angle scattering experiment presented in Ch. 6.1. In the pump-probe experiment using the triple-slit mask, however, where the sample apertures are much smaller than the beam, the local beam properties play a much greater role.

Figure 6.8a shows six normalized 25 ms long CCD exposures of the direct beam on the detector position. In Fig. 6.8b, the horizontal and vertical linescans through the maximum of each exposure are shown. It is apparent that in the time frame of this observation the direct beam has two predominant intensity modes, which both appear at a different spatial position. The intensity of one mode is reduced by 24 % compared to the other, while the beam position of the lower intensity mode is laterally shifted by about 10 % to the higher intensity mode. The intensity fluctuations would average out over the longer exposures of the triple slit measurements and, beyond that, could be corrected by the inherent reference signal of the vacuum slits. The positional fluctuations of the beam are a more serious source of error. Short-term positional fluctuation would lower the visibility of the interference pattern in the exposures, while long-term fluctuations would alter the local phase and amplitude curvature of the beam. As the FWHM beam size at the sample plane was 80 µm, positional fluctuations of up to 10 % of the beam FWHM are an important source of error for a sample with an aperture size in the order of 10 µm. Based on the model presented in Ch. 5.1, we estimate that for the employed experimental geometry a lateral beam shift of 8 µm between two corresponding exposures would cause in the worst case[2] an error to the relative magnetic asymmetry of the relative transmission of up to 80 %. We note that the beam fluctuations observed from Fig. 6.8 are happening on a shorter time compared to the exposure time (fluctuation: 4 s, exposure time: 30 s). The maximum beam shift error will only be caused when the beam is stable for one exposure and shifts to the other mode for the next exposure. To improve this aspect of the experiment, one could either refine the beam stabilization of the HHG process or enhance the intensity of the HHG source to allow a larger beam profile on the sample, where local curvature would have a lower impact on the experiment.

The reconstructed phase shifts of the XUV beam passing through the $Gd_{28}Fe_{72}$ layer as a function of pump-probe time delay are shown for both out-of-plane magnetization directions in the upper panel of Fig. 6.9. The lower panel of Fig. 6.9 shows the normalized magnetic asymmetry of the phase shift. The phase reconstruction was significantly more challenging compared to the amplitude reconstruction. Instead of our normal reconstruction scheme, we used a correction term to deal with linear phase differences in the incident wave front, as we will explain in the following.

In a pump-probe experiment that satisfies the plane wave approximation, the phase difference between both vacuum slits would be constant over all time delays. In our experiment, this phase difference was varying from exposure to exposure, indicating an unstable phase curvature of the incident beam at the sample position. Up until now, we only used the amplitude of the cross-correlation of both vacuum slits as normalization.

[2]This error depends on the change of amplitude gradient and phase gradient from the incident wave at the position of the slits. The worst case error will occur when the maximum of the Gaussian beam falls between the material slit and the adjacent reference slit for one exposure (lower gradient), and for the second exposure, both slits are illuminated by one side of the Gaussian beam (higher gradient).

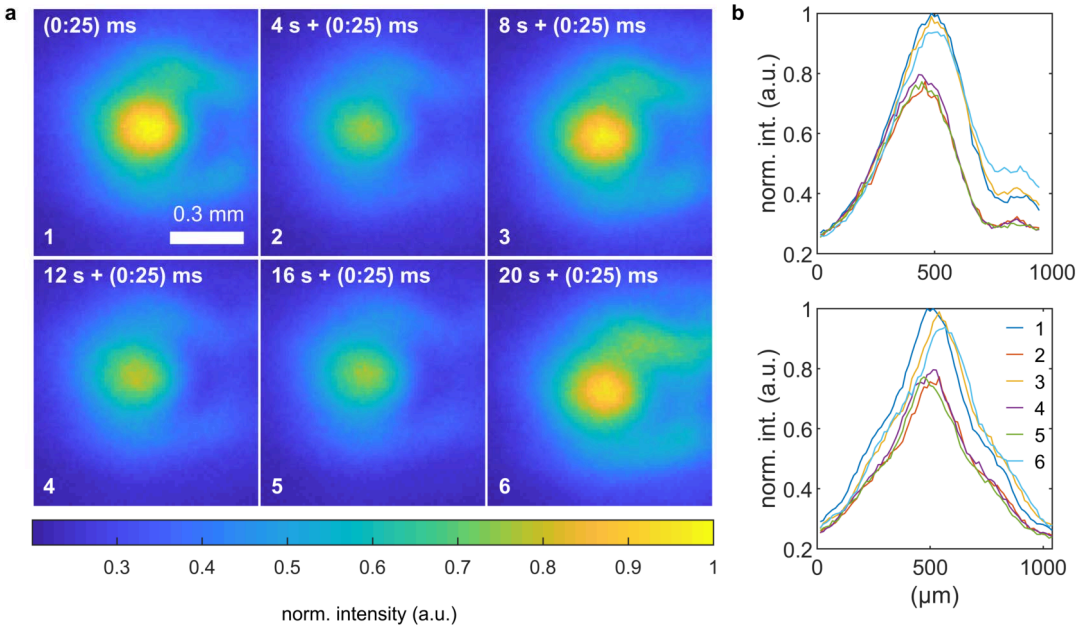

Figure 6.8: Intensity changes and positional fluctuations of the HHG direct beam at the detector plane. **a** Series of short CCD exposures (25 ms) of the direct beam. The readout time was 4 s. The exposure time is displayed in addition to the total time of the time series at the top of each image. **b** Top (bottom) graph shows horizontal (vertical) line scan through the maximum of each exposure from **a**. The numbers in the legend correspond to the positions of the images in the time series in **a**.

The phase of the cross-correlation of both vacuum slits is zero for an incident plane wave and non-zero for any deviation from a plane wave. For the case of the XUV probe beam, the non-zero phase of the cross-correlation of both vacuum slits provide a linear phase ramp approximation for phase curvature incident on the area of both vacuum slits.

The advantage of the geometry we introduced in this chapter is that the material slit and one vacuum slit are close together. This leads to the fact that the linear phase approximation between the two vacuum slits is approximately the same as between the material slit and the vacuum slit further away (see Fig. 6.4 for overview over the sample geometry). Thus, the corrected difference of the relative phase shifts for both magnetization directions $\Delta\phi^{\mathrm{corr}}$ was calculated by:

$$\Delta\phi^{\mathrm{corr}} = \Delta\phi - \Delta\phi_{\mathrm{ref}}, \tag{6.3}$$

with the uncorrected phase shift difference between both saturation magnetization states $\Delta\phi$ and, correspondingly, the difference between the relative phases of both reference slits $\Delta\phi_{\mathrm{ref}}$ as approximation for the phase curvature. Similarly, the corrected relative phase ϕ_i^{corr} between material and vacuum slit for a single magnetic saturation state of the sample was calculated by:

$$\phi_i^{\mathrm{corr}} = \phi_i - \phi_i^{\mathrm{ref}}, \tag{6.4}$$

with the uncorrected phase shift ϕ_i and the linear phase curvature approximation between both reference slits ϕ_i^{ref}. The index i stands for one of the two magnetization states.

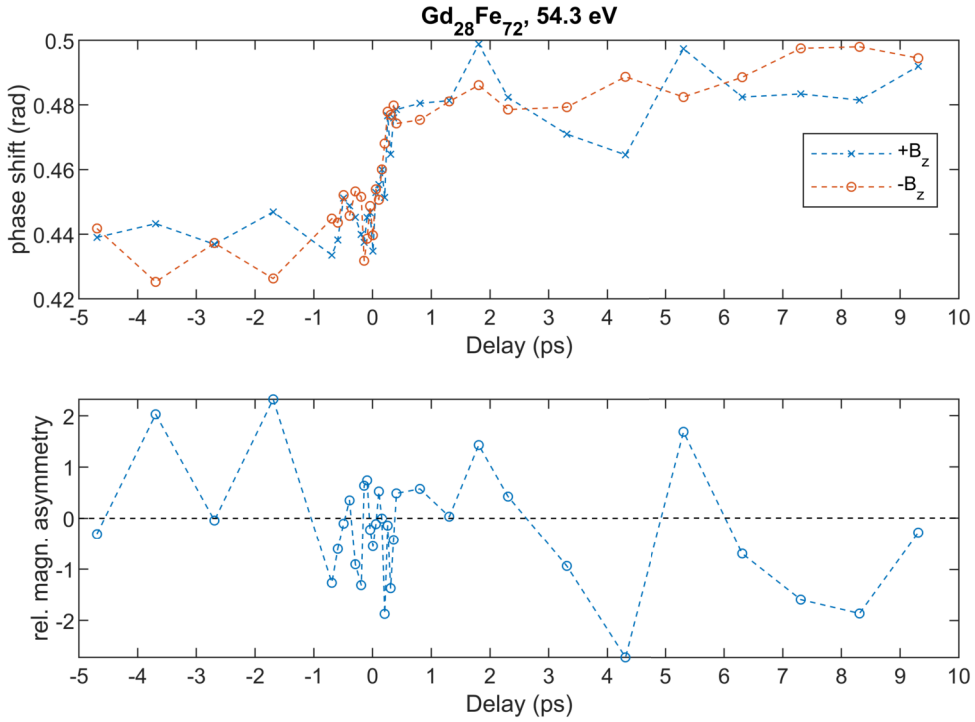

Figure 6.9: Measured transient relative phase of $Gd_{28}Fe_{72}$ at 54.3 eV for both magnetic saturation directions after excitation with a fs-IR laser (upper panel). The lower panel shows the relative difference of both signals. The phase shifts were corrected by a linear phase ramp.

The phase shifts for both magnetic saturation directions that are shown in the upper panel of Fig. 6.9 as a function of pump delay were corrected by the linear phase ramp. Both exhibit a steep jump of around 0.04 rad at time zero. This response of the sample is not connected to the optically induced ultrafast demagnetization, as there is no such behaviour visible in the relative difference between both magnetization states (lower panel of Fig. 6.9). The changes of the phase shift happen in the first 300 fs after the IR-pump excitation. This time delay interval has the highest density of sampling points. If plotted with equal spacing, the phase shift shows a constant drift as a function of the exposure time (data not shown). We attribute the constant phase shift to a drift between sample and XUV beam, which changes the phase gradient of the incident wave and which could not be corrected by the linear phase correction term in Eq. 6.4. Further investigation is necessary to determine the contribution to the phase jump at time zero due to changes in the electronic structure of the sample layer, e.g. due to heating.

In the lower panel of Fig. 6.9, the relative difference of the phase shifts for both magnetization directions is shown. The signal is too small to gain any insight into the temporal behaviour of the demagnetization.

To investigate why the SNR in the relative phase difference measurement is significantly lower than in the amplitude difference, we simulated the diffraction pattern for the different time delays (see Fig. 6.5 for comparison of the simulated and measured diffraction pattern), based on the assumption that the change of relative transmission and phase shift is caused by the change in magnetization induced by the IR laser pulse. The triple slit geometry for the simulation was taken from an SEM image of the sample. We used shot noise and read-out noise on the simulated diffraction pattern. The dynamic range of the CCD and the CCD's quantum efficiency were included. The magneto-optical constants for the $Gd_{28}Fe_{72}$ sample layer were taken from the results measured in equilibrium at the synchrotron source (Ch. 4.3.1). The simulated MCD was lowered, to account for a lower degree of ellipticity. The simulated photon energy was 54.3 eV. The dynamics of the magnetic contrast were taken from the fitted curve from the lower part of Fig. 6.6. We used a plane wave as illumination of the sample.

Figure 6.10 shows the simulated dynamics of the relative transmission based on demagnetization. The average value of the transmission is larger in the simulation than in the experiment (compare Fig. 6.10 and Fig. 6.6). This difference is most likely caused by a different layer height of the supporting silicon nitride membrane in the simulation compared to the experiment, as all other sample layers were known with sufficient accuracy. The transmission offset of the simulated sample has no effect on the difference signal. The standard deviation of the simulated values of the relative transmission is $\sigma = 0.17$ and for the measured data $\sigma = 0.31$. The difference between the standard deviation of the simulated data and the measured data can be used to estimate the error caused by beam drift. As the simulation only used read-out noise and shot noise as error sources, the standard deviation of the simulated relative transmission is fully based on both error sources. We attribute the difference between the standard deviation of simulated and measured data to the errors caused by beam drift.

The simulated demagnetization dynamics of the relative phase are shown in Fig. 6.11. As for the transmission, the absolute values do not match the experiment due to a likely different height of the non-magnetic layers in the sample, which does not affect the magnetic contrast. The lower panel of Fig. 6.11 shows the relative difference of the relative

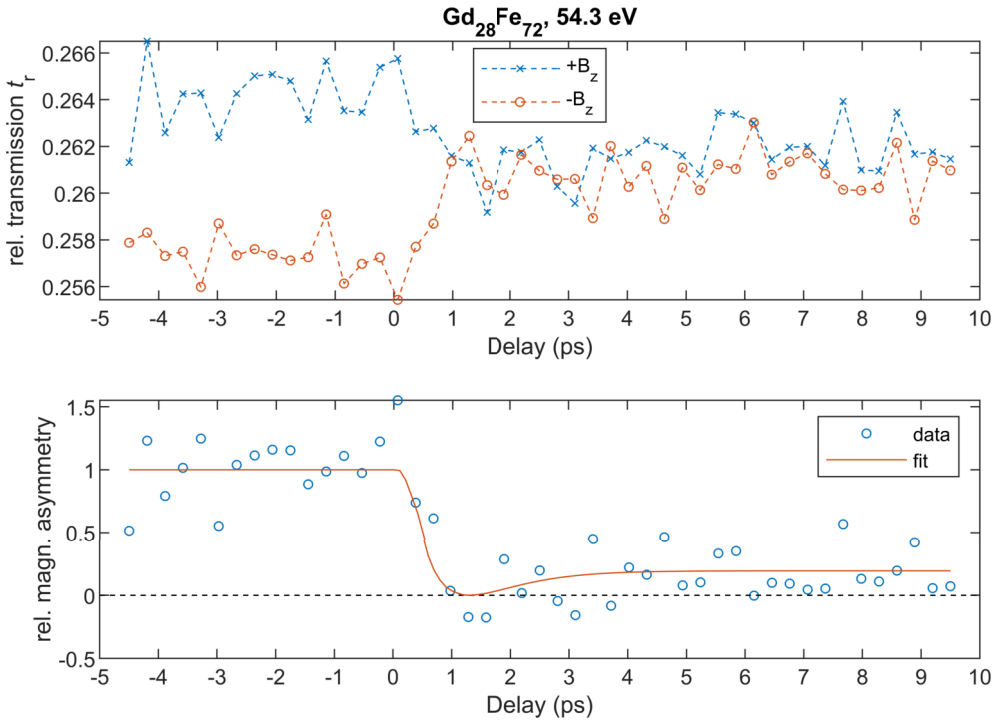

Figure 6.10: Simulated transient change of the relative transmission of $Gd_{28}Fe_{72}$ at 53.4 eV for both magnetic saturation directions (upper panel). For the simulated time dependency, the fit to the measured data from Fig. 6.6 was used. A single simulated diffraction pattern used for this analysis is shown in Fig. 6.5. In the lower panel, the relative magnetic asymmetry of the simulated data is shown with its correspondent double-exponential fit.

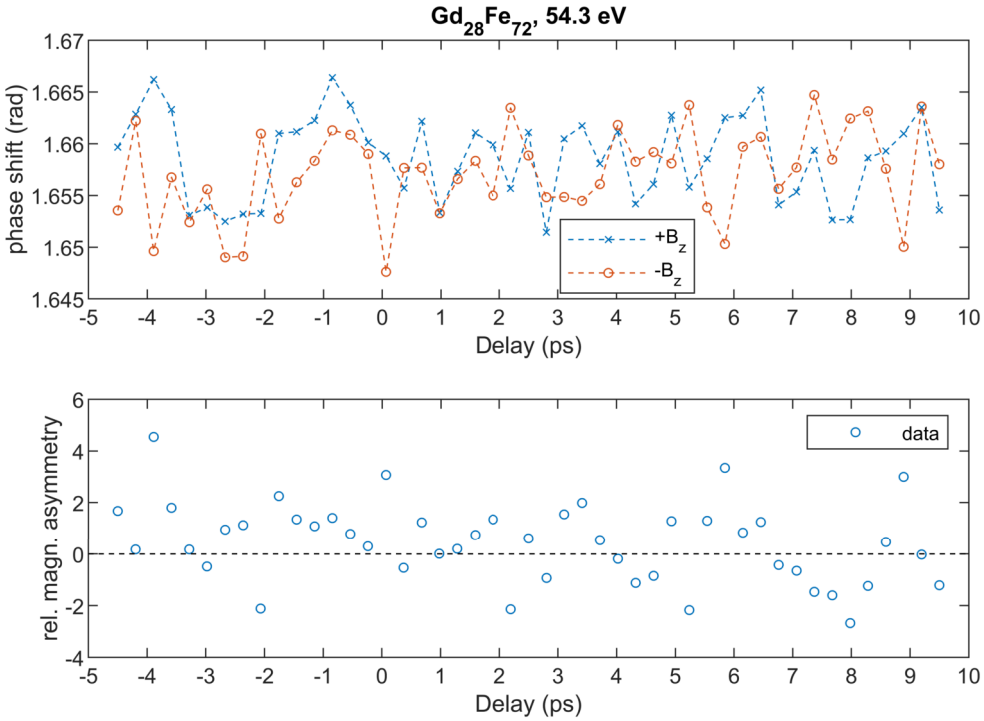

Figure 6.11: Simulated transient change of phase shift of $Gd_{28}Fe_{72}$ at 53.4 eV for both magnetic saturations directions (upper panel). The lower panel shows the relative magnetic asymmetry of both signals.

phase shifts for both magnetization states. As for the experimental data, the presence of a dynamical process in the simulation can not be discerned due to low SNR.

Figure 6.12 shows the magneto-optical constants for Fe around the M-edge, which we measured with our triple slit setup at the XUV-beamline UE112 at the synchrotron source BESSYII. The energy of the 35$^{\text{th}}$ harmonic (54.3 eV) is marked by a vertical line. It is apparent that while at that energy the dichroic absorptive contrast is maximal, the dichroic dispersive contrast is close to zero. With nearly no magnetic phase contrast at this energy, the SNR of the phase shift is expected to be low. An improvement of the experiment presented in this chapter would be to use a different harmonic, in which both $\Delta\beta$ and $\Delta\delta$ are sufficiently different from zero.

6.4 Discussion and Outlook

With the proof-of-principle experiment presented in this chapter, we have successfully demonstrated that our method is capable of measuring ultra-fast magnetization dynamics of absorption and dispersion at a HHG source. The photon energy of 54.3 eV was chosen such that the absorptive part of the magneto-optical constant of Fe was at its maximum, however, the dispersive part was close to zero. According to these magneto-optical constants, we could only measure a transient signal in the absorptive part within the measuring accuracy. We have shown by simulation that Poisson noise and readout noise are one of the two main error sources of the experiment. In addition to Poisson noise and readout noise, beam instabilities and beam inhomogeneities of the incident wavefront

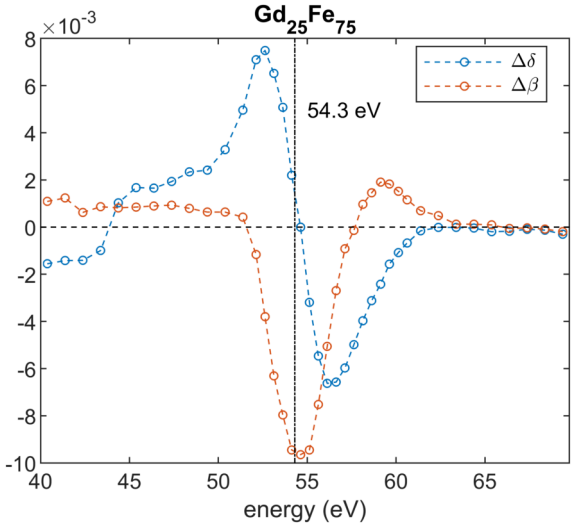

Figure 6.12: Magneto-optical constants for the Fe content of $Gd_{25}Fe_{75}$ at the M-edge. The energy of the 35th harmonics is marked by a vertical line.

further reduced the SNR of our measurement. This led to the fact that we can only make qualitative statements about the demagnetization dynamics.

In order to reduce the noise in subsequent measurements, we strongly recommend to use a focusing optic with longer focus length than in our experiment ($f = 250\,\mathrm{mm}$). As we have shown in Ch. 5.1, a longer focus length leads to a larger focus size and thus to less phase curvature. In Fig. 5.2d, we had estimated by a simulation that with our current setup, a relative beam to sample offset of about 25 nm between measurements would noticeable disturb the measurement. The exposure time for a scattering image was 30 s on average. Within this time frame, beam drifts larger than 25 nm were likely to occur (Fig. 6.8). If the ROC of the phase front were to increase by one order of magnitude, the tolerance to relative beam displacement would improve to 50 nm to 125 nm (depending on photon energy).

The properties of the HHG source should also be further optimized for subsequent experiments. With better beam stabilization, beam drift would occur on longer time scales. This would allow longer exposure times and thus increase the SNR. As we have shown in Ch. 5.3, it is important for a robust analysis of the optical constants to measure the scattering image at least up to the third main order. All destructive minima should have sufficient SNR, i.e., a smooth intensity profile to minimize reconstruction artefacts. The same effect would be achieved with a brighter source. The shorter the exposure time, the less existing beam instabilities disturb the measurement. In the extreme case of a very bright source, for instance a free electron laser (FEL), we are convinced[3] that our method is suitable for single-pulse measurements, making shot-to-shot fluctuations irrelevant.

We have seen that one problem of our experiment was that we could only measure one photon energy at a time. With a simple addition to our experiment, it would be possible to investigate the whole HHG spectrum at the same time (Fig. 6.13a). Assuming

[3]The total photon flux of the harmonic centred at 54.3 eV incident on the sample was $1 \times 10^8\,\mathrm{ph\,s^{-1}}$. For sufficient SNR, the CCD needed to integrate the far-field diffraction pattern for approximately 30 s. A FEL can provide a photon flux in the order of $1 \times 10^{12}\,\mathrm{ph\,pulse^{-1}}$ [25].

we can focus the entire HHG spectrum on the triple-slit, an added transmission grating behind the triple-slits could spatially separate the individual harmonics in the far field (Fig. 6.13c and d). With such an experimental design, all harmonics can simultaneously be investigated. In particular, this would allow to probe the M-edge response on- and off-resonance, making full use of the maximum phase contrast as well as the amplitude contrast.

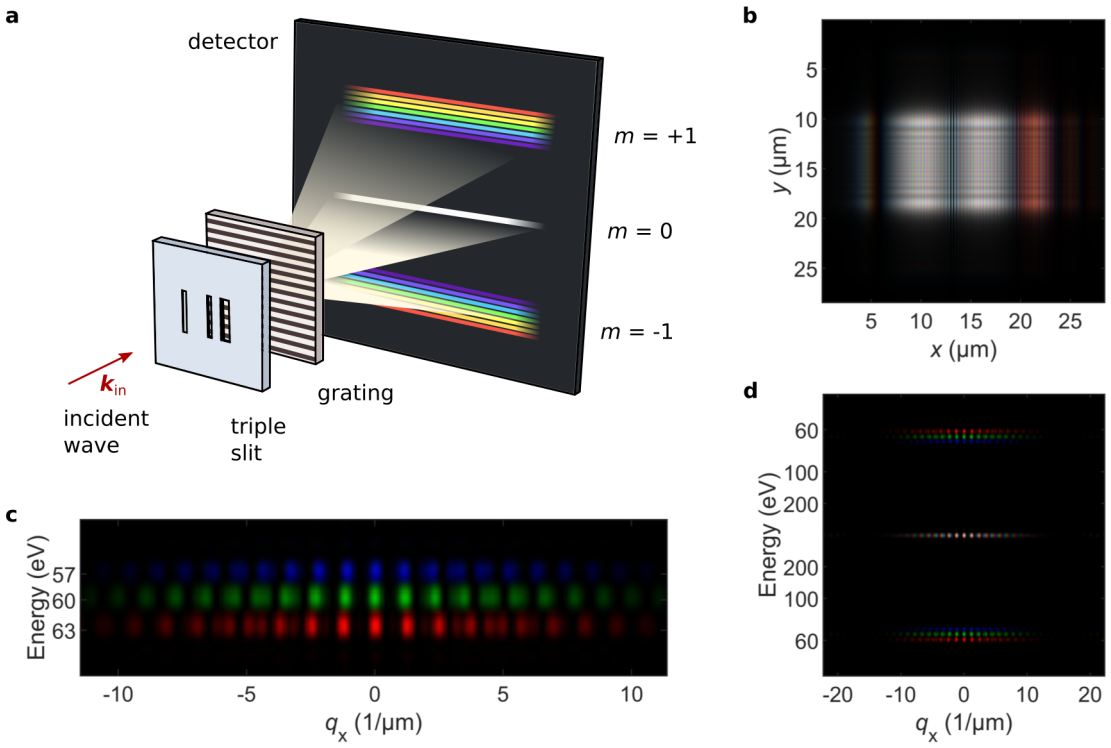

Figure 6.13: Simulation of a multi-color triple slit experiment. **a** Schematic demonstration of the geometry. Instead of selecting one harmonic of the XUV-beam, the full spectrum illuminates the standard triple slit. We add a grating 100 µm behind the triple slit. In the far field, the grating spatially separates the individual harmonics according to $\sin\phi = m\lambda/g$, with ϕ being the angle between the incident and exiting wave vector, m the order of the main maxima, and g the grating constant. **b** Simulated near field wave incident on the grating. For the simulation, we used three single energies, 57.34 eV, 60.45 eV, and 63.54 eV. These energies are demonstrated in this figure by the three different color channels red, green, and blue. The colormap displays the colors additive, meaning for example that for the color white all three channels contribute equally. **c** Magnification of the $m = -1$ diffraction order. The x-axis is labeled with the reciprocal coordinate, while the y-axis shows the corresponding energy. The three energy channels are spatially separated and the individual triple slit diffraction is clearly visible in each case. **d** Full size far field diffraction pattern of the multi-color triple slit simulation. The labels of the axis are similar as in **c**.

CHAPTER 7

Summary

This thesis presents a novel interferometric method for the spectroscopic and time-resolved investigation of the optical and magneto-optical refractive index of thin films in the soft x-ray and XUV spectral range. Given the increasing availability of laboratory sources and large-scale facilities providing ultra-short pulses in this photon energy range, the application of this radiation for investigating ultrafast phenomena in condensed matter with high specificity is largely increasing as well. As a result, a urgent demand for spectroscopic data, in particular for the electronic resonances, was created. Still important data of the refractive index is missing and previous experiments have often determined the complex refractive index in separate measurements or have estimated the missing part by a Kramers-Kronig transformation.

The wavefront splitter of our interferometer consists of a simple monolithic combination of a double slit acting as a reference and an additional aperture containing the sample system under investigation as a free-standing film. The interferogram measured in the far field is evaluated by a single Fourier transformation. Via polarization-dependent measurements, the dichroic contributions to the complex refractive index due to the magnetization of the material can be extracted.

Compared to previous methods [5, 9, 10], our method determines the absorptive and dispersive part of the refractive index within a single exposure and does not depend on additional normalization measurements as it uses a self-normalizing approach. Due to the simple experimental implementation of our interferometer and its low spatial requirements, it is readily possible to realize elaborate and customized sample environments such as the installation of an electromagnet in the direct vicinity of the sample to investigate the magneto-optical properties. Other examples include a cryostat for temperature control and optical or THz excitation.

Unlike other coherent methods that determine the complex refractive index [1, 17], the analysis of our data is not based on an iterative algorithm. A single numerical Fourier transformation is sufficient to analyse the complex refractive index. In this sense, our method is closely related to Fourier-transform holography [22, 24].

We implemented our interferometric method at a synchrotron source (Ch. 4) and a

HHG source (Ch. 6). Spectroscopic results are presented for $Gd_{25}Co_{75}$-alloy, $Gd_{25}Fe_{75}$-alloy, and $[Co(4)Pt(7)]_{\times 20}$-multilayers, investigating for Co and Fe both the spectral regions of the respective M- and L-edges and for Gd the spectral region corresponding to the N-edge. A Kramers-Kronig transformation analysis showed the self-consistency of our simultaneous measurement of the absorptive and dispersive part of the optical and magneto-optical refractive index. For all of these measurements we find very good agreement of our measurements with data from literature, demonstrating the reliability of our method. As the only exception, we observe a deviation of our measurement from previous experiments (Prieto et al. [61]) in the case of the magneto-optical spectrum for the Gd N-edge (Ch. 4.2.2). In this case, we compared our data with theoretical *ab initio* calculation and found a good agreement between both our data and theory. As the sample layer thickness is a scaling parameter in our analysis of the refractive index, we confirmed in particular the thickness of the $Gd_{25}Fe_{75}$ sample layer with transmission electron microscopy (Ch. 4.3.1). We conclude that within the estimated error our values for the magneto-optical indices of Gd in $Gd_{25}Fe_{75}$ and $Gd_{25}Co_{75}$ at the N-edge are accurate.

Beside the analysis of the magneto-optical index, we have determined the optical constants for Co at the L-edge (Ch. 4.2.3). Our data showed very good agreement with data from literature. A single measurement is sufficient to determine both the real and imaginary part of the refractive index. Only if the influence of the substrate and potential seed and cap layers has to be considered, a second measurement using a reference sample is necessary. If differential information are sufficient for the experiment such as for the investigation of the magneto-optical contributions or transient changes, this reference measurement can be omitted.

To estimate the SNR limits of our method, we investigated the measured influence of exposure time and data acquisition order (Ch. 4.4) and investigated the simulated influence of different beam parameters (like partial coherence (Ch. 3.2.1) and beam curvature, sampling, exposure time, and shot and read-out noise (Ch. 5)) on the data analysis. The main statements from these considerations are:

1. The SNR must be sufficient to measure the destructive interference minima up to the third main diffraction order in order not to get noticeable perturbation in the analysis.

2. Slight undersampling of the data can be tolerated. In this case, however, the reconstruction must be corrected because of the point spread function of the CCD (Ch. 2.3).

3. The cross-correlations plateaus must be sampled by at least two pixels. This is achieved by having reference slits with different sizes.

4. Since our method transmits only a small part of a wider coherent beam, this spatial filtering is sufficient to ensure that spatial coherence is not a limitation for reconstruction.

5. The bandwidth of the photon energy has to be also considered for the error of refractive index' real part and not only for the spectroscopic resolution. As an example, a photon energy bandwidth of $\approx 0.5\,\mathrm{eV}$ with a central energy of $54.3\,\mathrm{eV}$ leads to an error of $\approx 1\,\%$ in the analysis of the phase shift of Fe in a $Gd_{25}Fe_{75}$

sample layer. The largest photon energy bandwidth during our experiment was 0.2 eV for the HHG source and, therefore, not a concern for our experiment.

6. Shot noise and read-out noise in the scattering image are no major issues (as long as point 1 is valid) because in the analysis the noise can be averaged out.

7. The main issues of our interferometric method are the curvature of the incident wavefront and the temporal stability of the beam position on the sample. The wave front curvature must be approximated by a plane wave over the size of all the slit apertures for the measurements of the optical indices. For the magneto-optical indices, the beam position must be stable during the exposure time of at least two scattering images.

Another aim of this thesis was the application of our interferometric method on time-resolved measurements. As a first step, we set up a time-resolved small-angle scattering experiment using a high-harmonic generation source, where we measured the ultra-fast demagnetization of Co in $[\mathrm{Co}(8)/\mathrm{Pt}(8)]_{\times 16}$ at the Co M-edge for three different pump fluences between $4.0\,\mathrm{mJ\,cm^{-2}}$ and $9.9\,\mathrm{mJ\,cm^{-2}}$ (Ch. 6.1). To switch from the small-angle scattering experiment to the time-resolved interferometric experiment, no major changes of the experimental geometry were necessary. We present a proof-of-concept experiment for a time-resolved investigation in a pump-probe scheme (Ch. 6). Using the high-harmonic generation source for interferometric probing, the evolution of the magneto-optical refractive index of Fe in $Gd_{28}Fe_{72}$ at the Fe M-edge (54.3 eV) is studied after optical excitation leading to ultrafast demagnetization. The results were compared to a simulation to analyse the SNR of the measurement.

The main challenges of our time-resolved interferometric experiment turned out to be the low dichroic phase signal at 54.3 eV and the positional beam instabilities. As we discussed in Ch. 6.4, the low dicroidic phase signal can be enhanced by using a different harmonic closer to the maximum of $\Delta\delta$. The errors caused by the beam instabilities can be reduced by using a longer focus length for the focussing optic. This reduces beam curvature and enhances the tolerance against orthogonal beam drift. For further experiments, a brighter source would lead to faster exposure times. This would decrease the impact of the slow beam drift onto the scattering image. In the extreme case of a very bright source, for instance a free electron laser, we are convinced that our method is suitable for single-pulse measurements of the absorptive and simultaneously the dispersive part of the refractive indices. The photon flux of the harmonic centred at 54.3 eV incident on the sample was $1 \times 10^8\,\mathrm{ph\,s^{-1}}$ (Ch. 3.2). For sufficient SNR, the CCD needed to integrate the far-field diffraction pattern for approximately 30 s. A FEL can provide a photon flux in the order of $1 \times 10^{12}\,\mathrm{ph\,pulse^{-1}}$ [25]. This photon flux in combination with single-pulse measurements would make shot-to-shot fluctuations irrelevant.

Appendices

APPENDIX A

Reconstruction Protocol of the Triple Slit Data

1. Average dark images and subtract them from the triple slit scattering patterns.
2. Correct cosmic rays in the scattering pattern.
3. Shift the center of all individual scattering patterns to the center of the array.
4. (Opt.) Use inverse gnomonic projection to correct tilted sample-detector plane.
5. Align the axis of the dominant spatial frequencies with the axis of the array, by rotating the scattering pattern by the appropriate angle. This corrects a misalignment between the axis of the triple slits with the detector.
6. Crop the image to exclude areas of zeros introduced to the array via the rotation step.
7. Apply a 2D discrete Fourier transformation to the data to yield the 2D reconstruction array of the data.
8. Use a line scan through the maxima of all 2D cross-correlations to get the 1D reconstruction array.
9. Multiply an appropriate phase ramp to the 1D reconstruction array to correct for subpixel misalignments of the data. The phase should be such that the image and the twin-image of the phase cross-correlation between both reference slits become mutually zero.
10. Average over the plateau of the cross-correlation of both reference slits to get the normalizing factor c_{23}. If the plateau of this cross-correlation is sampled by only one pixel: use linear fits to the sides of the cross-correlation and their intersection as normalizing factor c_{23}.
11. Average over the first cross-correlation between reference slit and material slit to get c_{12}.

12. Use $|c_{12}|/c_{23}$ to get the normalized transmission through the sample layer. Use $\arg c_{12}$ to get the phase shift through the sample layer.

APPENDIX B

Additional Spectra of $Gd_{25}Co_{75}$ Co/Pt and Ta

B.1 *O*-Edge Resonance of Ta

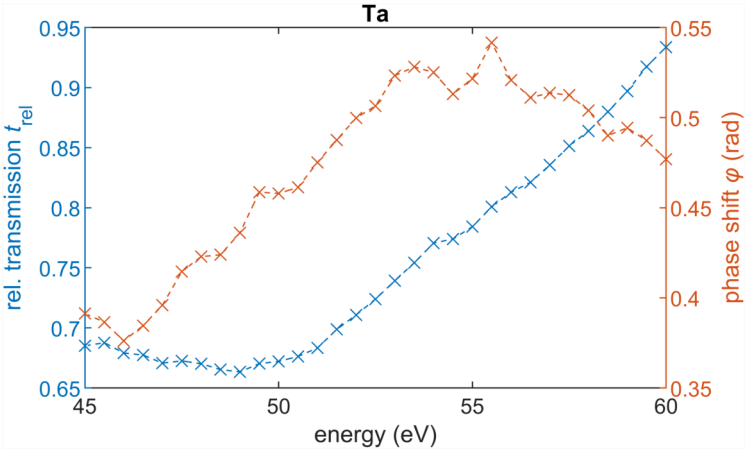

Figure B.1: Spectroscopic response of transmission and phase shift of Si_3N_4(200 nm)/Ta(3 nm) at the Ta *O*-edge.

B.2 *M*-Edge Resonance of $Gd_{25}Co_{75}$ith KK Inversion

B.3 *M*-Edge Resonance of $[Co(4)Pt(7)]_{\times 20}$

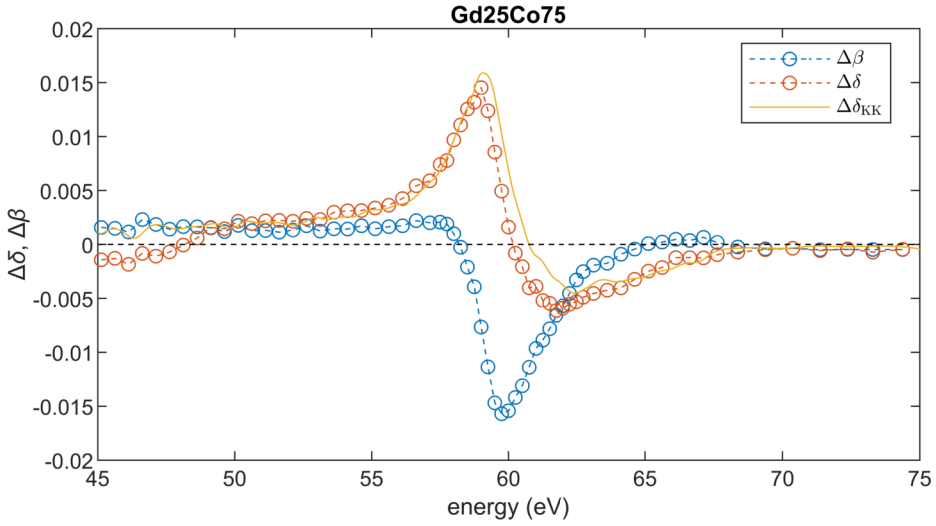

Figure B.2: Comparison of $\Delta\delta$ with the KK inversion of $\Delta\beta$ for Co at the M edge. The $Gd_{25}Co_{75}$ layer was protected by a 3 nm capping layer and seeded by a 2 nm Ta layer. The spectrum of $\Delta\beta$ was extended to lower photon energies by the average of the pre-edge asymmetry to prevent discontinuity in the KK inversion integral.

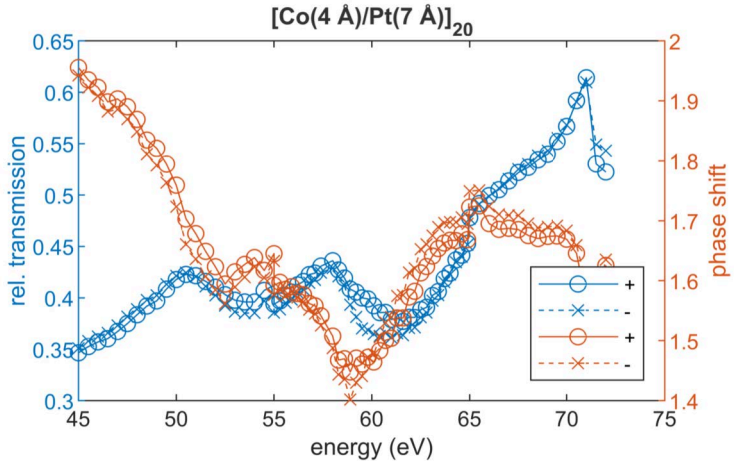

Figure B.3: Spectroscopic response of transmission and phase shift of $[Co(4)Pt(7)]_{20}$ at the Co M-edge with circularly polarized light.

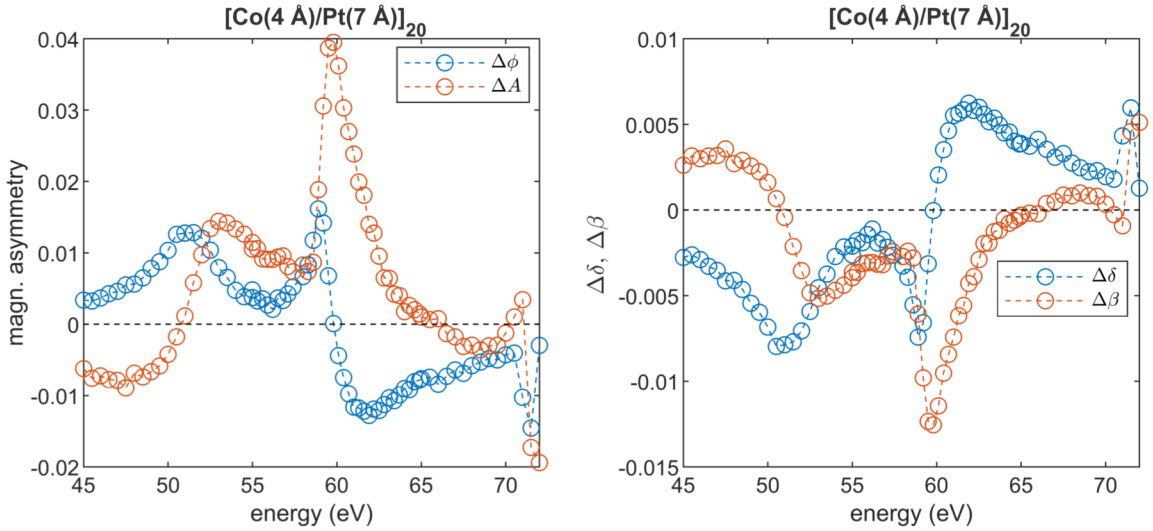

Figure B.4: Spectroscopic response of the complex dichroidic part of the optical constants of a $[\mathrm{Co}(4)\mathrm{Pt}(7)]_{20}$ multilayer at the Co M-edge.

Bibliography

[1] D. Hemmers, M. Benzid, and G. Pretzler, "Direct measurement of the complex refractive index of thin foils in the XUV spectral range by point diffraction interferometry," *Applied Physics B*, vol. 108, no. 1, pp. 167–175, 2012.

[2] C. Stanciu, F. Hansteen, A. Kimel, A. Kirilyuk, A. Tsukamoto, A. Itoh, and T. Rasing, "All-optical magnetic recording with circularly polarized light," *Physical review letters*, vol. 99, no. 4, p. 047601, 2007.

[3] F. Willems, S. Sharma, C. v. K. Schmising, J. Dewhurst, L. Salemi, D. Schick, P. Hessing, C. Strüber, W. Engel, and S. Eisebitt, "Magneto-optical functions at the 3 p resonances of Fe, Co, and Ni: Ab initio description and experiment," *Physical review letters*, vol. 122, no. 21, p. 217202, 2019.

[4] M. Hennecke, I. Radu, R. Abrudan, T. Kachel, K. Holldack, R. Mitzner, A. Tsukamoto, and S. Eisebitt, "Angular momentum flow during ultrafast demagnetization of a ferrimagnet," *Physical review letters*, vol. 122, no. 15, p. 157202, 2019.

[5] B. L. Henke, E. M. Gullikson, and J. C. Davis, "X-ray interactions: photoabsorption, scattering, transmission and reflection E= 50-30,000 eV, Z= 1-92," *Atomic data and nuclear data tables*, vol. 54, no. 2, 1993.

[6] R. d. L. Kronig and H. Kramers, "Atti congr. intern. fisici," *Como*, vol. 2, p. 545, 1927.

[7] V. Lucarini, J. J. Saarinen, K.-E. Peiponen, and E. M. Vartiainen, *Kramers-Kronig relations in optical materials research*, vol. 110. Berlin: Springer Science & Business Media, 2005.

[8] L. D. Landau, J. Bell, M. Kearsley, L. Pitaevskii, E. Lifshitz, and J. Sykes, *Electrodynamics of continuous media*, vol. 8. Amsterdam: elsevier, 2013.

[9] N. Brimhall, N. Herrick, D. D. Allred, R. S. Turley, M. Ware, and J. Peatross, "Measured optical constants of copper from 10 nm to 35 nm," *Optics Express*, vol. 17, no. 26, pp. 23873–23879, 2009.

[10] J. Svatos, D. Joyeux, D. Phalippou, and F. Polack, "Soft-x-ray interferometer for measuring the refractive index of materials," *Optics letters*, vol. 18, no. 16, pp. 1367–1369, 1993.

[11] K. Rosfjord, C. Chang, R. Miyakawa, H. Barth, and D. Attwood, "Direct index of refraction measurements at extreme-ultraviolet and soft-x-ray wavelengths," *Applied optics*, vol. 45, no. 8, pp. 1730–1736, 2006.

[12] C. Chang, E. Anderson, P. Naulleau, E. Gullikson, K. Goldberg, and D. Attwood, "Direct measurement of index of refraction in the extreme-ultraviolet wavelength region with a novel interferometer," *Optics letters*, vol. 27, no. 12, pp. 1028–1030, 2002.

[13] M. Wieland, T. Wilhein, C. Spielmann, and U. Kleineberg, "Zone-plate interferometry at 13 nm wavelength," *Applied Physics B*, vol. 76, no. 8, pp. 885–889, 2003.

[14] L. Sève, J. Tonnerre, and D. Raoux, "Determination of the anomalous scattering factors in the soft-x-ray range using diffraction from a multilayer," *Journal of applied crystallography*, vol. 31, no. 5, pp. 700–707, 1998.

[15] M. Magnuson and C. F. Hague, "Determination of the refractive index at soft x-ray resonances," *Journal of electron spectroscopy and related phenomena*, vol. 137, pp. 519–522, 2004.

[16] D. L. Windt, S. Donguy, C. J. Hailey, J. E. Koglin, V. Honkimaki, E. Ziegler, F. E. Christensen, and F. A. Harrison, "Optical constants for hard x-ray multilayers over the energy range E= 35–180 keV," in *Optics for EUV, X-Ray, and Gamma-Ray Astronomy*, vol. 5168, pp. 35–40, International Society for Optics and Photonics, 2004.

[17] B. Mills, C. Chau, E. Rogers, J. Grant-Jacob, S. Stebbings, M. Praeger, A. De Paula, C. Froud, R. Chapman, T. Butcher, *et al.*, "Direct measurement of the complex refractive index in the extreme ultraviolet spectral region using diffraction from a nanosphere array," *Applied Physics Letters*, vol. 93, no. 23, p. 231103, 2008.

[18] R. Feynman, R. Leighton, and M. Sands, *The Feynman Lectures on Physics, Vol. III: The New Millennium Edition: Quantum Mechanics*. The Feynman Lectures on Physics, New York: Basic Books, 2011.

[19] T. Young, "II. the Bakerian lecture. on the theory of light and colours," *Philosophical transactions of the Royal Society of London*, no. 92, pp. 12–48, 1802.

[20] T. Young, *A course of lectures on natural philosophy and the mechanical arts: in two volumes*, vol. 2. London: Johnson, 1807.

[21] G. Taylor, "The phase problem," *Acta Crystallographica Section D: Biological Crystallography*, vol. 59, no. 11, pp. 1881–1890, 2003.

[22] S. Eisebitt, J. Lüning, W. Schlotter, M. Lörgen, O. Hellwig, W. Eberhardt, and J. Stöhr, "Lensless imaging of magnetic nanostructures by x-ray spectro-holography," *Nature*, vol. 432, no. 7019, pp. 885–888, 2004.

[23] J. W. Goodman, *Introduction to Fourier optics*. Greenwood Village: Roberts and Company Publishers, 2005.

[24] B. Pfau and S. Eisebitt, "X-ray holography," in *Synchrotron Light Sources and Free-Electron Lasers: Accelerator Physics, Instrumentation and Science Applications* (E. J. Jaeschke, S. Khan, J. R. Schneider, and J. B. Hastings, eds.), pp. 1093–1133, Springer, 2016.

[25] D. Attwood and A. Sakdinawat, *X-rays and extreme ultraviolet radiation: principles and applications*. Cambridge: Cambridge university press, 2017.

[26] D. F. Gardner, B. Zhang, M. D. Seaberg, L. S. Martin, D. E. Adams, F. Salmassi, E. Gullikson, H. Kapteyn, and M. Murnane, "High numerical aperture reflection mode coherent diffraction microscopy using off-axis apertured illumination," *Optics express*, vol. 20, no. 17, pp. 19050–19059, 2012.

[27] S. Schaffert, B. Pfau, J. Geilhufe, C. M. Günther, M. Schneider, C. von Korff Schmising, and S. Eisebitt, "High-resolution magnetic-domain imaging by Fourier transform holography at 21 nm wavelength," *New Journal of Physics*, vol. 15, no. 9, p. 093042, 2013.

[28] C. E. Shannon, "Communication in the presence of noise," *Proceedings of the IRE*, vol. 37, no. 1, pp. 10–21, 1949.

[29] B. Pfau, C. Günther, S. Schaffert, R. Mitzner, B. Siemer, S. Roling, H. Zacharias, O. Kutz, I. Rudolph, R. Treusch, *et al.*, "Femtosecond pulse x-ray imaging with a large field of view," *New Journal of Physics*, vol. 12, no. 9, p. 095006, 2010.

[30] J. Stöhr and H. C. Siegmann, "Magnetism," *From fundamentals to Nanoscale Dynamics*, 2006.

[31] P. J. de Groot, "A review of selected topics in interferometric optical metrology," *Reports on Progress in Physics*, vol. 82, no. 5, p. 056101, 2019.

[32] S. Samsonov, A. Dille, O. Dewitte, F. Kervyn, and N. d'Oreye, "Satellite interferometry for mapping surface deformation time series in one, two and three dimensions: A new method illustrated on a slow-moving landslide," *Engineering Geology*, vol. 266, p. 105471, 2020.

[33] B. P. Abbott, R. Abbott, T. Abbott, M. Abernathy, F. Acernese, K. Ackley, C. Adams, T. Adams, P. Addesso, R. Adhikari, *et al.*, "Observation of gravitational waves from a binary black hole merger," *Physical review letters*, vol. 116, no. 6, p. 061102, 2016.

[34] R. Verma, *Wave Optics*. New Delhi: Discovery Publishing House Pvt. Limited, 2006.

[35] D. Nolte, *Optical Interferometry for Biology and Medicine*. Bioanalysis, New York City: Springer New York, 2011.

[36] E. Beaurepaire, J.-C. Merle, A. Daunois, and J.-Y. Bigot, "Ultrafast spin dynamics in ferromagnetic nickel," *Phys. Rev. Lett.*, vol. 76, pp. 4250–4253, May 1996.

[37] C. D. Stanciu, F. Hansteen, A. V. Kimel, A. Kirilyuk, A. Tsukamoto, A. Itoh, and T. Rasing, "All-optical magnetic recording with circularly polarized light," *Phys. Rev. Lett.*, vol. 99, p. 047601, Jul 2007.

[38] C. Boeglin, E. Beaurepaire, V. Halté, V. López-Flores, C. Stamm, N. Pontius, H. Dürr, and J.-Y. Bigot, "Distinguishing the ultrafast dynamics of spin and orbital moments in solids," *Nature*, vol. 465, no. 7297, pp. 458–461, 2010.

[39] N. Bergeard, V. López-Flores, V. Halte, M. Hehn, C. Stamm, N. Pontius, E. Beaurepaire, and C. Boeglin, "Ultrafast angular momentum transfer in multisublattice ferrimagnets," *Nature communications*, vol. 5, no. 1, pp. 1–7, 2014.

[40] J. Dewhurst, F. Willems, P. Elliott, Q. Li, C. von Korff Schmising, C. Strüber, D. Engel, S. Eisebitt, and S. Sharma, "Element specificity of transient extreme ultraviolet magnetic dichroism," *Physical Review Letters*, vol. 124, no. 7, p. 077203, 2020.

[41] U. Bovensiepen, "Magnetism in step with light," *Nature Physics*, vol. 5, no. 7, pp. 461–463, 2009.

[42] C. Chappert and P. Bruno, "Magnetic anisotropy in metallic ultrathin films and related experiments on cobalt films," *Journal of Applied Physics*, vol. 64, no. 10, pp. 5736–5741, 1988.

[43] M. Ding and S. J. Poon, "Tunable perpendicular magnetic anisotropy in GdFeCo amorphous films," *Journal of magnetism and magnetic materials*, vol. 339, pp. 51–55, 2013.

[44] P. S. Miedema, W. Quevedo, and M. Fondell, "The variable polarization undulator beamline UE52 SGM at BESSY II," *Journal of large-scale research facilities JLSRF*, vol. 2, p. 70, 2016.

[45] G. Schiwietz, M. Beye, and T. Kachel, "UE112_PGM-1: An open-port low-energy beamline at the BESSY II undulator UE112," *Journal of large-scale research facilities JLSRF*, vol. 1, p. 33, 2015.

[46] K. Yao, F. Willems, C. von Korff Schmising, C. Strüber, P. Hessing, B. Pfau, D. Schick, D. Engel, K. Gerlinger, M. Schneider, *et al.*, "A tabletop setup for ultrafast helicity-dependent and element-specific absorption spectroscopy and scattering in the extreme ultraviolet spectral range," *Review of Scientific Instruments*, vol. 91, no. 9, p. 093001, 2020.

[47] C. von Korff Schmising, D. Weder, T. Noll, B. Pfau, M. Hennecke, C. Strüber, I. Radu, M. Schneider, S. Staeck, C. M. Günther, *et al.*, "Generating circularly polarized radiation in the extreme ultraviolet spectral range at the free-electron laser FLASH," *Review of Scientific Instruments*, vol. 88, no. 5, p. 053903, 2017.

[48] CXRO, "X-ray database: optical constants," 2010, last visited on 2019-10-10.

[49] G. Geloni, E. Saldin, E. Schneidmiller, and M. Yurkov, "Transverse coherence properties of x-ray beams in third-generation synchrotron radiation sources," *Nuclear Instruments and Methods in Physics Research Section A: Accelerators, Spectrometers, Detectors and Associated Equipment*, vol. 588, no. 3, pp. 463–493, 2008.

[50] B. Pfau, *Imaging Magnetic Nanostructures using Soft X-ray Fourier Transform Holography*. PhD thesis, Technical University Berlin, 2013.

[51] T. Ditmire, E. Gumbrell, R. Smith, J. Tisch, D. Meyerhofer, and M. Hutchinson, "Spatial coherence measurement of soft x-ray radiation produced by high order harmonic generation," *Physical Review Letters*, vol. 77, no. 23, p. 4756, 1996.

[52] T. Ditmire, J. Tisch, E. Gumbrell, R. Smith, D. Meyerhofer, and M. Hutchinson, "Spatial coherence of short wavelength high-order harmonics.," *Applied Physics B: Lasers & Optics*, vol. 65, no. 3, 1997.

[53] R. A. Bartels, A. Paul, H. Green, H. C. Kapteyn, M. M. Murnane, S. Backus, I. P. Christov, Y. Liu, D. Attwood, and C. Jacobsen, "Generation of spatially coherent light at extreme ultraviolet wavelengths," *Science*, vol. 297, no. 5580, pp. 376–378, 2002.

[54] W. T. Silfvast, *Laser fundamentals*. Cambridge: Cambridge university press, 2004.

[55] S. Flewett, H. M. Quiney, C. Q. Tran, and K. A. Nugent, "Extracting coherent modes from partially coherent wavefields," *Optics letters*, vol. 34, no. 14, pp. 2198–2200, 2009.

[56] M. Dierolf, A. Menzel, P. Thibault, P. Schneider, C. M. Kewish, R. Wepf, O. Bunk, and F. Pfeiffer, "Ptychographic x-ray computed tomography at the nanoscale," *Nature*, vol. 467, no. 7314, pp. 436–439, 2010.

[57] M. Odstrcil, P. Baksh, S. Boden, R. Card, J. Chad, J. Frey, and W. Brocklesby, "Ptychographic coherent diffractive imaging with orthogonal probe relaxation," *Optics express*, vol. 24, no. 8, pp. 8360–8369, 2016.

[58] P. Hessing, "Holographie-gestützte Ptychographie mit weicher Röntgenstrahlung," Master's thesis, Technical University Berlin, 2014.

[59] L. Caretta, M. Mann, F. Büttner, K. Ueda, B. Pfau, C. M. Günther, P. Hessing, A. Churikova, C. Klose, M. Schneider, *et al.*, "Fast current-driven domain walls and small skyrmions in a compensated ferrimagnet," *Nature nanotechnology*, vol. 13, no. 12, pp. 1154–1160, 2018.

[60] K. Starke, E. Navas, E. Arenholz, Z. Hu, L. Baumgarten, G. Van der Laan, C. Chen, and G. Kaindl, "Magnetic circular dichroism in 4d→ 4f resonant photoemission and photoabsorption of gd metal," *Physical Review B*, vol. 55, no. 4, p. 2672, 1997.

[61] J. Prieto, F. Heigl, O. Krupin, G. Kaindl, and K. Starke, "Prediction of huge x-ray Faraday rotation at the Gd n 4, 5 threshold," *Physical Review B*, vol. 66, no. 17, p. 172408, 2002.

[62] F. Heigl, *Magnetooptics in Lanthanides*. PhD thesis, Free University of Berlin, 2003.

[63] F. Willems, *Ultrafast optical demagnetization dynamics in thin elemental films and alloys: foundations of and results from helicity-dependent and time-resolved XUV spectroscopy*. PhD thesis, Technical University Berlin, 2019.

[64] C. Korff Schmising. private communication.

[65] S. Sharma. private communication.

[66] K. Dewhurst, S. Sharma, L. Nordström, F. Cricchio, O. Gråsäs, and H. Gross, "The ELK code," 2018.

[67] A. Thompson, *X-ray Data Booklet*. Berkeley: Lawrence Berkeley National Laboratory, University of California, 2001.

[68] H.-C. Mertins, S. Valencia, D. Abramsohn, A. Gaupp, W. Gudat, and P. M. Oppeneer, "X-ray Kerr rotation and ellipticity spectra at the 2 p edges of Fe, Co, and Ni," *Physical Review B*, vol. 69, no. 6, p. 064407, 2004.

[69] J. B. Kortright, S.-K. Kim, G. P. Denbeaux, G. Zeltzer, K. Takano, and E. E. Fullerton, "Soft-x-ray small-angle scattering as a sensitive probe of magnetic and charge heterogeneity," *Physical Review B*, vol. 64, no. 9, p. 092401, 2001.

[70] N. Nakajima, T. Koide, T. Shidara, H. Miyauchi, H. Fukutani, A. Fujimori, K. Iio, T. Katayama, M. Nỳvlt, and Y. Suzuki, "Perpendicular magnetic anisotropy caused by interfacial hybridization via enhanced orbital moment in Co/Pt multilayers: Magnetic circular x-ray dichroism study," *Physical Review Letters*, vol. 81, no. 23, p. 5229, 1998.

[71] T. Ueno, J. Sinha, N. Inami, Y. Takeichi, S. Mitani, K. Ono, and M. Hayashi, "Enhanced orbital magnetic moments in magnetic heterostructures with interface perpendicular magnetic anisotropy," *Scientific reports*, vol. 5, p. 14858, 2015.

[72] D. Lide, R. Weast, and C. R. Company, *CRC Handbook of Chemistry and Physics: A Ready-reference Book of Chemical and Physical Data*. Boca Raton: CRC Press, 1984.

[73] O. Svelto and D. C. Hanna, *Principles of lasers*, vol. 1. Berlin: Springer, 2010.

[74] J. Geilhufe, B. Pfau, C. M. Günther, M. Schneider, and S. Eisebitt, "Achieving diffraction-limited resolution in soft-x-ray Fourier-transform holography," *Ultramicroscopy*, p. 113005, 2020.

[75] P. Erez, "Shot noise generator," 2018, last visited on 2020-09-10.

[76] K. Holldack, J. Bahrdt, A. Balzer, U. Bovensiepen, M. Brzhezinskaya, A. Erko, A. Eschenlohr, R. Follath, A. Firsov, W. Frentrup, *et al.*, "FemtoSpeX: a versatile optical pump–soft x-ray probe facility with 100 fs x-ray pulses of variable polarization," *Journal of synchrotron radiation*, vol. 21, no. 5, pp. 1090–1104, 2014.

[77] F. Willems, C. Smeenk, N. Zhavoronkov, O. Kornilov, I. Radu, M. Schmidbauer, M. Hanke, C. von Korff Schmising, M. Vrakking, and S. Eisebitt, "Probing ultrafast spin dynamics with high-harmonic magnetic circular dichroism spectroscopy," *Physical Review B*, vol. 92, no. 22, p. 220405, 2015.

[78] B. Vodungbo, J. Gautier, G. Lambert, A. B. Sardinha, M. Lozano, S. Sebban, M. Ducousso, W. Boutu, K. Li, B. Tudu, *et al.*, "Laser-induced ultrafast demagnetization in the presence of a nanoscale magnetic domain network," *Nature communications*, vol. 3, no. 1, pp. 1–6, 2012.

[79] K. Kuiper, T. Roth, A. Schellekens, O. Schmitt, B. Koopmans, M. Cinchetti, and M. Aeschlimann, "Spin-orbit enhanced demagnetization rate in Co/Pt-multilayers," *Applied Physics Letters*, vol. 105, no. 20, p. 202402, 2014.

CHAPTER 8

Acknowledgements

First and foremost, I would like to express my gratitude to Prof. Stefan Eisebitt for his support, guidance, and encouragement. I am glad to have had the opportunity to have had such a scientifically excellent as well as kind supervisor during my time at the Max Born Institute.

Secondly, I want to thank Dr. Bastian Pfau for his support throughout all the stages of my thesis including help with preparing and realizing my experiments, and fruitful scientific discussions of ideas and results.

The experiments and results presented in this thesis could not have been performed and produced without the assistance, patience, and helpful insights of many colleagues. I would like to thank Dr. Christian Günther, Dr. Michael Schneider, and Dr. Dieter Engel for their help with the sample fabrication process. Without their knowledge about nanostructuring with FIB and producing magnetic thin films, the execution of the triple-slit experiments would not have been possible. The knowledge of Dr. Christian Strüber and Dr. Daniel Schick regarding everything HHG related was a crucial part of the success of the time-resolved, proof-of-concept experiment. Beside countless hours at beamtimes and in the lab, the scientific input, positivity, and friendly words of Dr. Clemens von Korff Schmising were always a delight, for which I will remain grateful. I would also like to thank Dr. Ilie Radu for his motivational attitude and in-depth discussions about XMCD and time-resolved spectroscopy. Furthermore, I would like to thank Dr. Sangeeta Sharma for the electronic structure calculation at the Gd N-edge. By writing the data acquisition software for the triple-slit experiments and providing support even at inopportune times (nightshifts at beamtimes), Marc Zieglarski played a crucial part in the realization of the experiments, for which I am thankful. For all things related to designing in CAD, I could always rely on Dr. Tino Noll and Bertram Friedrich. Whenever electrical or mechanical problems occurred, the whole team of the workshop did a great job of fixing them.

One essential reason that my time at the Max Born Institute will remain unforgettable lies in the personal interactions with my fellow Ph.D. candidates, e.g. lively discussions about physics, doing sport competitions during breaks and after work, supporting each other in the lab, and lending each other an ear even when times got hard. For all the

great times, thank you Felix Willems, David Weder, Michael Schneider, Martin Hennecke, Kelvin Yao, and Martin Borchert.

Additionally, I would like to thank the music ensemble of the TU Berlin physics' department for being a weakly retreat and a source of inspiration.

Thank you Adrian, Johannes, Lara, and Elke for accompanying me on this way.

I want to express my deeply felt gratitude to my parents who have supported me throughout all the stages of my academic career with infinite patience and creativity.

Finally, I would like to thank Behnoush. Without her love, patience, sense of humour, and understanding, the writing of this thesis would have been so much harder.